SC-RR-69-512

ELECTRON BEAM DIAGNOSTICS: PART I

William H. Buckalew
Lawrence D. Posey
Radiation Source Diagnostics Division 5223
Sandia Laboratories
Albuquerque, New Mexico

October 1969

ABSTRACT

Methods for performing pulsed electron beam diagnostics are presented, and techniques for determining energy deposition profiles and beam energy density are discussed. The dosimetry materials and instrumentation employed in measurements of this type are treated in detail.

In addition, techniques for the determination of electron beam pulse profile as well as differential energy spectrum are considered.

Representative data, obtained using the above techniques to define the electron beam output of the Sandia Model 705 Febetron and Hermes I, are included.

TABLE OF CONTENTS

LIST OF ILLUSTRATIONS

4

LIST OF ILLUSTRATIONS (cont)

5

6

ELECTRON BEAM DIAGNOSTICS: PART I

I. INTRODUCTION

Electron beams, both pulsed and steady state, have been and are presently being employed to study basic material behavior, such as space charge buildup and breakdown in dielectric materials[1-4] and the thermoelastic properties of materials as contained in the Gruneisen coefficient.[5,6]

In order to accurately analyze the results of measurements of this type, a detailed description of the electron beam is required. Ideally, this description should include information on the absorbed dose to various materials, the beam energy density, the electron beam time history, and the electron beam differential energy spectrum. These quantities are spatially varying functions (1) for electron beams where the (Bennett) pinch[7,8] mode of operation is employed, or (2) for electron beams produced by machines employing external magnetic field constriction. This is a result of the complex trajectories of the electrons in the fields produced by (1) the plasma which gives rise to the (Bennett) pinch, or (2) the external focussing coils. Hence, the complete definition of the electron beam environment at all useful spatial positions and for all operating conditions (i.e., magnetic focussing field, gas pressure, etc.) is a task of substantial magnitude. As a result, the material presented in this report will demonstrate the techniques developed which can be utilized to define the environment at any point of interest.

Various techniques for electron beam diagnostics have been developed to measure the above-mentioned beam parameters with varying degrees of accuracy and/or resolution.[9-12] These techniques include the use of total stopping calorimeters to measure beam energy density, thin calorimeters to measure the energy deposition in thin samples (a linear array of thin calorimeters can be used to determine energy deposition profiles), a number of different passive dosimetry materials to measure energy deposition, magnetic spectrometers or differential energy absorption techniques to obtain spectral energy information, etc.

In Section II, the electron beam diagnostic techniques we have employed are described in detail. In addition, information relative to space charge effects in the dielectric passive dosimetry materials employed are presented.

In Section III, results obtained from the application of these techniques to the electron beam associated with the Sandia Laboratories Model No. 705 Febetron No. 1 are presented and, whenever practicable, are compared with the results obtained by other investigators. In addition, results obtained for the Hermes I electron beam are presented in Appendix B.

II. EXPERIMENTAL TECHNIQUES

Definition of an electron beam environment should include the determination of (1) typical energy deposition profiles in various materials, (2) the beam energy density, (3) the beam current time history and associated charge release, and (4) electron differential energy spectrum information. These quantities are, in general, spatially dependent and in some cases are also found to be dependent upon (1) the magnitude of the magnetic focussing field, if employed, (2) variations between supposedly identical electron tubes, (3) gas pressure in the drift tube and/or experimental apparatus, (4) the extent of the electron return path to the source machine, (5) accelerating potential variations, and (6) the specific configuration and composition of the experiment being conducted in the electron beam.

In Part A of this section, techniques are described for making absorbed dose and energy density measurements; in Part B, transient characteristics are considered; and in Part C, techniques for obtaining spectral energy information are discussed.

A. Dose and Energy Density

Energy deposition and incident beam energy density measurements are made, for the most part, using either thin active calorimeters or thin passive dosimetry materials in the case of the former, and total stopping calorimeters or linear stacks of thin calorimeters or passive dosimetry samples for the latter. The calorimetric technique requires, in the main, only a measurement of the temperature rise of the calorimeter and knowledge of the temperature dependent heat capacity of the calorimeter material. The utility of the passive materials depends upon the extent to which exposure induces changes in various of their material properties such as optical transmission, fluorescence radiation yield, etc.

Calorimetry

The use of calorimeters to monitor pulsed electron beams will, depending upon the calorimeter geometry employed, yield the energy absorbed in the

calorimeter or, correcting for backscattering and bremsstrahlung energy loss, the beam energy density incident upon the calorimeter.

The choice of calorimetric materials is, of course, somewhat arbitrary and usually the result of several compromises. The materials that have been employed thus far for calorimetric measurements are graphite, aluminum, and copper.* Aluminum was chosen because relatively thin detectors may be easily fabricated and results obtained can be readily compared with existing theoretical energy deposition data. Graphite, of course, exhibits excellent stability in high energy density beams and is used mainly for making high energy density measurements.[13] The ease of bonding thermal junctions to relatively massive specimens of copper was a prime consideration in the fabrication of copper calorimeters.

The use of sufficiently thin calorimeters results in a minimal perturbation to the incident electron beam and in the measurement of a thin-sample dose to the calorimetric material.

The thin calorimeters (Fig. 2.1) used in the thin-sample dose measurements on the 705 Febetron were made of 5 mil aluminum foil of various geometries. Chromel-alumel thermocouples were used as the temperature sensors.** Junctions were formed by spot welding the thermocouple wire (0.5 mil to 5 mil wire has been employed) to the lip of each calorimeter disc (Al) to complete the calorimeter. Since a change in temperature is all that is required, the junctions of the thermocouple wires to the copper leads carrying the signal to the recording apparatus served as the reference junction.

Graphite was also used in the fabrication of thin calorimeters that can be used in high energy density electron beams. These calorimeters were fabricated by electro-depositing 2 to 3 mils of copper to the surface of a bulk

---

*More recently, titanium, molybdenum, and tantalum have been added to the selected calorimeter materials. Titanium was chosen for its usefulness in high energy density beams and molybdenum and tantalum were chosen to obtain information representative of intermediate and high Z materials, respectively. Results obtained using Ti and Ta calorimeters on the Sandia Hermes I facility are presented in Appendix B.

**More recently, chromel-constantan thermocouple wire has been employed in some situations because of its greater output per unit temperature rise; i.e., ~ 0.06 mV/$\circ_C$ versus ~ 0.04 mV/$\circ_C$ for Cr-Al.

SILVER PHOSPHATE GLASS

COBALT GLASS

CINEMOID

CINEMOID DISCS

5 MIL Al CALORIMETER

TOTAL STOPPING Cu CALORIMETER

TOTAL STOPPING Al CALORIMETER
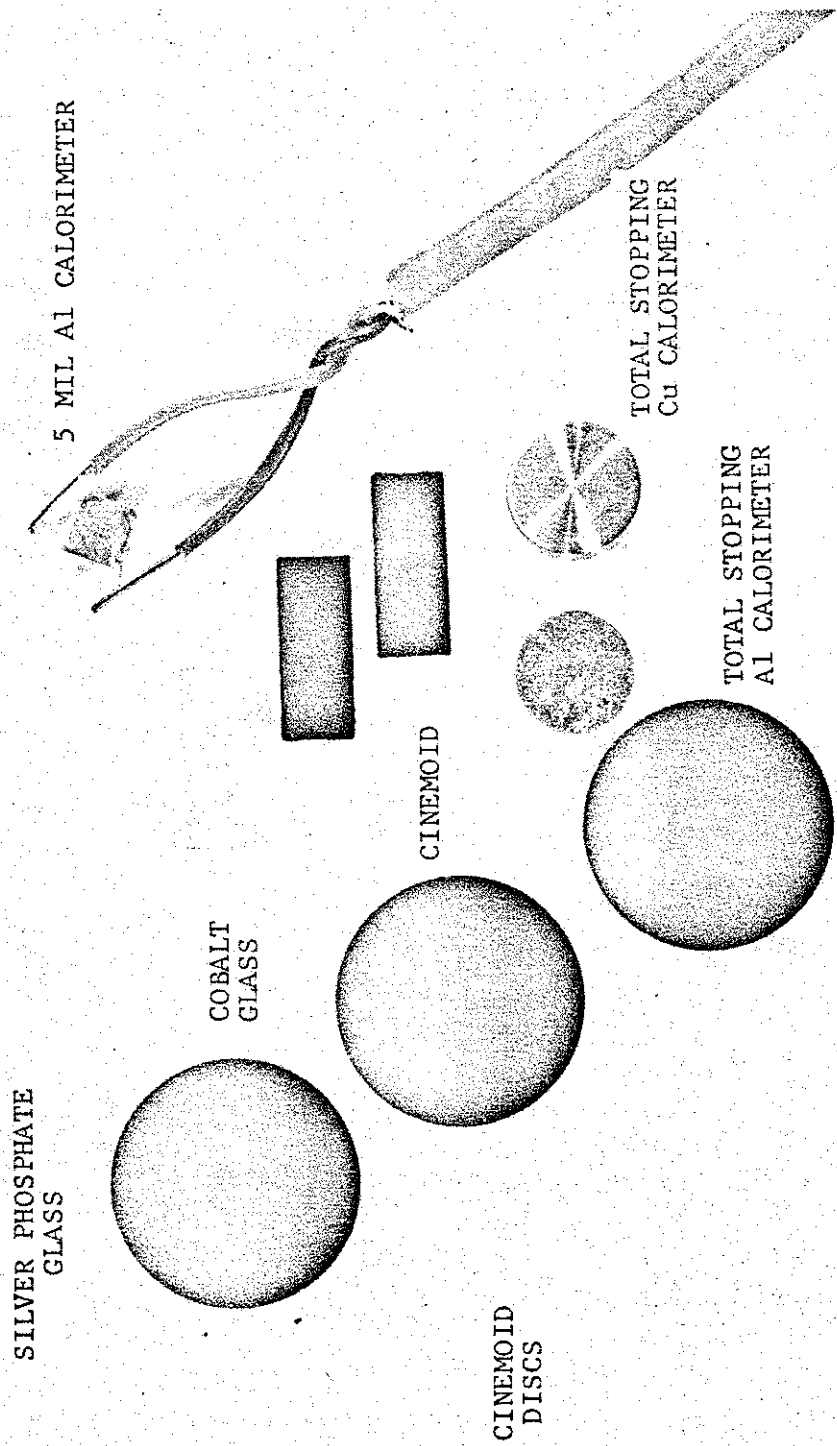
Figure 2.1a.   Calorimeters and passive detectors

13

TOTAL STOPPING ALUMINUM CALORIMETER
ENCLOSED IN AN ALUMINUM EQUILIBRATOR
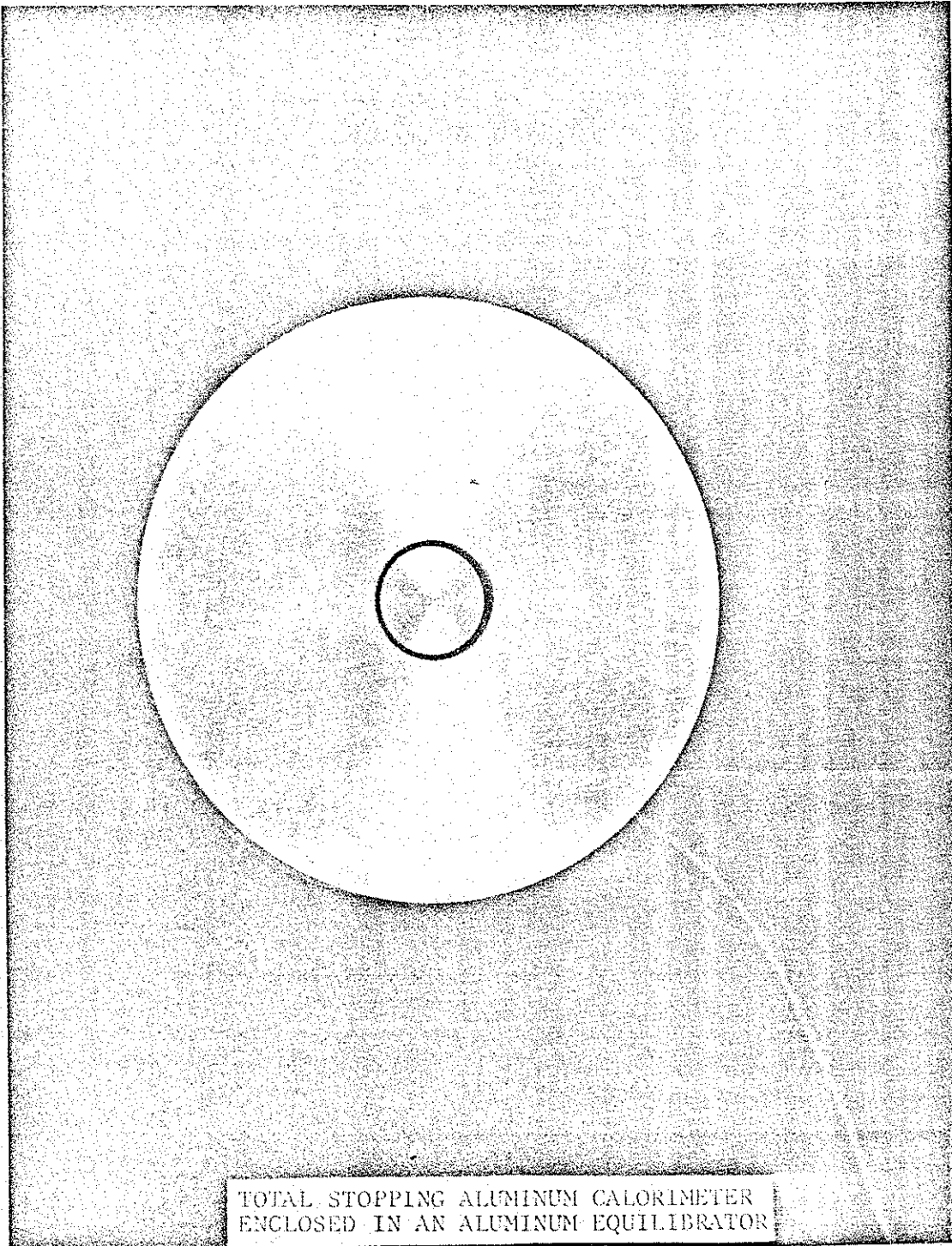
Figure 2.1b.   Calorimeters and passive detectors

graphite slab. The bulk graphite was then sliced into 30 mil thick by one centimeter square absorbers. A thermal junction of 5 mil chromel-alumel wire was silver soldered to the 30 mil surface of the graphite. The individual calorimeters were then placed in a linear array in order to determine energy depositions in graphite. These "linear array calorimeters" are described in more detail in Appendix B and typical results, obtained on the Sandia Hermes I facility, are presented.

The observed output of any of these systems yields immediately the beam energy absorbed in the calorimeter material, providing radiation heat transfer is negligible, since the absorbed energy is simply

$$E_{abs} = \int_{T_1}^{T_2} C_p(T) dT \quad , \tag{2.1}$$

where C_p is the heat capacity of the calorimeter material and $T_2 - T_1$ is the temperature rise of the calorimeter. For some materials, over rather small temperature changes, $C_p(T)$ is approximately a constant value and the above becomes

$$E_{abs} \approx C_p \Delta T \quad . \tag{2.2}$$

In addition to thin calorimeter measurements (used for energy deposition determinations), infinitely thick calorimeters (thickness greater than the electron range) can be used to measure the incident electron beam energy density (cal/cm^2 incident). Copper calorimeters (Fig. 2.1) of the same cross sectional area as the thin aluminum calorimeters have been used to measure the electron beam energy density output of the Febetron 705. These calorimeters are required to be at least as thick as the range of the most energetic electron to be measured. Thicknesses greater than the maximum range anticipated are of no consequence, as long as the temperature rise is measurable. The copper calorimeters used in the Febetron 705 measurements were 75 mils (1.68 gm/cm^2) thick (the range of a 2 MeV electron, the theoretical maximum electron energy for the Febetron 705, is 1.43 gm/cm^2 in copper) and are therefore infinitely thick to the electrons. The temperature sensing element used with this calorimeter was a chromel-alumel thermocouple made of #30 (10 mil) gauge wire and was silver soldered to the back surface of the copper

disc. Additional infinitely thick calorimeters to be used with higher energy-density machines were fabricated from graphite.* These calorimeters are of the same cross sectional area and configuration as the thin graphite calorimeters but are infinitely thick to 5 MeV electrons; i.e., 2.92 gm/cm² or 0.65 inch. Two mils of copper is electro-deposited on the back surface of such a calorimeter and a chromel-alumel junction of #30 gauge wire is silver soldered to this copper backing.

The incident beam energy density, as determined using either of these infinitely thick calorimeters, is obtained directly from the temperature rise in the calorimeter (for negligible backscattering and bremsstrahlung corrections),

$$I_B(cal/cm^2) = \int_{T_1}^{T_2} \Delta h \ C_p(T)dT \simeq \Delta h \ C_p \Delta T \qquad (2.3)$$

where Δh is the thickness of the calorimeter in gm/cm²; i.e., the calorimeter thickness times its density.

At this point it should be mentioned that care must be taken in the use of infinitely thick calorimeters or linear array calorimeters in the region of the pinch of an electron beam. In this situation electrons can enter through the sides of the calorimeter and lead to erroneously high beam energy-density measurements. In those situations where the incident electron beam possesses a substantial angular dispersion at the position of the calorimeter, an equilibrator (as shown in Figure B-2) must be employed in order to eliminate this side effect.

In actual measurements, for either thin or infinitely thick calorimeters, the output of a calorimeter, of the order of millivolts, is first amplified with an appropriate DC amplifier and then recorded on an electro-mechanical strip chart recorder or digitized and recorded on paper tape.

Although large electrical transients are present during the discharge of electron source machines, the thermal, electrical, and mechanical

---

*A segmented planar-array of graphite calorimeters is presently being employed on high energy-density beams in order to make low spatial-resolution beam-profile measurements.[13]

response of this measuring system is sufficiently slow so that the observed signals are completely devoid of any evidence of electrical transients after about one second. Additionally, the thermal decay of the system in air or vacuum is sufficiently slow so that extrapolation of the observed signal to zero time is easily done by making a semi-log plot of the observed voltage versus time.

The fact that the temperature dependence of C_p for the calorimeter materials and the temperature versus millivolt calibration of most thermocouple materials are known, the use of calorimeters for energy absorption determination represents an absolute measurement, at least within the uncertainty in the specific heat, with the following possible exceptions. Thermal equilibrium may not be obtained prior to thermal decay; i.e., heat conduction along the thermocouple lead wires commences before the bulk of the calorimeter and its sensor, the thermocouple, achieve the same temperature. The magnitude of this effect is not accurately known at present, but is estimated to be of the order of 5 to 10 percent for energy absorption determinations using thin aluminum calorimeters with chromel-alumel thermocouple leads of a few mil diameter. Two other losses of energy that may occur in the use of thin calorimeter systems are those due to bremsstrahlung production and electron backscattering. Bremsstrahlung losses may be estimated by[14]

$$\epsilon = \left[\left(d\xi_o \right) R / \tau_o \right], \text{ where} \tag{2.4}$$

$(d\xi_o, R = 1/\rho \ (dE/dx) \ t_{Rad}$, provided t, the thickness of the calorimeter, is less than t_{Rad}, the radiation length of the calorimetric material, and τ_o is the initial energy of the incident electrons. Insertion of values appropriate to the Febetron 705 in the above equation yields for the bremsstrahlung losses, in thin aluminum calorimeters

$$\epsilon \doteq 0.001 \approx 0.1\% \ .$$

The backscattering of electron energy is estimated from the calculations of Berger[15] to be about 3 percent of the incident energy for this machine. Figure 2.2a shows the magnitude of bremsstrahlung and backscattering losses by electrons in thin targets for several materials. These latter two effects do not, however, affect the ability of calorimeters to make energy deposition measurements. Only thermal loading and radiation heat transfer affect this.
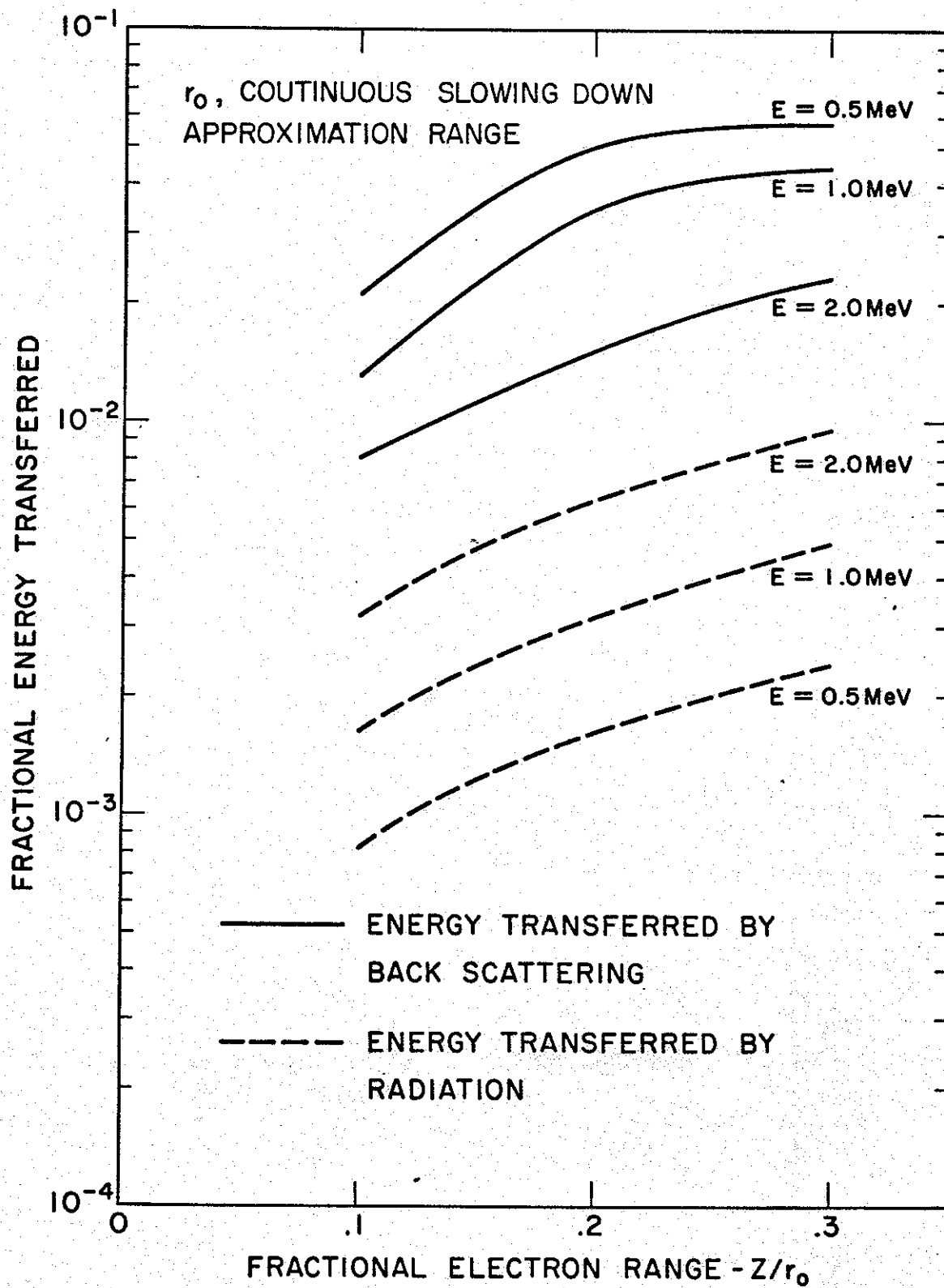
Figure 2.2a. Electron energy dissipated by backscattering and radiation in thin targets

In the case of infinitely thick calorimeters, uncertainties in the measurement of the incident electron beam energy density result from all four of these effects; i.e., the thermal loading effect, radiation heat transfer, bremsstrahlung losses, and backscattered electron energy loss. Note the bremsstrahlung and backscattered losses must be considered in this case since the infinite calorimeter is used to determine the total energy of the intercepted beam. Thermal loading losses are again estimated to be on the order of 5 to 10 percent for the infinitely thick aluminum calorimeters employing the same thermocouple wire as for the thin aluminum calorimeters. Bremsstrahlung losses for thick absorbers are estimated from[14]

$$\epsilon = \frac{3 \times 10^{-4} \ Z\tau_o}{1 + 3 \times 10^{-4} \ Z\tau_o} \tag{2.5}$$

where again τ_o equals the initial kinetic energy of the incident electrons. The above yields, for bremsstrahlung losses on the Febetron 705 using thick copper calorimeters,

$$\epsilon = 0.033 \approx 3\% \quad .$$

Backscattered energy loss is estimated from the experiments of Wright and Trump[16] to be approximately seven percent for conditions typical of the Febetron 705.

Electron energy escape, in infinite targets, due to bremsstrahlung losses and backscattering are presented in Figure 2.2b for various energy electrons in several different materials.

It should be kept in mind that if the energy deposition of an electron beam is measured with either a thin or an infinitely thick calorimeter of a certain material, then, in order to determine the deposition in another material, the difference in bremsstrahlung production and electron back-scattering for the two materials must be considered.

Passive Materials

In addition to calorimeters, absorbed dose and incident energy density measurements can be made with radiation sensitive glasses and many different dye-loaded plastics. A single thin detector yields, of course, absorbed
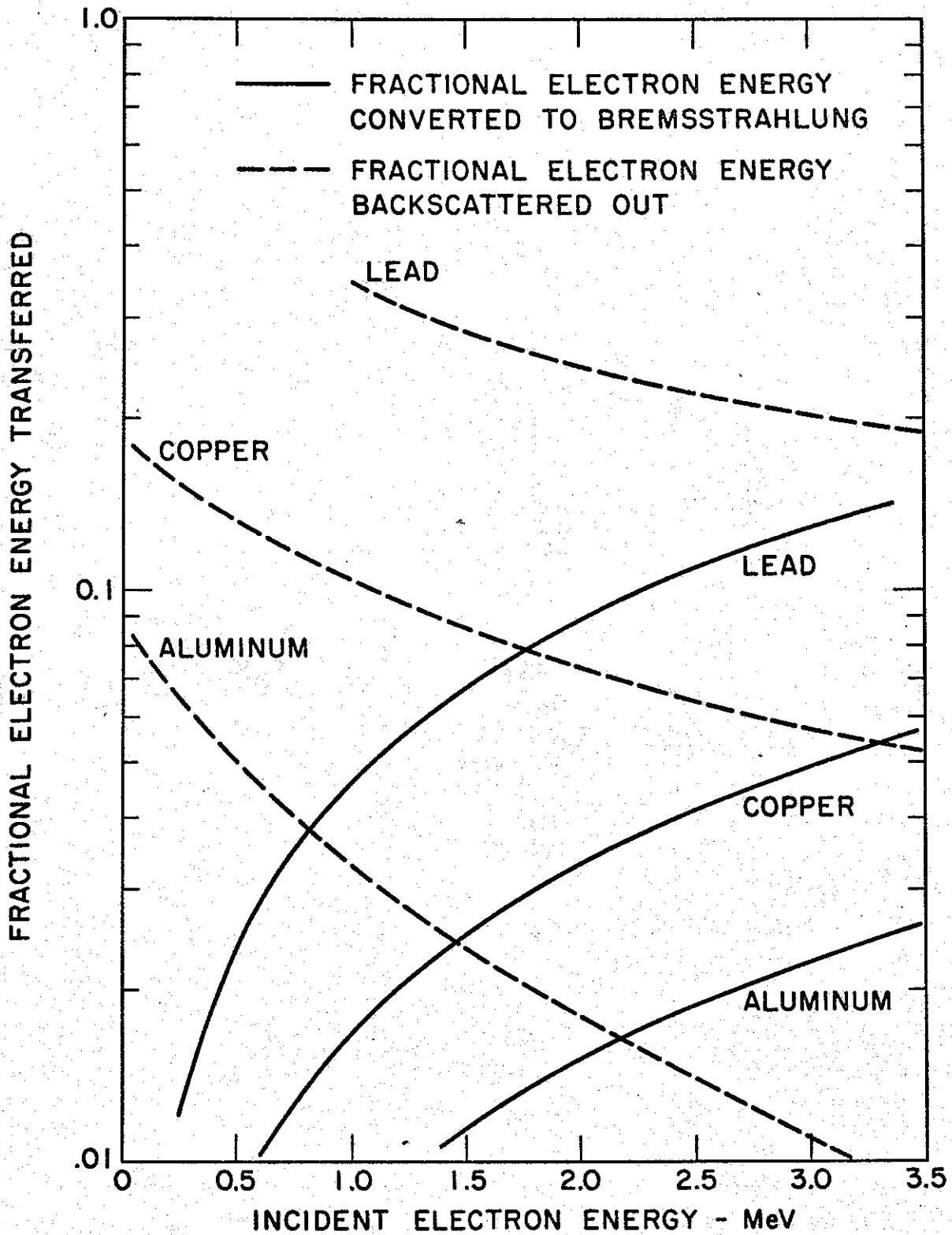
Figure 2.2b. Electron energy dissipated by backscattering and radiation in thick targets

dose information; while use of a detector infinitely thick to the incident radiation would result in a measurement of the incident beam energy density excluding backscattering and bremsstrahlung energy loss corrections.

Dye-loaded organics have been used to monitor photon and electron beams for a number of years. The colored plastics used at our laboratory were first suggested by the USNRDL[17] as a result of an extensive investigation aimed at finding some passive detector capable of measuring absorbed radiation doses extending into the megarad region. In the course of the USNRDL investigation, approximately 61 different types or colors of Cinemoid (obtainable from Kliegel Bros., Long Island City, New York) were exposed to 50 megarads of Co^{60} radiation and the resulting change in light transmission as a function of wavelength measured. As a result of these steady state radiation experiments, it was determined that two of the plastics --- #25 Purple and #48 Bright Rose --- showed promise as materials for high level dosimetry. Physically, these materials are available in sheets with a nominal thickness of 10 mils. The density has been determined to be 1.36 gm/cm^3. Chemically, both the #48 and #25 appear to be almost identical, the main difference being in the dye used for tinting.

The response of #48 Bright Rose and #25 Purple Cinemoids to steady state irradiations (Co^{60}) are plotted in Figure 2.3.* On the abscissa is plotted absorbed dose to water as measured with ferrous sulphate (a fundamental method of measuring absorbed gamma dose) on the Sandia Co^{60} Gamma Irradiation Facility; while on the ordinate is plotted the change in optical density of the plastics. The greatest change in optical density for a given absorbed dose of the #48 Cinemoid occurs at 520 mμ, while that of #25 Cinemoid occurs at 435 mμ.

The optical density referred to here is as usually defined:

$$OD = \log_{10} \left(\frac{T_o}{T}\right)$$ (2.6)

---

*It has recently been found that the calibration curve for #25 Purple Cinemoid is dependent upon the ambient environment during exposure and/or environmental preconditioning of the samples prior to exposure.[18,19]
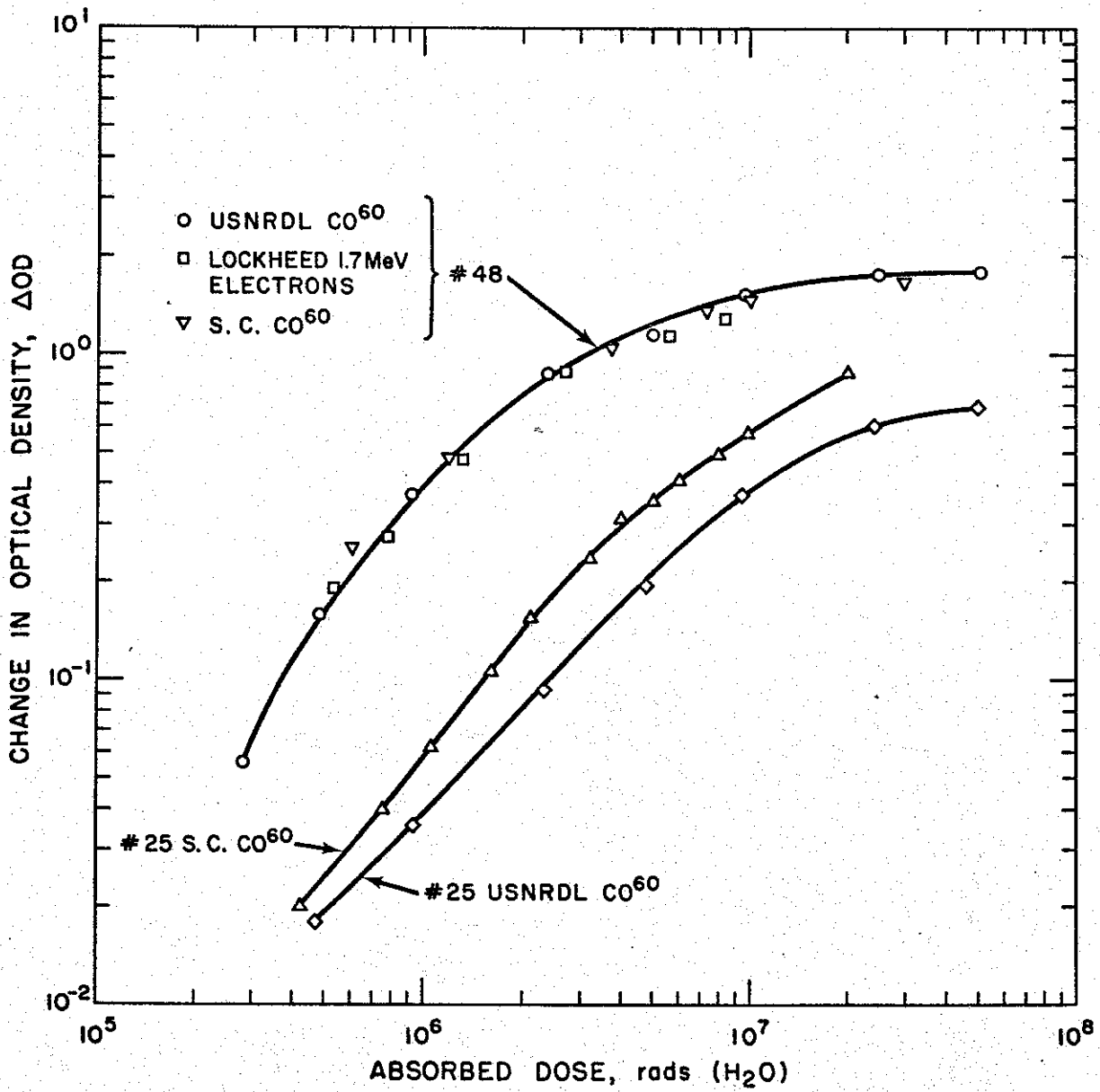
Figure 2.3.   Calibration Curve - ΔOD vs. dose for #25 and #48 Cinemoids

where T_0 and T are the incident and transmitted light intensity at the appropriate wavelength. The change in optical density for a sample is then simply

$$\Delta OD = \log_{10} \left(\frac{T_1}{T_2}\right) \tag{2.7}$$

where T_1 and T_2 are the transmitted intensities, at a given wavelength, for the unirradiated and irradiated conditions, respectively, as determined with an appropriate spectrophotometer.

In reference to the dose versus the change in optical density curves (Figure 2.3), the uppermost curve represents the response of #48 Bright Rose and the two lower curves represent the response of #25 Purple Cinemoid. The #48 Bright Rose is a composite of three independent determinations -- USNRDL Co^{60}, Lockheed Research 1.7 MeV electron, and the Sandia Co^{60} exposures.

The intermediate curve is the Co^{60} response of #25 Purple Cinemoid irradiated in the Sandia Co^{60} facility, while the lowest curve is the Co response of the #25 Cinemoid as determined by USNRDL. The difference in response for these two irradiations has no ready explanation but may be the result of differences in the Cinemoid batches used in the two experiments.

The calibration or response curves presented in Figure 2.3 are based upon the absorbed dose in water for the purpose of comparison only. In actual practice the absorbed dose as measured with ferrous sulphate is adjusted to the absorbed dose in the material of interest, so that radiation measurements with a material reflect actual energy deposition in that particular material.

The adjustment of absorbed dose in water to absorbed dose in Cinemoid is readily computed from

$$\text{Dose(Cine)} = \frac{\mu_E(\text{Cine})}{\mu_E(\text{H}_2\text{O})} \ \text{Dose(H}_2\text{O}) \tag{2.8}$$

23

where μ_E(Cine) and μ_E(H$_2$O) are the energy absorption coefficients, at the calibration energy, for Cinemoid and water. This adjustment is, of course, reflected in the calibration of the Cinemoid.

In addition to the plastics, radiation sensitive glasses can also be used as passive dosimetry materials in monitoring sufficiently diffused and/or low energy density electron beams. The glasses used in this laboratory are of two types --- silver meta-phosphate (commonly referred to as silver phosphate) glass and cobalt glass obtained from Bausch and Lomb. These glasses are 15 mm by 6 mm in cross-sectional area and 1.5 mm thick for the "thick" cobalt and silver phosphate glasses; however, the "thin" glasses, while having the same cross-sectional dimensions as the thick glasses, are 0.25 mm thick.

These glasses respond to radiation by becoming increasingly opaque to certain wavelengths of radiation as the absorbed dose increases. The optimum response of both glasses for use at this laboratory has been determined to occur at a wavelength of 360 mμ. The techniques of reading and calibration of these glasses are then completely analogous to the Cinemoid plastics. Examples of the calibration curves of the glasses are given in Figures 2.4a and 2.4b. As in the case of the plastic materials, absorbed dose can be obtained from one thickness of glass, but in order to determine the incident-beam energy density, an infinitely thick stack of glass is required.

One further consideration, when the glasses are used, is that of the variation in the glass thickness. The variation in Cinemoid thickness is at most several percent whereas the glass exhibits as much as a 25 to 30 percent variation. For a uniform irradiation of the glass this means that, since the absorbed radiation is related to optical transmission, the apparent absorbed radiation dose will be a function of the glass thickness. In order to correct for glass thickness variations, the calibration curve could be expressed in terms of ΔOD/mm as in Figure 2.4 or several thicknesses of glass, selected at random, could be exposed to a known dose. Using this latter approach, the apparent absorbed dose plotted as a function of glass thickness is presented in Figure 2.5. These data have been normalized to unity correction at glass thicknesses of 0.25 mm and 0.23 mm, the nominal thicknesses for the cobalt and silver phosphate glasses, respectively. As may be anticipated, the apparent absorbed dose is a

24
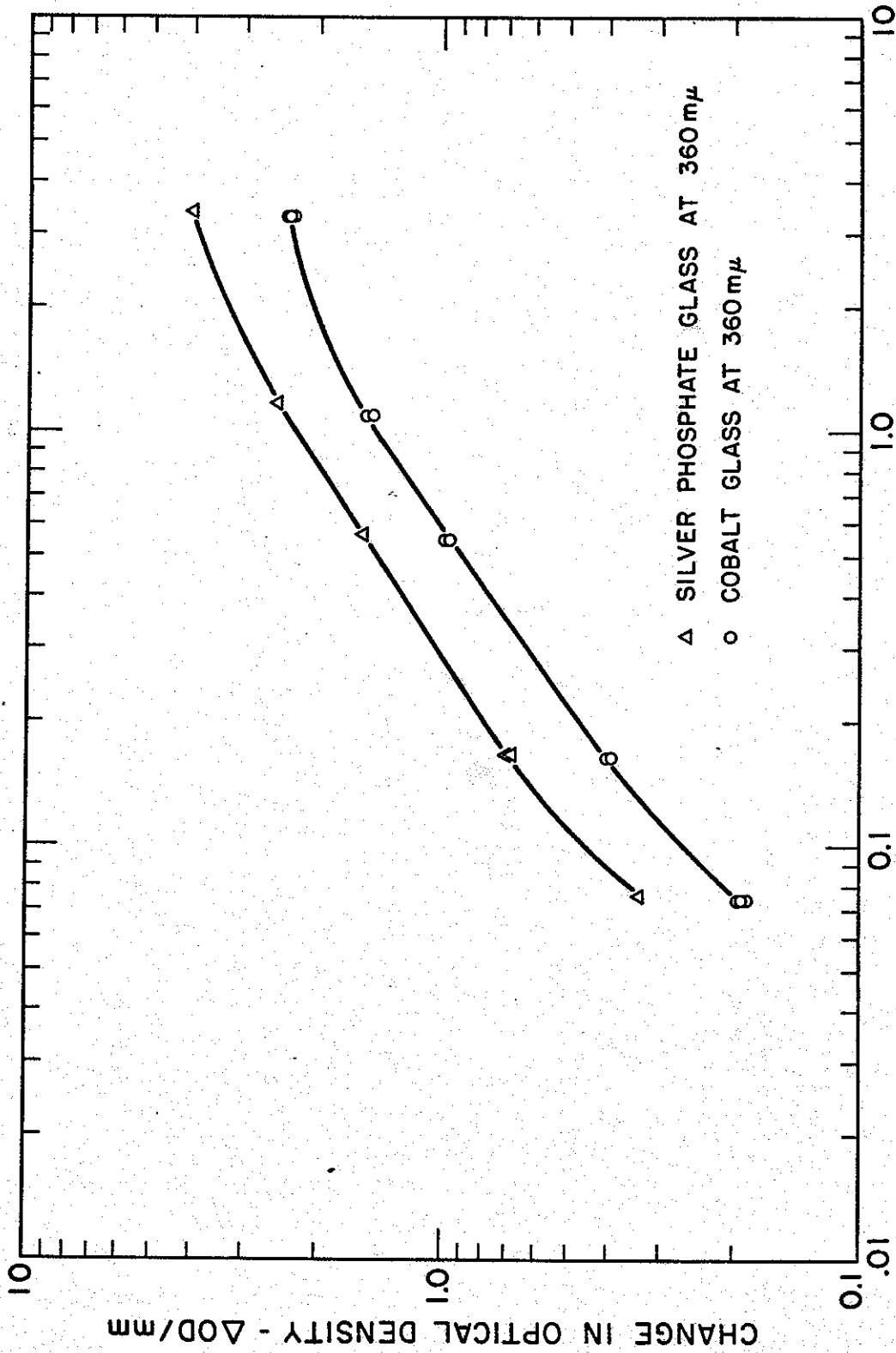
Figure 2.4a. Calibration Curves $\Delta OD/mm$ vs. dose for thin silver phosphate and cobalt glass
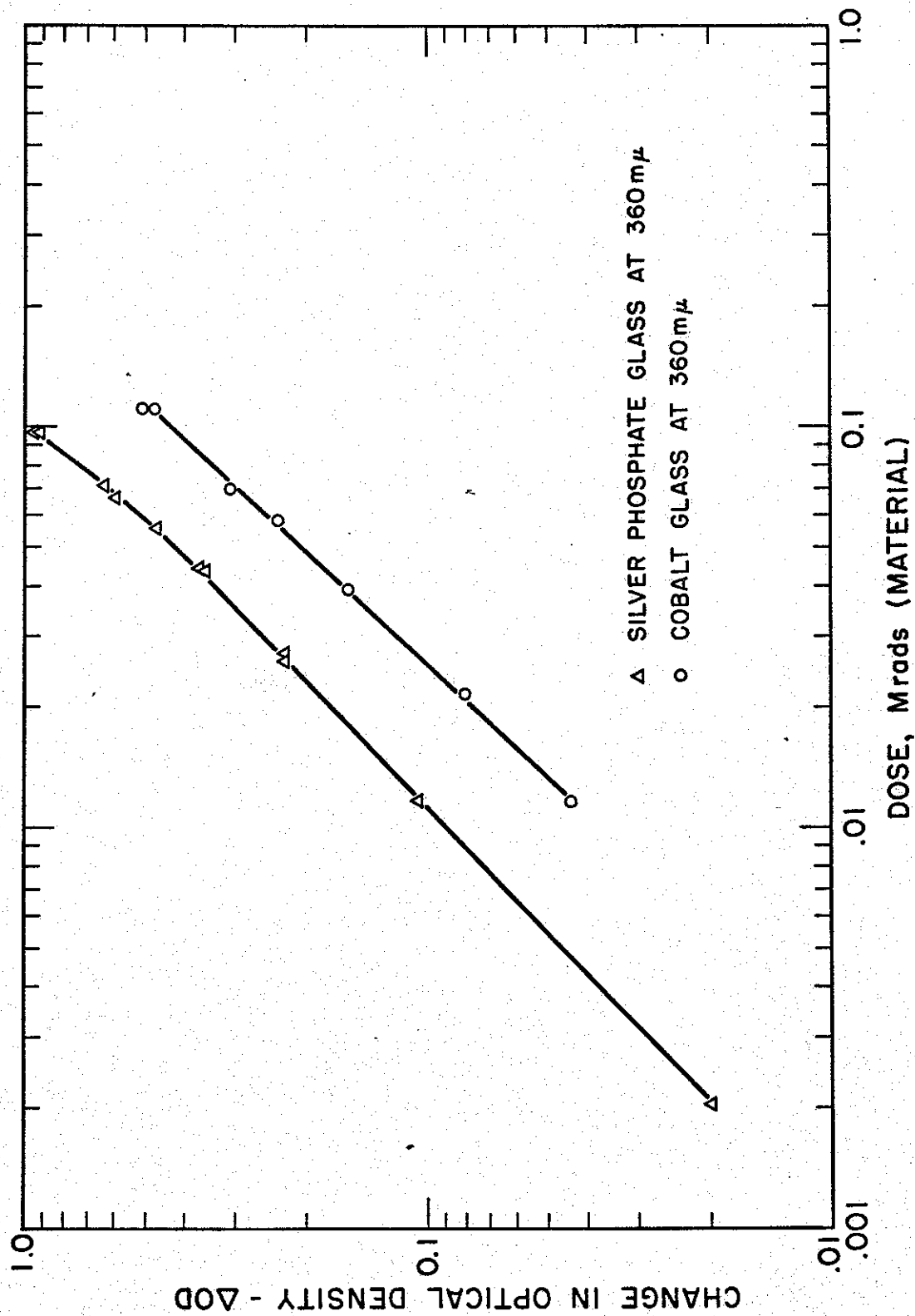
Figure 2.4b. Calibration Curves ΔOD vs. dose for regular silver phosphate and cobalt glass

△ SILVER PHOSPHATE GLASS AT 360 mμ

○ COBALT GLASS AT 360 mμ

DOSE, Mrads (MATERIAL)

CHANGE IN OPTICAL DENSITY - ΔOD

26
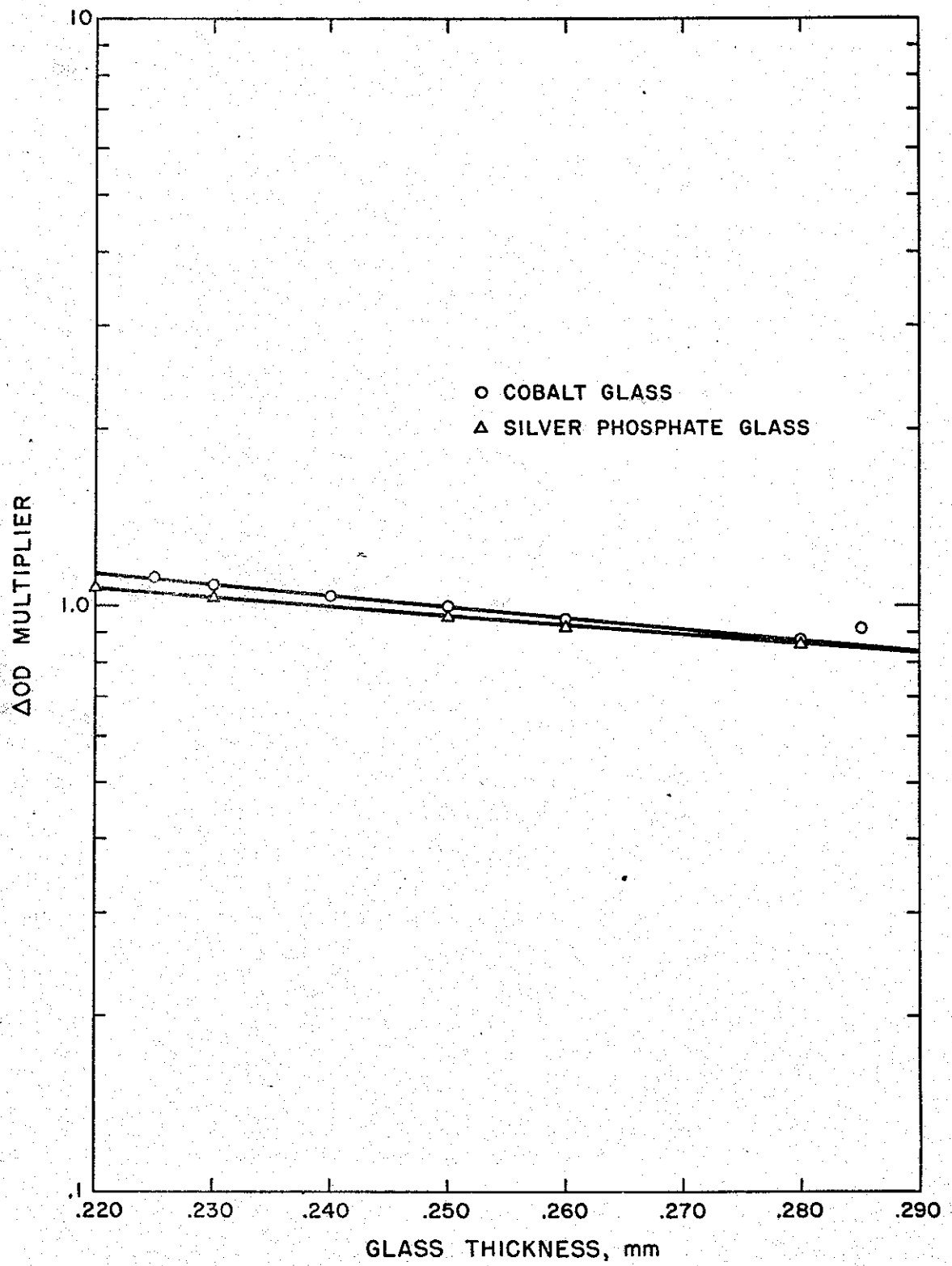
Figure 2.5. Correction factor - ΔOD multiplier as a
function of glass thickness

27

smoothly varying function of the glass thickness. The use of cobalt or silver phosphate glass then implies that careful account must be taken of its thickness. It should be emphasized that the glass calibration curves also reflect an adjustment from Rads(H_2O) to energy absorbed in the detector material of interest.

Reproducibility and accuracy of measurements using these passive detectors are dependent upon uniformity of the detector material -- both physically and chemically -- and the type of system used to read the detectors. Uncertainties in measurements arising from non-uniformities in the detector material can usually be removed by such pre-exposure expediencies as thickness measurements of the detectors and pre-irradiation transmission measurements. The reproducibility and accuracy of the readout system are, of course, dependent on the system employed and also on the nature of the spectral response curves of the detectors. The readout systems used in these measurements are the Beckman DK-2 and DU spectrophotometers. When considering the stated reproducibility and accuracy of the DK-2 spectrophotometer and applying this to the radiation response function of the detectors and, additionally, considering the precision reading ability of the spectrophotometer operator, dose measurements with a precision uncertainty of 10 percent are routinely possible when using these passive detectors. A few percentage point increase in accuracy and reproducibility are possible when using the DU system since the DU is inherently more accurate and the readout, being a null indication, allows for greater reading precision by the operator. These readout systems sample but a small portion in the center of the dosimetry samples so that edge effects should be minimized.

At this point it is appropriate to discuss an anomaly associated with the #48 Rose Cinemoid. The #48 Rose Cinemoid response to steady state radiation is more sensitive than that of the #25 Purple. However, when the #48 Rose Cinemoid is used to measure absorbed dose on pulsed electron sources, it consistently indicates lower absorbed dose than is measured by other methods, i.e., calorimeters and #25 Purple Cinemoid. The experience at Sandia, with Rose Cinemoid, was not unique since similar difficulties have been reported[1] for the Rose Cinemoid when it was used in pulsed electron environments. Due to this under-response resulting from rate-saturation, the use of #48 Rose Cinemoid should be confined to that of monitoring steady state environments, or to obtaining only qualitative beam information.

Applications

The calorimetry and passive dosimetry techniques described above can be employed in the determination of electron beam properties such as the spatial variation of the beam energy density as well as to yield information concerning the energy deposition profiles produced in various materials.

"Surface Dose" Measurements -- A thin detector absorbs only a fraction of the incident electron beam energy. The fraction absorbed is dependent on the thickness and composition of detector material and the energy of the incident electrons. In Figure 2.6 are presented some representative, calculated,[20] energy deposition profiles for monoenergetic electrons normal-incident on aluminum. It is apparent from these figures that, if a thin calorimeter is to measure an absorbed "surface dose," then it should be no more than several hundredths gram per square centimeter thick in order to minimize the effect of backscattering. The dose measured by an isolated thin detector will be less than that measured by an identical detector backed by an infinitely thick sample of the same material as a result of the absence of backscattered electrons in the former case. An example of this effect is shown in Figure 2.7 where energy deposition profiles are presented for a number of different stack thicknesses exposed on the Sandia Model 705 Febetron No. 1. As can be observed from the figure, the absorbed dose for 0.0330 gm/cm^2 (one thickness) of Cinemoid is approximately 25 percent lower than the absorbed dose to the front thickness in a stack of five samples. Also, the dose delivered to the interior of the intermediate thickness stacks is somewhat less than that delivered to the more nearly infinite-thickness stacks. This increase in absorbed dose to the thicker stacks indicates the increasing importance of multiple electron scattering with increasing sample thickness.

Surface dose measurements using a single large piece of passive dosimetry material can, therefore, only yield approximate information concerning the spatial variation of the beam intensity inasmuch as energy absorbed and not energy density is measured. It is not possible to convert directly from surface dose to beam energy density without knowledge of the electron energy spectrum (which may be spatially dependent) or energy deposition profile for all spatial points of interest.
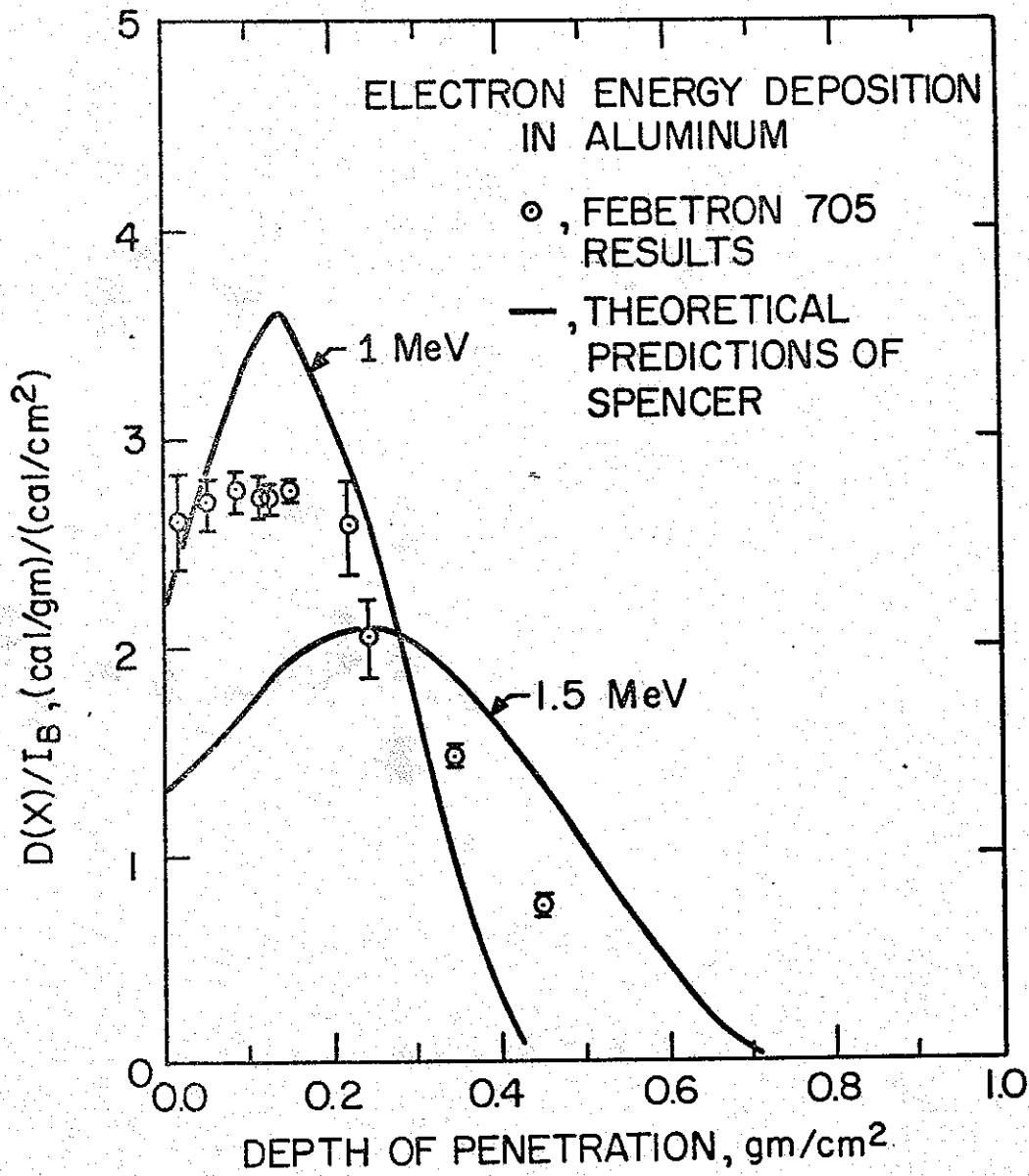
Figure 2.6. Electron energy deposition in Al vs. penetration - theoretical and experimental
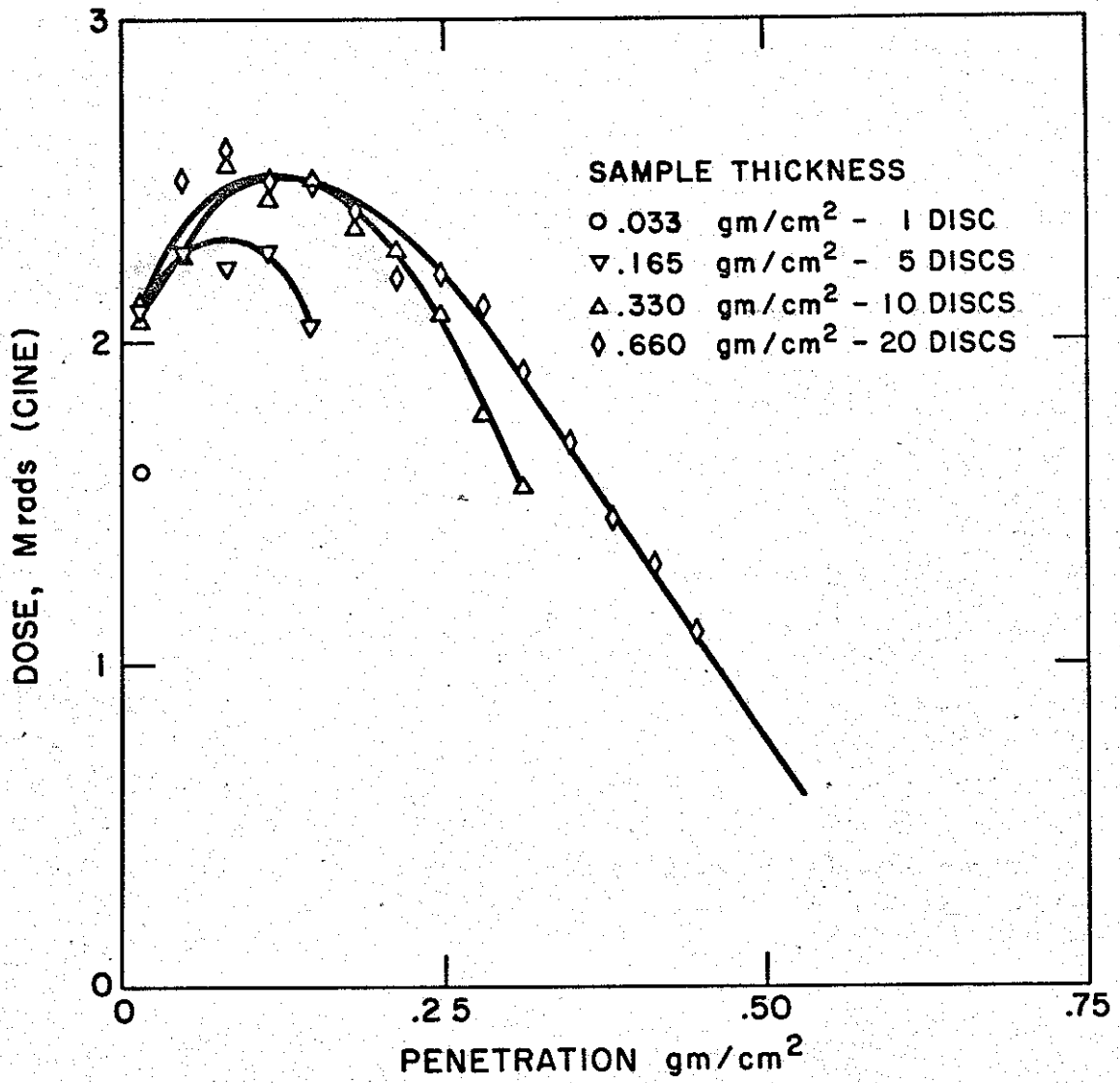
Figure 2.7. Electron energy deposition vs. penetration
in various thickness Cinemoid samples

Energy Deposition Profiles -- It is possible to obtain energy deposition profiles by stacking detectors perpendicular to the electron beam axis and of sufficient total thickness to be of the order of the extrapolated range of the most energetic electrons in the beam.

As can be seen in Figure 2.6, the energy deposition produced by mono-energetic electrons in aluminum increases until a maximum is achieved and then decreases with increasing penetration. It is observed that increasing the initial energy of the incident electron increases the penetration depth at which the maximum energy deposition occurs. The deposition peaking may be explained on the basis of electron slowing down and subsequent backscattering with the backscattered electrons contributing to the energy deposition.

Since most pulsed electron beam machines emit a spectrum of electrons, the solid curves in Figure 2.6 are not completely representative of a dose-depth curve for these machines. The dashed curves in Figure 2.6 are experimentally determined electron deposition curves for the Sandia Model 705 Febetron No. 1 output ($E_{max} \approx 1.5$ MeV) as obtained with thin aluminum calorimeters. The relatively shallow penetration distance of the deposition maximum and large surface deposition are indicative of a large low-energy electron component or a substantial angular dispersion of the incident electron beam (this resulting in energy deposition closer to the front surface than for the case of normal incidence). For the case of non-normal incidence, there is a possibility that electrons can escape from the sides of an infinitely thick sample of material. It is, therefore, necessary to employ calorimeters or passive dosimetry stacks of a configuration such that the diameter or side dimension is much greater than the thickness or to use a suitable equilibrator (see Figure 2.1).

Figure 2.8 also presents energy deposition profile results typical of the Sandia Model 705 Febetron No. 1. The dashed curve was obtained using #25 Cinemoid, while the solid curve is the result of aluminum calorimeter measurements. Stacks of the Cinemoid samples or the glasses described above were exposed on a single shot, and the energy deposition to each sample of the stack was determined. The energy deposition profiles for aluminum calorimeters were measured as follows. The "surface" dose to an unshielded thin aluminum calorimeter was determined, and then progressively thicker aluminum shields were placed in front of the calorimeter
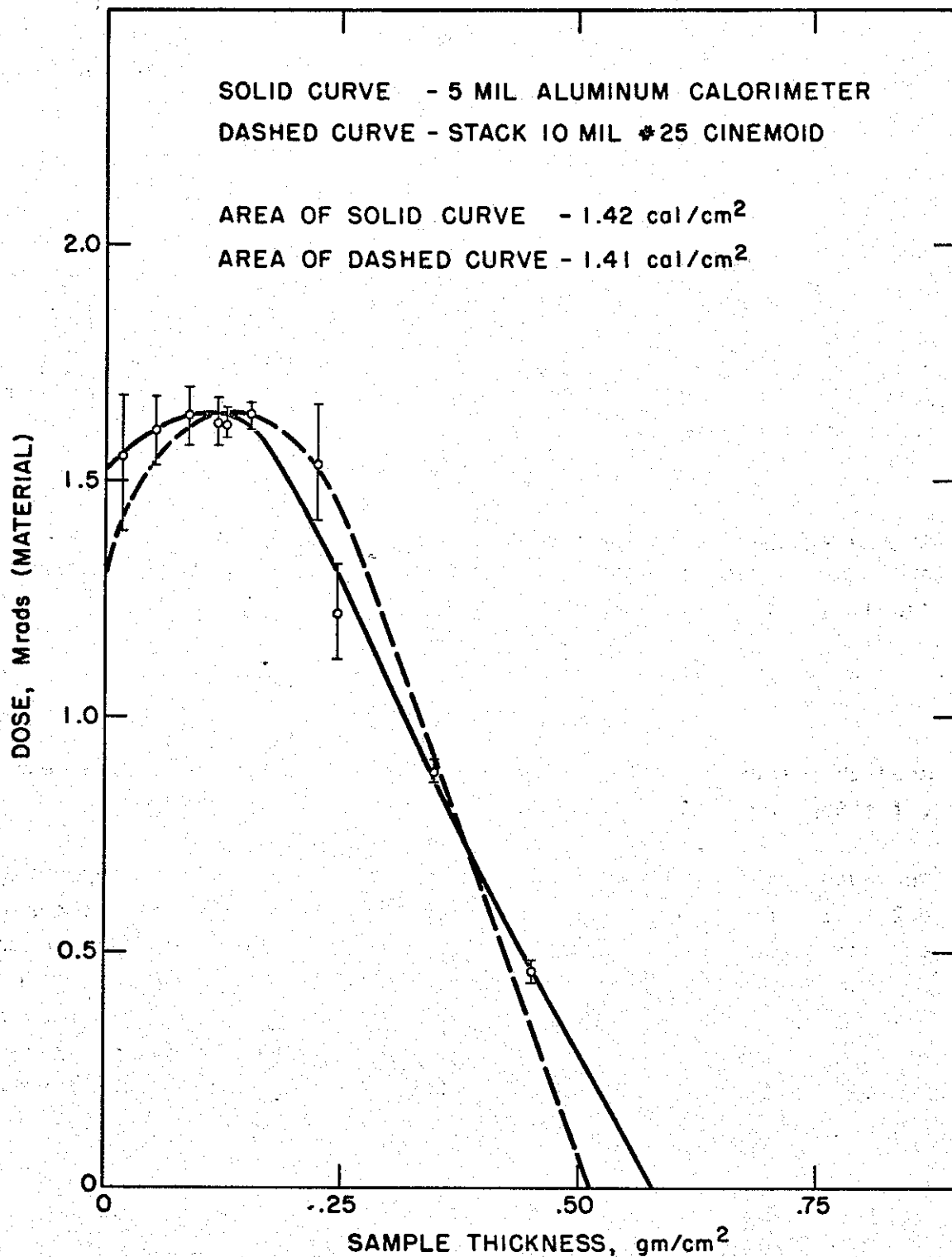
Figure 2.8.   Electron energy deposition in Al and #25 Cinemoid vs.
penetration for the Sandia Model 705 Febetron

and the variation in absorbed dose determined. By proper variation of the aluminum shield thicknesses, a characteristic dose versus depth curve is obtained as shown in Figure 2.8 (solid curve). The agreement between the beam energy density measured in these two cases may be fortuitous since the measurements were made on different tubes.

The electron stopping powers, $1/\rho \, dE/dx$, of many materials, in addition to being almost energy independent over broad energy ranges, show small variation between materials for a given electron energy.[21] Further evidence of the similarity of electron energy deposition in several materials is given in Figure 2.9. In this figure the integrated energy deposition is plotted as a function of sample thickness; i.e., the integral of the deposition profiles.

Beam Energy Density -- From what was said in the preceding paragraphs, it should be clear that the beam energy density, I_B, is obtained directly from the area under the energy deposition curve, i.e.,

$$I_B = \int_0^\infty D(x)\,dx, \ cal/cm^2 \ , \tag{2.9}$$

providing the stack is infinite in extent to the electrons in the beam and backscattering and bremsstrahlung corrections are negligible.

The curves (with the exception of the calorimetric data) appearing in Figure 2.9 are based upon a Co^{60} calibration in terms of energy deposition to the particular dosimeter material. As stated above, for an infinite stack the total area under the deposition curve represents the beam energy density. Table II.1 shows the agreement between the various materials, and, once again, the agreement of the beam energy density measurements should be taken lightly since different tubes were employed during the series of measurements summarized in this table.

Table II.1

Comparison of Energy Density Measurements

Detector Material	#25 Cinemoid	Cobalt Glass	Aluminum Calorimeter	Copper Calorimeter
Absorbed Energy (cal/cm^2)	3.0 ± 0.3	3.3 ± 0.3	3.1 ± 0.3	3.4 ± 0.3
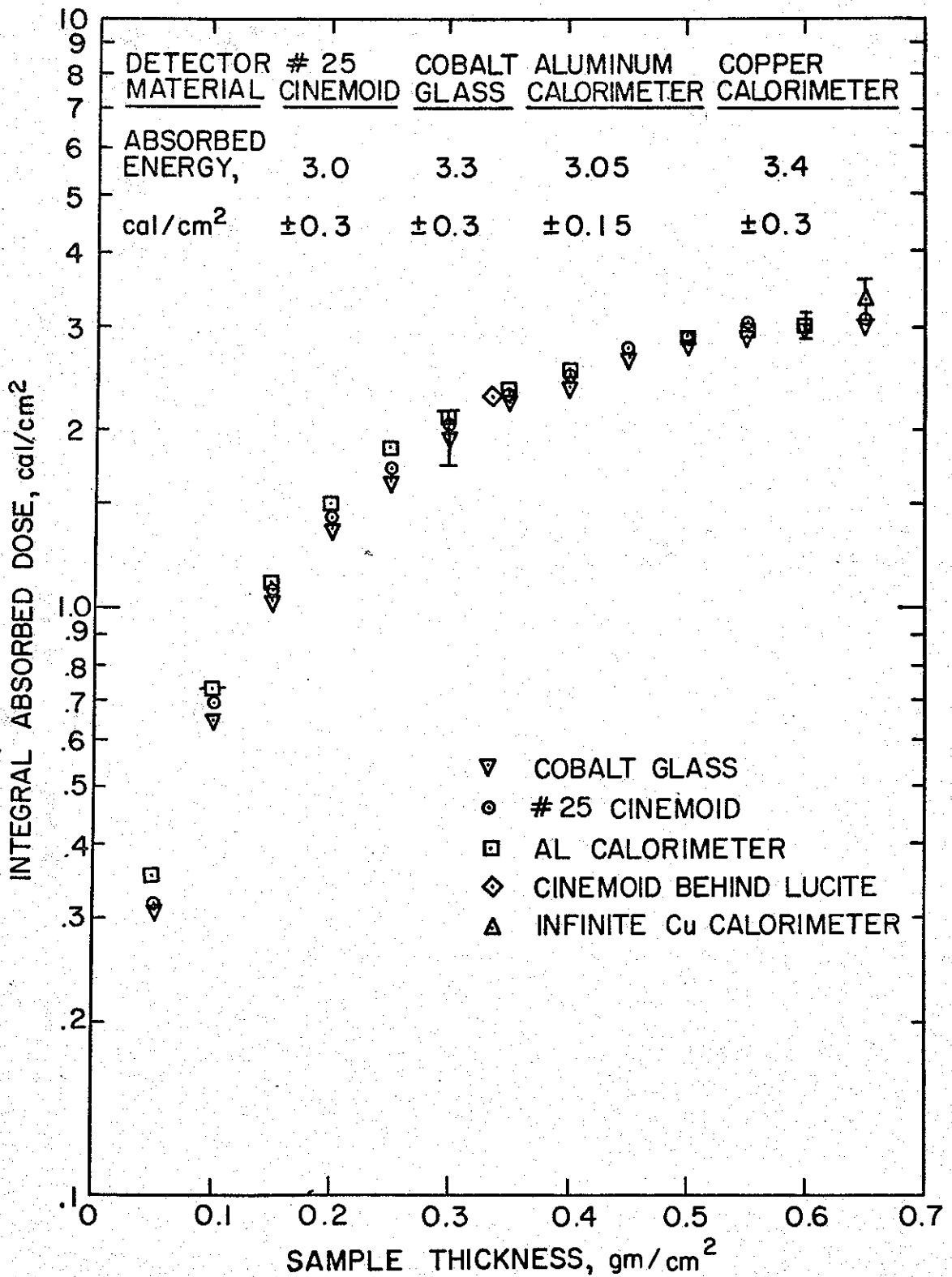
Figure 2.9. Integrated electron energy deposition in various materials vs. penetration for the Sandia Model 705 Febetron

In addition to yielding incident energy density information, the energy deposition profiles yield other information (e.g., the maximum electron energy in the beam and an effective electron energy for the beam) which will be discussed in more detail in Section II.C.

Information concerning the spatial variation of the beam intensity can be obtained from measurements of the energy deposition profile, and therefore beam energy density, at numerous positions on and off the beam axis.

B. Electron Beam Time Profiles

Monitoring of the instantaneous voltage across the electron source tube and of the instantaneous beam current can yield useful information concerning the rate at which energy is deposited (this can also be deduced from time history measurements of the x-rays produced when the electrons are stopped in a high Z target), approximate spectral energy information, and charge release information.

Voltage Monitor

A voltage divider network is commonly employed to monitor the tube voltage for these types of machines. This type of device senses the instantaneous tube voltage $V_T(t)$ and not the instantaneous anode-to-cathode voltage drop $V_{A-C}(t)$ (which determines the instantaneous electron energy $E_e(t)$) due to the presence of an inductive voltage drop in the tube shank during the pulse, i.e.,

$$E_e(t) = qV_{A-C}(t) = q\left(V_T(t) - L\frac{dI(t)}{dt}\right) \tag{2.10}$$

where L is the inductance of the tube and return path to ground and q is the magnitude of the electronic charge.

Current Monitor - Faraday Cup

Current measurements in this Laboratory have been made using the Faraday cup[22] shown in Figure 2.10.* The cup is evacuated and the center catcher

---

*This cup has been modified recently to allow for sampling of larger fractions of the electron beam through the use of an all-aluminum electron catcher and $1\,\Omega$ or so current viewing resistors. The Field Emission Model 1652 Electron Beam Monitor has also been employed for total charge release determinations.

cup is fabricated of graphite to minimize bremsstrahlung production. A lead liner is employed in order to reduce ionization in the residual air (operating pressure in the range of a few tens of microns) and in the coax connector (mounted in the back plate) which leads to the 50 Ω current viewing resistor. A 0.002 inch thick Ni window allows the electron beam to enter the cup housing. The beam intensity was attenuated by placing one of a set of copper apertures outside this window. The aperture sizes employed, when making measurements on the beam axis, were limited to diameters of 1/32" (4.94×10^{-3} cm^2) and 1/16" (1.98×10^{-2} cm^2) due to the fact that for larger apertures the voltage developed across the current viewing resistor leads to breakdown in the coax cable, i.e., RG-58, 50 Ω characteristic impedance.

In the electrical circuit employed with this Faraday cup, RG-58 cable carries the signal from the cup to a Tektronix Model 017-055 T50/N125 adaptor. This adaptor provides the 50 Ω current viewing resistance. A Tektronix Type 519 oscilloscope, with varying degrees of input attenuation is used to monitor the voltage pulse and therefore the associated beam current time history. Due to the rather small aperture sizes, the measurements sample only a portion of the beam as mentioned above. The charge collected is obtained from the time history of the beam current, i.e.,

$$Q = \int_0^\infty I(t)dt \quad . \tag{2.11}$$

Therefore, the charge determined in this way is representative of only a small portion of the total beam.

C. Energy Spectrum

As mentioned earlier in this section, it is possible to obtain some relatively crude spectral information from the energy deposition profiles obtained using either calorimeters or passive dosimetry materials.
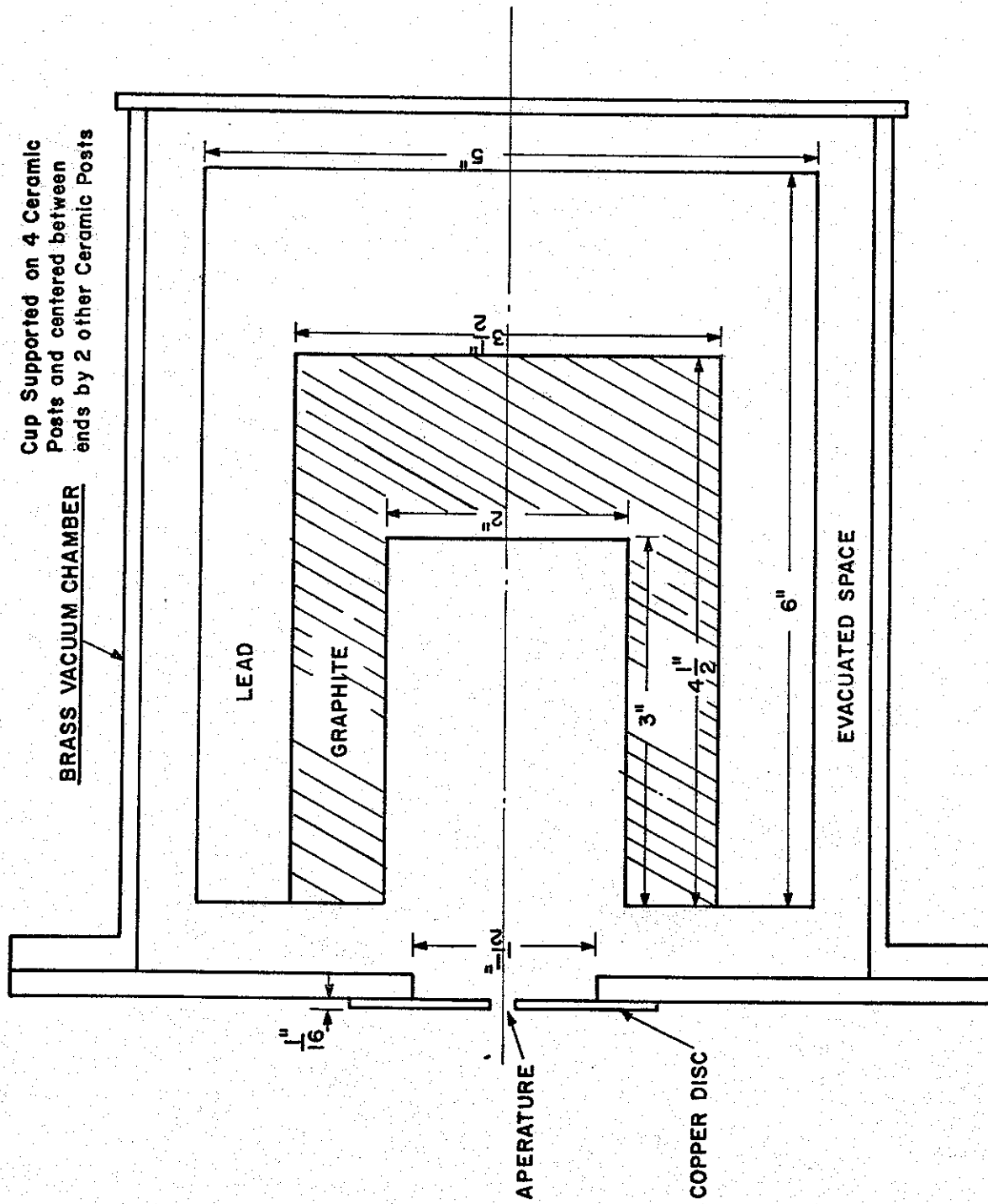
Figure 2.10. Faraday cup cross-sectional view

Beam Maximum Energy

The energy deposition profiles shown in Figure 2.8 can be extrapolated to zero dose, and the zero dose intercept with the abscissa then yields approximate information concerning the extrapolated range for the most-prominent high-energy electrons in the spectrum.

In the case of the aluminum results, a maximum electron energy is obtained from the range-energy relationship experimentally determined by Katz and Penfold[23] for beta particles and presented in Figure 2.11. In the case of Cinemoid, the extrapolated "range" may be converted to an approximate maximum electron energy by comparison to electron range versus energy tabulations.[21] A plot of range versus energy for a Cinemoid-like plastic (lucite) is given in Figure 2.12. The upper curve was obtained from this reference while the lower curve is a normalization of this curve to the experimental results obtained at an electron energy of 1.8 MeV on the Sandia Van de Graaff accelerator. The difference between these two at 1.8 MeV results from the fact that the calculations[21] predict the total electron path length rather than the depth of penetration, which is the smaller of these two due to the large angle scattering events which electrons experience when penetrating matter.

Beam Effective Energy

In addition to the maximum electron energy, an effective electron energy can be deduced from the energy deposition profile. In this determination the spectrum of electrons producing the energy deposition profile is assumed to be a monoenergetic source possessing a characteristic energy, the effective energy.

As shown in Appendix A, the ratio of the incident beam energy density, I_B, to the surface dose in an infinite stack of detectors, $D(o)$, for a normal-incident monoenergetic electron beam is related to the electron energy by

$$\frac{I_B}{D(o)} = \left.\frac{E}{\frac{dE}{dx}(E) \, J(o,E)}\right|_{E_{eff}} \equiv f(E_{eff}) \qquad (2.12)$$

Figure 2.11. Range vs. energy for electron penetration in Al

$$R = 412 \, E_0^{1.246 - 0.0954 \log E_0}$$
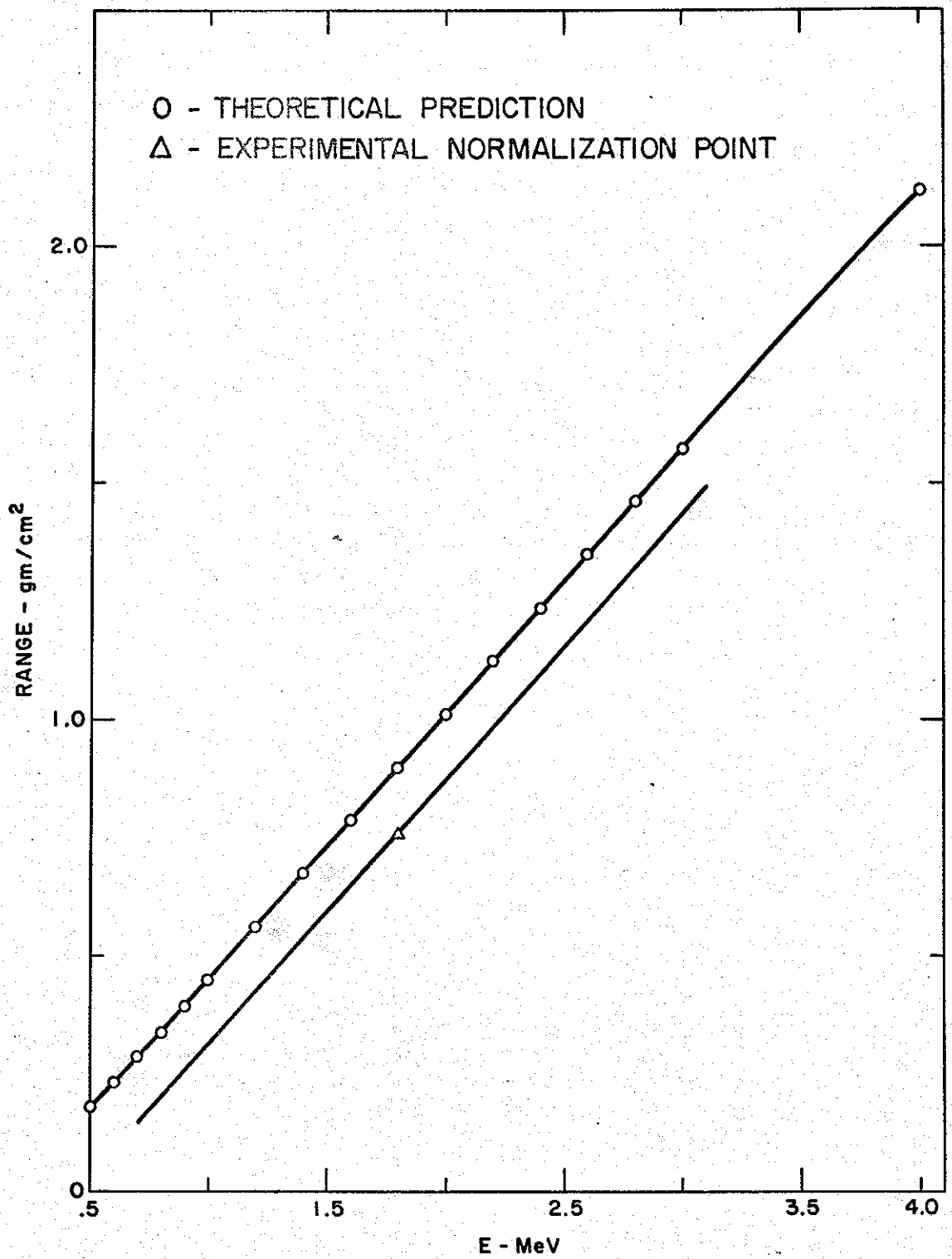
Figure 2.12.   Range vs. energy for electron penetration
              in lucite - theoretical and experimental

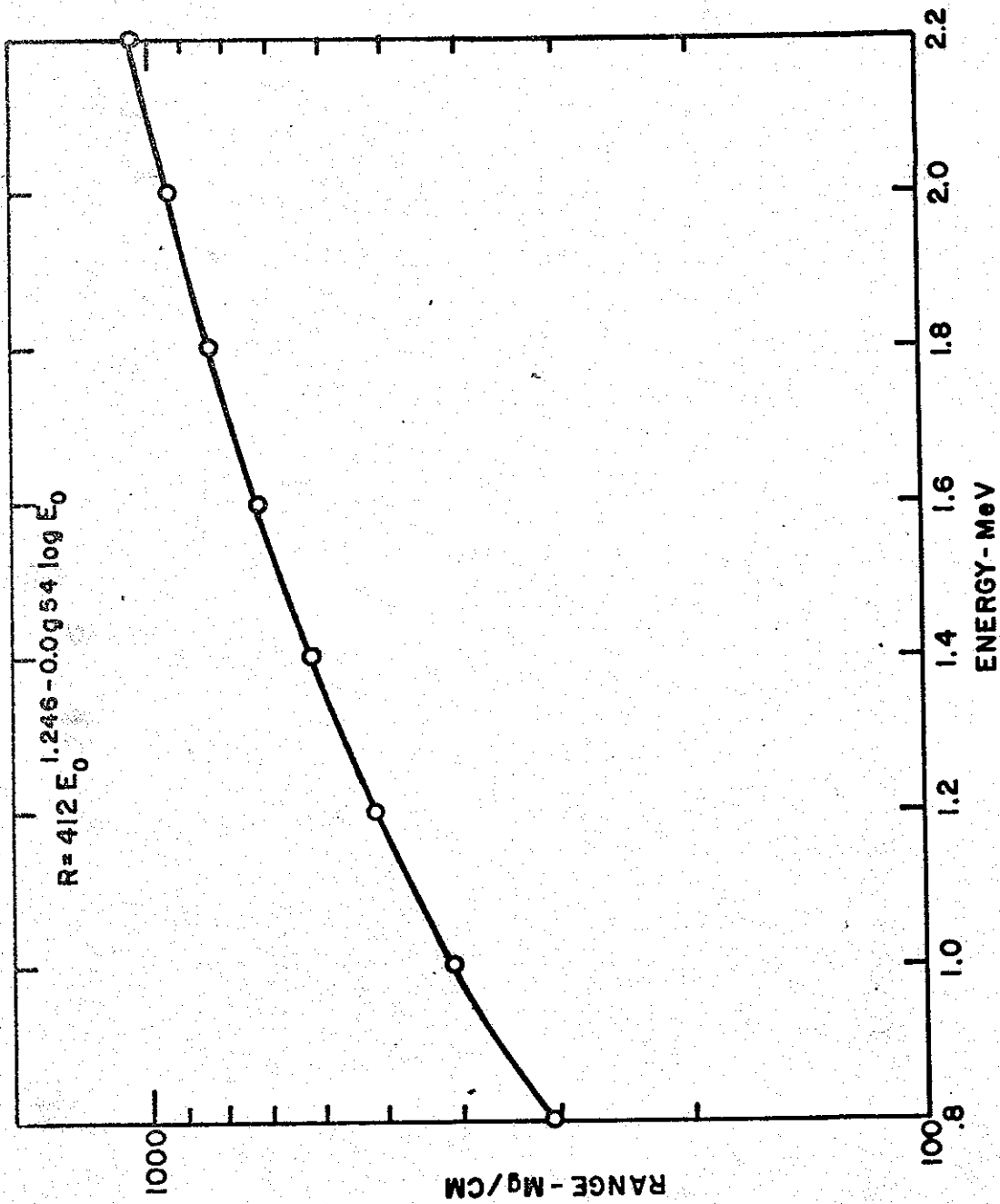which defines the effective monoenergetic energy, E_{eff}, and where E is the electron energy, dE(E)/dx is the electron stopping power at energy E, and J(o,E) is the surface energy dissipation function for normally incident electrons defined by Spencer.[20] In this reference calculated values are available for aluminum and polystyrene and in this report the polystyrene predictions are used in the analysis of the Cinemoid results. Typical results for the Sandia Model 705 Febetron No. 1 using this technique are presented in Section III.C.

It should be evident from the information presented in Section II.C that the electron beam is monoenergetic if the maximum energy and effective energy are found to be identical.

It can also be shown (see Appendix A) that over a limited energy range (i.e., typical of the Febetron 705 electron energies) the effective energy of an electron beam possessing a spectrum of electron energies is less than the average energy of the electrons in the beam.

Beam Average Energy

Combining the results of the current measurements with those obtained from the energy density measurements described in Section II.A, it is possible, in principle at least, to determine the average electron energy at any position where both quantities are measured. The average energy, $\overline{E}$, determined in this way is then given by

$$\overline{E} = I_B \bigg/ \frac{Q}{qA} \tag{2.13}$$

where $q = 1.6 \times 10^{-19}$ coulomb and A is the aperture area. Due to the fact that the energy density and current measurements are representative of only a small portion of the electron beam, the average energy determined from Equation 2.13 is itself not characteristic of the beam as a whole.

Current and Voltage Waveforms

The electron differential energy spectrum representative of the entire beam can, in principle, be determined directly from the current time history (as obtained from a Faraday cup which collects the entire charge released by the electron tube) and the time dependence of the cathode-to-anode voltage, i.e., at a given instant in time the cathode-

to-anode voltage determines the electron energy and the current at that same time determines the number of electrons possessing this energy. In practice this requires an accurate knowledge of the tube shank inductance, as can be seen from Equation 2.10, but this is not always easily determined, with the result that this technique does not generally yield high accuracy results.

Magnetic Spectrometer

As mentioned in the introduction, the complex trajectories of the electrons emerging from the tube window make representative high resolution energy spectrum measurements difficult. In order to measure the electron energy spectrum for a single pulse (this is desirable to eliminate any effects which might result from poor pulse reproducibility or tube deterioration), it is desirable to use a broad range spectrometer to cover as large an energy range in a single pulse as possible. At this Laboratory measurements of the electron differential energy spectrum have been made with a focussing-type spectrometer, similar to that described by Browne and Buechner.[24]

In order to attain relatively high resolution, the electron beam (total charge release per pulse of approximately a couple of hundred microcoulombs) was collimated, allowing only a small fraction of the electron beam charge to enter the magnetic field region. (As indicated previously, this means the spectrometer measurements are not representative of the entire beam.)

The configuration of the electron spectrometer is shown in Figure 2.13a and 2.13b. In this design both source and image are external to the field region.* The magnetic field is produced by a 4-inch pole piece Varian Model V-4001 electromagnet. When this spectrometer is used on the Sandia Model 705 Febetron, the electromagnet is far removed from the tube window due to the fact that the focussing coil in this machine produces a magnetic field external to the tube window, which results in an undesirable perturbation upon the internal spectrometer field. The separation is,

---

*For a given field setting the length of the focal plane of the spectrometer corresponds to radii of curvature for the electrons from 0.85 R to 1.51 R where R is the radius of the pole pieces.

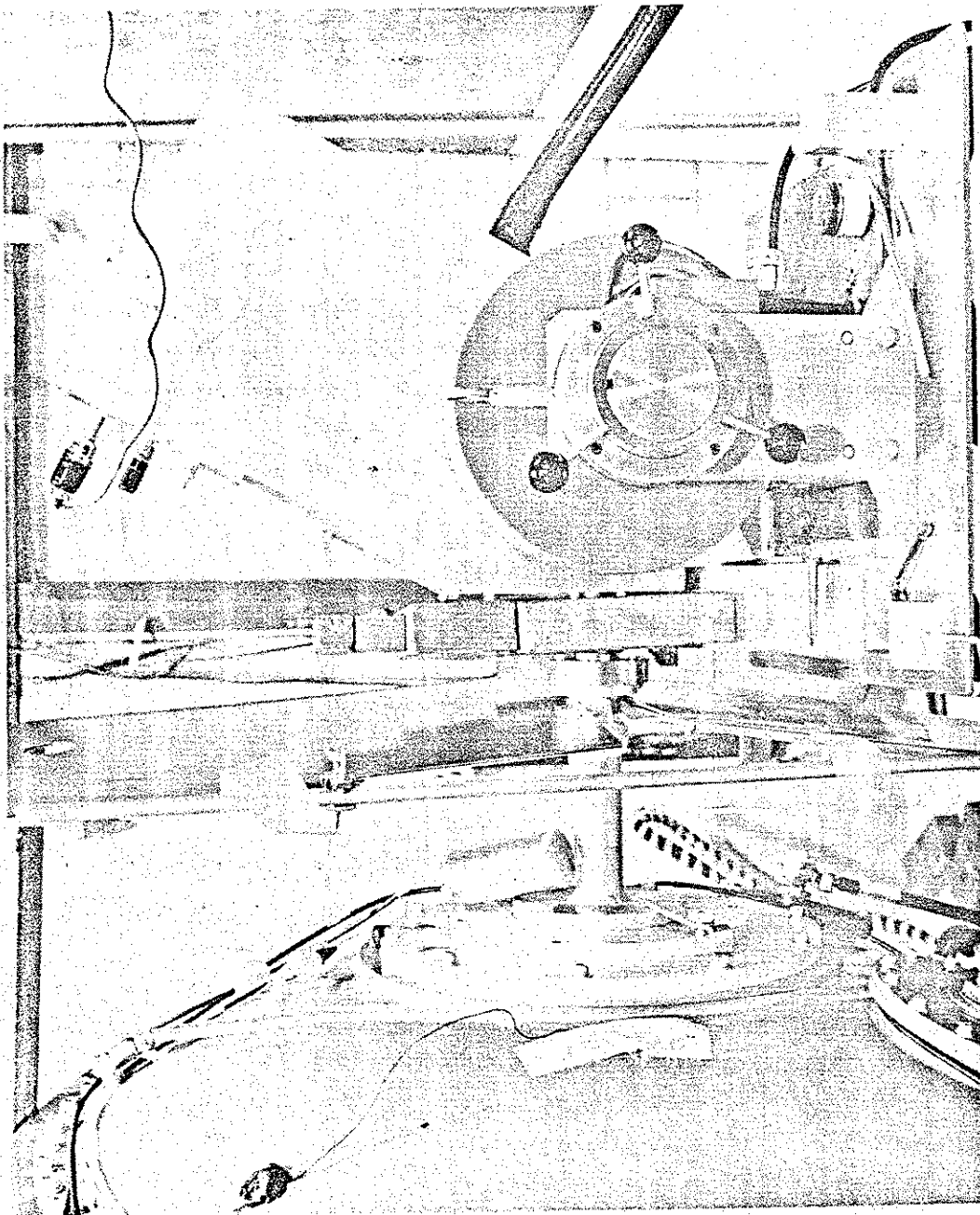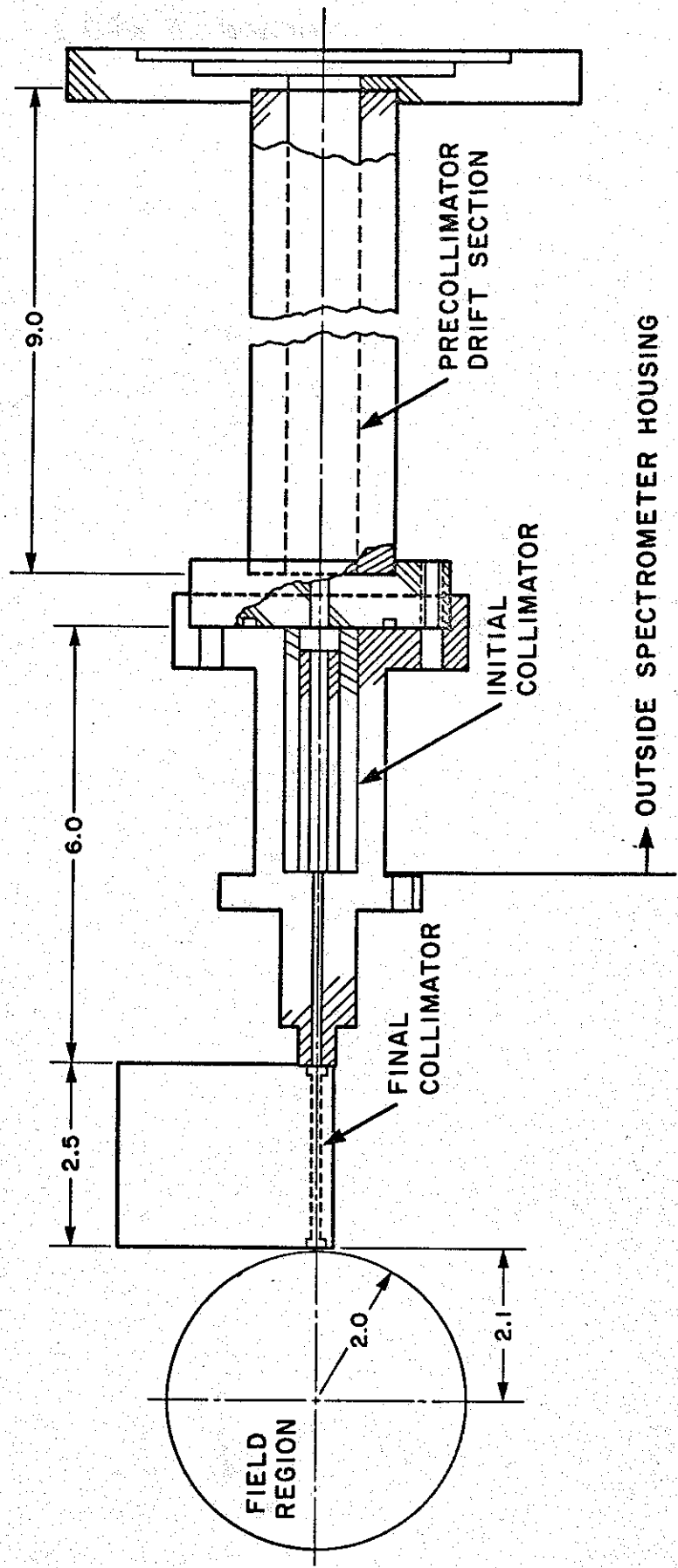Figure 2.13a. Magnetic spectrometer; photograph of assembly

Figure 2.13b. Magnetic spectrometer; cross-sectional view

PRECOLLIMATOR DRIFT SECTION

INITIAL COLLIMATOR

FINAL COLLIMATOR

OUTSIDE SPECTROMETER HOUSING

FIELD REGION

9.0

6.0

2.5

2.0

2.1

however, not large enough to make the electron beam appear as if it resulted from a point source. The fact that the Browne and Buechner design is for focussing electrons originating from a point source at a finite distance from the field boundary is of no serious consequence in these measurements, since the incident beam is so highly collimated that acceptable energy resolution can be achieved with energy separation alone and no focussing.

Eastman Kodak type KK and AA films were employed as the electron detector at the focal plane of the spectrometer. The film was densitometrically analyzed to determine film optical density as a function of position along the focal plane. These results were then corrected for the width of the signal trace by making transverse densitometer measurements. The position along the focal plane is converted to electron energy using the theoretical expression of Browne and Buechner. Due to the fact that these films should have the same response to electrons as Eastman Kodak No Screen,[25] for which calibration data is available,[26] the energy dependent sensitivity of this film (determined for normal incidence of the electrons only) is used to obtain the electron exposure corresponding to a given optical density. As can be seen in Figure 2.13a, lead was used to shield the film from the bremsstrahlung produced in the collimator.

Energy calibration of the spectrometer was accomplished using a radioactive P^{32} β-source and a Li-drift Si detector with the pole piece gap set at one-eighth inch. The Si detector was positioned at the center of the focal plane and the electron energy measured as a function of magnetic field strength. The field measurements were made with a RFL Model 1965 Hall effect gaussmeter. As mentioned above, the electron energy corresponding to the position of the Si detector was theoretically calculated for a given field strength and was found to agree with the measured values to within five percent, i.e., the measured energy being higher than that predicted. This difference has been attributed to the existence of a fringe field. Additional evidence for the presence of a fringe field comes from measurements made with larger pole piece separations where it has been found that the deviation between experiment and prediction increases with increasing pole piece separation.

D. Space Charge Effects

Space charge buildup and polarization effects in dielectric materials, sometimes used to monitor electron beams, have been reported by a number

of experimenters.[1,2,3,4] The supposition is that electrons penetrating the dielectric material, subsequent to being stopped, are trapped in the dielectric with an associated charge buildup in that region. The field resulting from this space charge should repel electrons arriving at later times with the result that the energy deposition in the material should possess a different spatial variation and/or should be less than if space charge effects were absent, as is the case in a metal, for example.

The results presented in Figure 2.9 and Table II.1 indicate that these effects have not been observed in our work with #25 Cinemoid, at least within experimental error. The estimated errors for each type of material were presented earlier. However, these results were obtained with laminates of Cinemoid and are therefore probably not representative of solid dielectrics. One possible explanation for this lack of observable space charge effects is that air ionization and/or surface conduction on the thin samples of dosimetry material result in a path to ground for the stopped electrons, at least for those exposures carried out in air. In order to test this hypothesis, a set of runs were performed in which stacks of #25 Cinemoid were exposed in vacuum (approximately 100 μ pressure) and air where, in each case, both grounded and ungrounded configurations were employed. The resulting dose-depth curves are shown in Figure 2.14 and the beam energy density for all the shots is to be found in Table II.2. The results for all four combinations agree within experimental error so that any space charge effects, if present, can be no more than about 10 percent for the Cinemoid layered samples.

Table II.2

Beam Energy Density Measurements
in Vacuum and Air with Laminated
Cinemoid Stacks Both Grounded
and Ungrounded

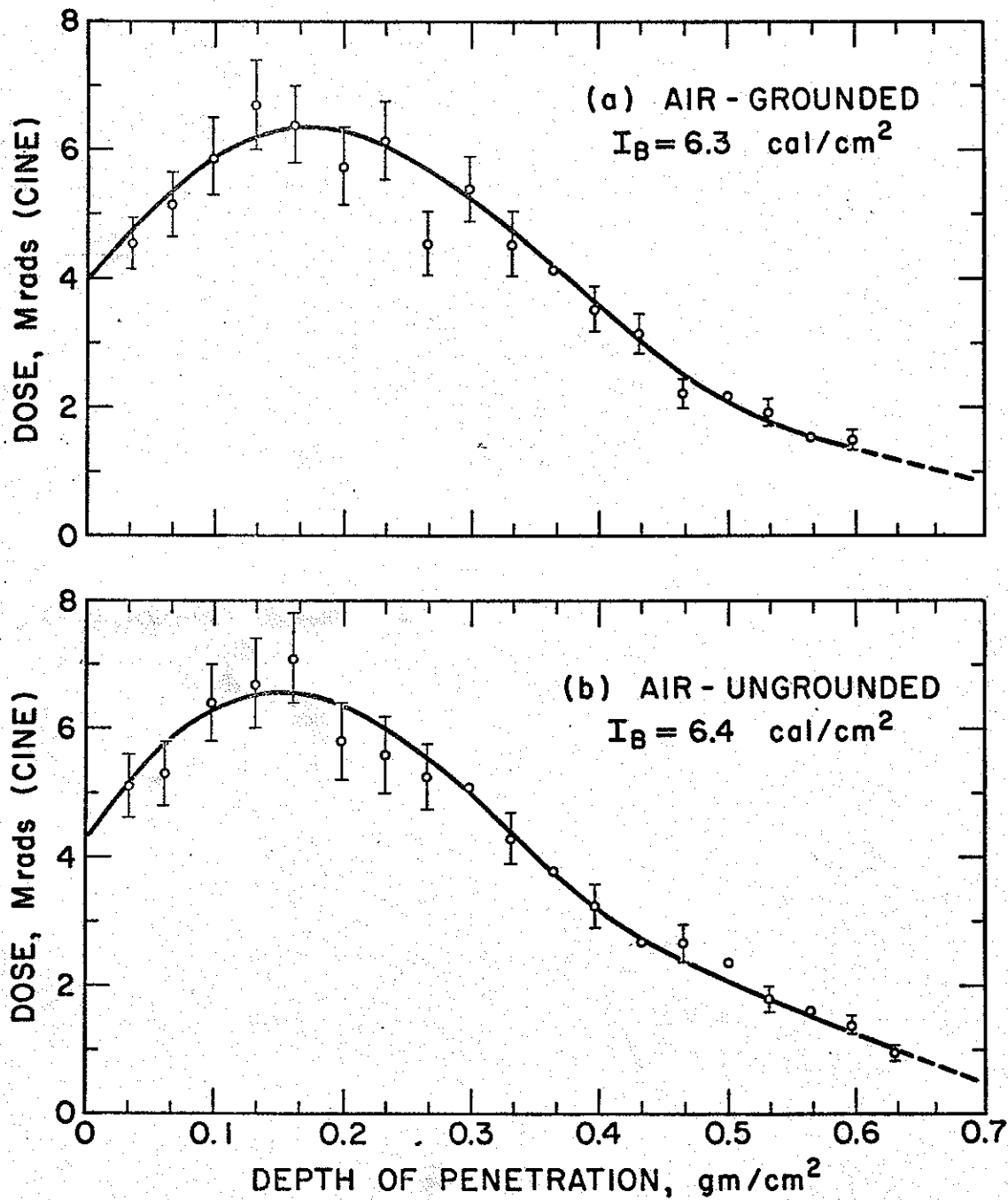|	Beam Energy Density (cal/cm^2)			
	Air		Vacuum	
Shot No.	Grounded	Ungrounded	Grounded	Ungrounded
1	6.3	5.4	5.6	4.9
2	5.6	5.9	6.7	6.4
3	5.5	6.4	5.4	5.7
Av.	5.8	5.9	5.9	5.7

Figure 2.14a,b.   Electron energy deposition vs. penetration in #25 Cinemoid -
air and vacuum environments, grounded, and ungrounded
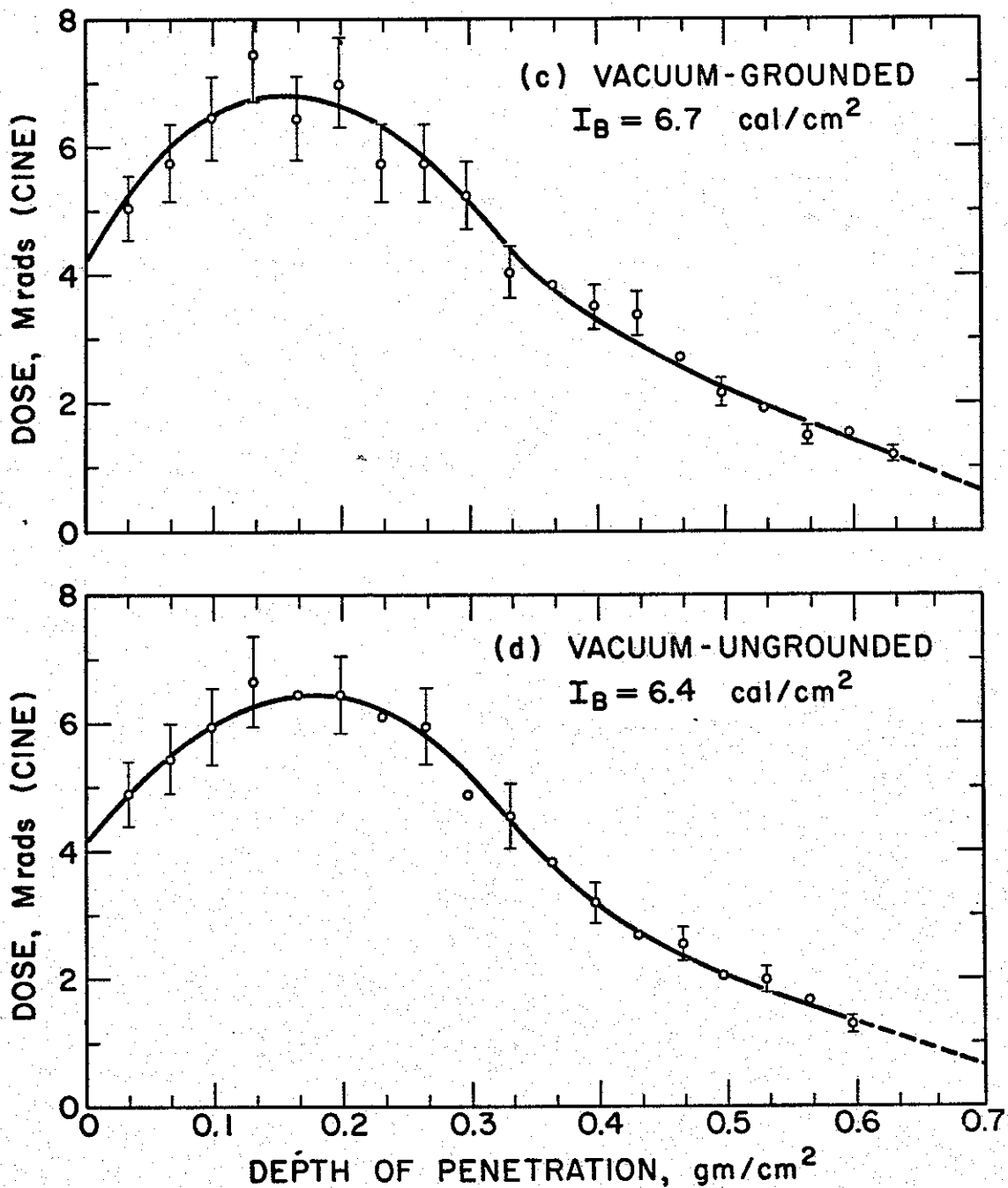configurations

Figure 2.14c,d. Electron energy deposition vs. penetration in #25 Cinemoid - air and vacuum environments, grounded, and ungrounded configurations

Previous work by Rauch and Andrew[1] indicated that space charge effects
are important in lucite for samples thicker than that of the Cinemoid discs
employed in this work. A set of measurements were carried out in an attempt
to reproduce the results of Rauch and Andrew which were also obtained using
a Model 705 Febetron operated in the electron beam mode. In these measure-
ments one looks for changes in the dose-depth curve by placing stacks of
#25 Cinemoid behind varying thicknesses of lucite. The results of these
experiments are shown by the deposition profiles presented in Figure 2.15.
It is seen from this figure that the dose-depth curves at large depths of
penetration are the same within experimental error for all the lucite
samples (except the 1/16" sample for which the results are consistently low
at all depths of penetration, but higher than the results presented in
Reference 1, which may have resulted from a low output for this particular
shot) even though, in all cases except the 1/64" sample, the lucite samples
underwent charge breakdown with resultant Lichtenburg figures. For small
depths of penetration the results for the 1/64" and 1/16" lucite samples
fall below those for the stack of #25 Cinemoid alone; while, for the 1/32"
lucite sample, an anomalous increase in dose is observed. The former effect
is consistent with a picture in which the higher energy electrons, being
incident upon the sample at early times before space charge effects are
important, determine the end of the energy deposition curve. At a later
time in the pulse, when the space charge has had time to accumulate, the
lower energy electrons (which are incident at this time) may be repelled
with a resulting decrease in the energy deposition at small depths of
penetration. The anomalous increase in dose for the 1/32" lucite sample
cannot be explained at this time. The deviations between the various dose-
depth curves are of the order of the experimental error (2σ precision error)
so that if the phenomenon postulated above is indeed present, its effect
upon the energy deposition process must be of the order of 20 to 25 per-
cent. Rauch and Andrew observed larger deviations and this may result
from the difference in beam charge density employed in the two sets of
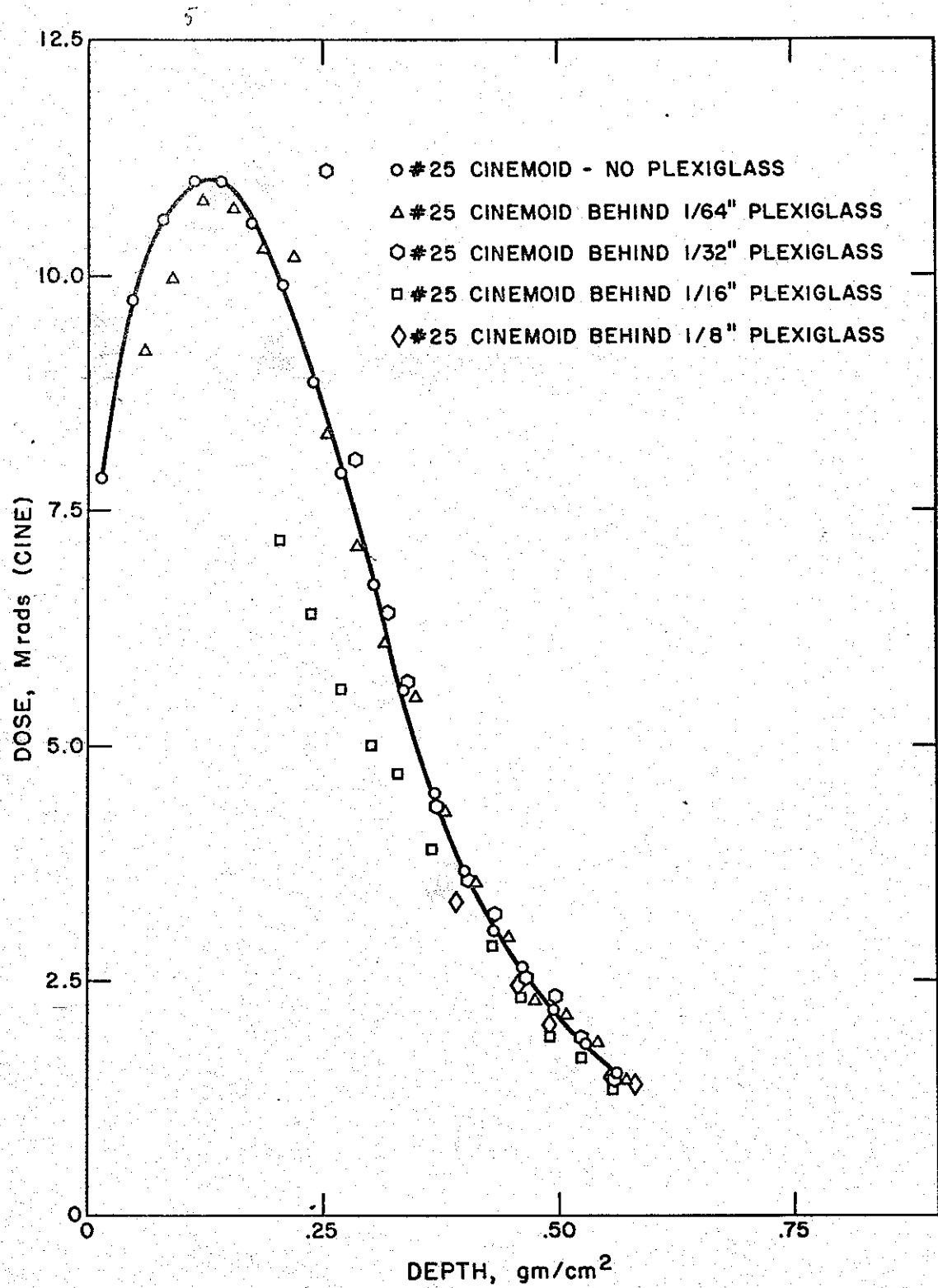measurements.

Figure 2.15. Electron energy deposition in lucite and #25 Cinemoid vs. penetration for the Sandia Model 705 Febetron

III. EXPERIMENTAL RESULTS

A. Beam Current

It is not possible, at this time, to present absolute results for the beam current or charge release measurements due to the fact that under typical measuring conditions the internal shunt resistance of the Faraday cup was found to be of the order of magnitude of the current viewing resistor (i.e., $50 \, \Omega$). Additional current viewing resistors in the range of 0.025 to 1.0 Ω will be employed in future measurements.

In spite of this problem it is possible to present some interesting and useful results at this time. It has been found that the completeness of the electron return path to the machine has a marked effect upon beam current measurements. The results presented in Table III.1 show that an adequate return path to the machine must be provided if the proper current is to be measured. In addition, as a result of the relatively long life of the ionized state of the residual gas in the cup (i.e., compared to the duration of the beam-current pulse), the measured current pulse shape should be

Table III.1

Charge Measured With 1/32" Faraday Cup Aperture
at the 9" Position on the Beam Axis for the
Sandia Model 705 Febetron (Type 545A Tube No.
313) as a Function of the Degree of Grounding.

Number of Grounding Straps	Measured Charge (Coulomb)
1	4.2×10^{-8}
2	6.5×10^{-8}
3	8.3×10^{-8}
4	9.1×10^{-8}
5	8.2×10^{-8}
8	8.3×10^{-8}
8	9.0×10^{-8}

representative of the actual beam current time history although the magnitude will be in error as mentioned above.

Figure 3.1 presents results comparing the current time history for the type 545A tube in air and vacuum environments with that of the type 545D tube operated in air. All these results show the current persisting to times in excess of 100 nsec. The 1/16" and 1/32" Faraday cup apertures employed to obtain these results, as well as those presented in Figures 3.2 and 3.3, are therefore representative of but a small portion of the beam. In Figure 3.2 the current time history is shown at a number of positions along the beam axis. The pulse shape is seen to be similar at 0.5 inches and 9 inches; while at intermediate positions the pulse shape appears to be composed of two distinct components where the fast component (the peak occurring at the earliest time in the pulse) is dominant at the 3 inch position, the slow component (the peak occurring at later time in the pulse) is dominant at the 7 inch position, and the two components are comparable in magnitude at the 5 inch position.

In Figure 3.3 results are presented for the current time history as a function of focussing field at (a) the 1 inch position and (b) the 3.5-inch position on the beam axis. These results indicate that as the focussing field is decreased from 3000 g to 2400 g, the slow component disappears, and upon further reduction in the field to 1800 g the shoulder existing at long times for the 2400 g field is eliminated. It is possible that this latter current contribution corresponds to a separate energy group of electrons.

Due to the fact that absolute current measurements were not achieved, it was not possible to determine the average energy. Even if accurate current measurements had been possible, average energy measurements would not have been accurate since the energy density measurements are not representative of the same fraction of the beam as the current measurements (as mentioned earlier the energy density measurements are representative of a larger fraction of the beam than the 1/32" and 1/16" apertures employed in the current measurements). This is evident from the beam profiles to be found in Figures 3.6 and 3.7.

"A" TUBE 200μ PRESSURE

"A" TUBE AMBIENT AIR
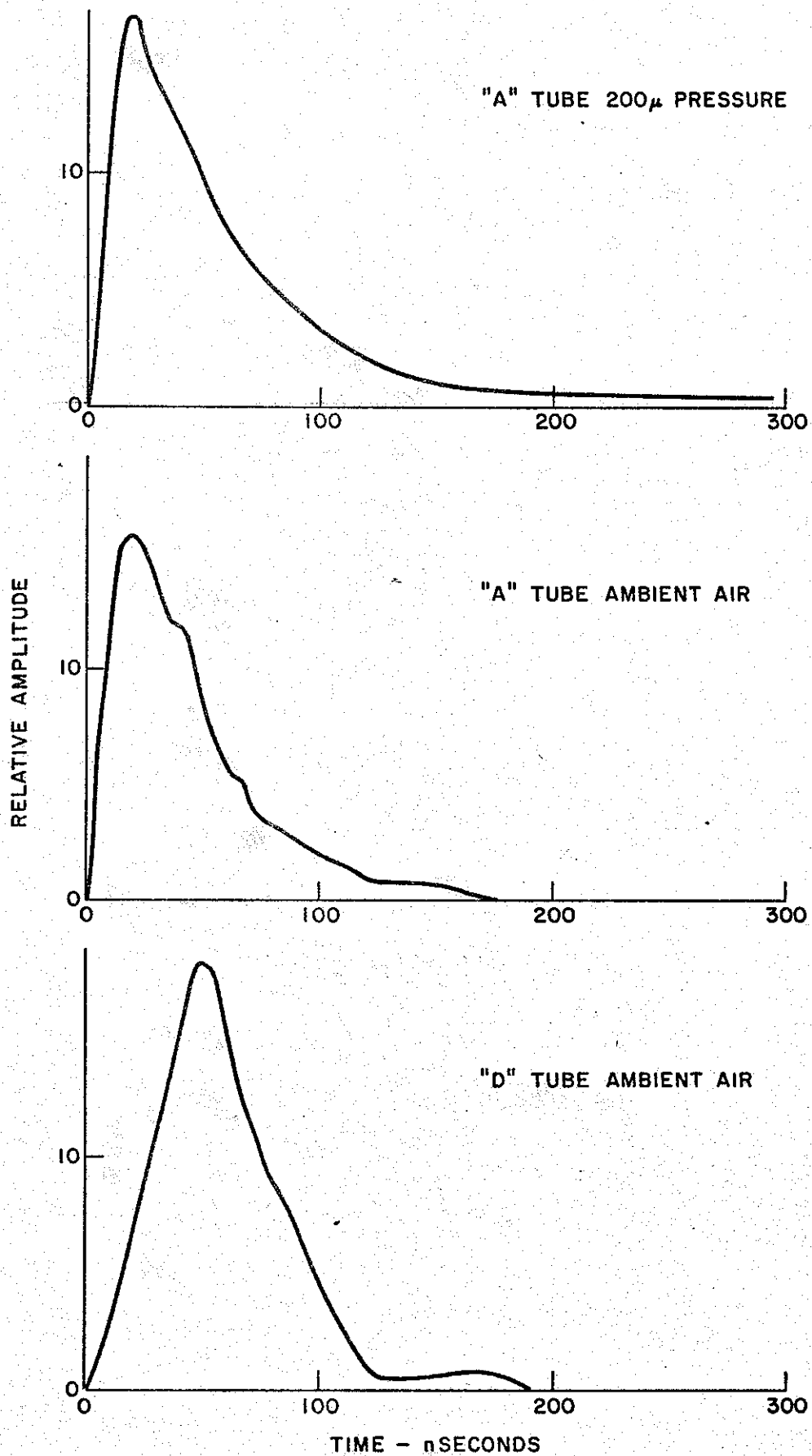
"D" TUBE AMBIENT AIR

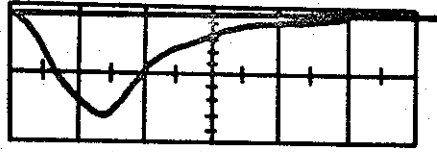RELATIVE AMPLITUDE

TIME — nSECONDS

Figure 3.1. Electron current time history for A- and
D-type tubes - air and vacuum environments

0.5 in.,
1/16" APERATURE,
940 V/CM
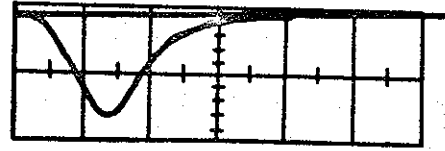
1.5 in.,
1/32" APERATURE,
188 V/CM
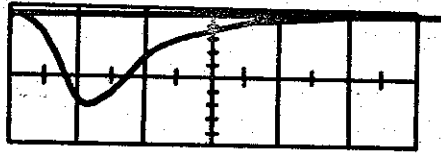
3",
1/16" APERATURE,
470 V/CM
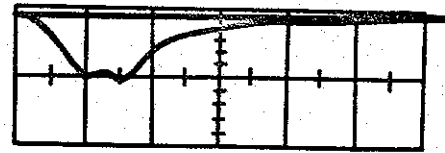
5",
1/16" APERATURE,
470 V/CM
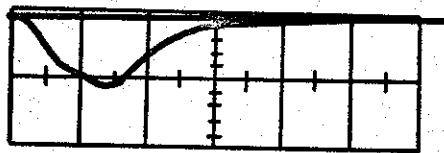
7",
1/16" APERATURE,
470 V/CM
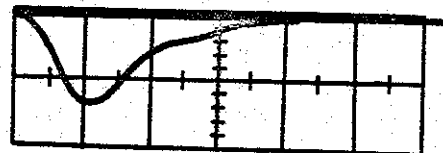
9",
1/16" APERATURE,
470 V/CM

Figure 3.2.   Sandia Model 705 Febetron current waveforms as a
function of distance from the tube surface for
Type A tube No. 313 in air. The sweep speed is
20 nsec/cm in all cases
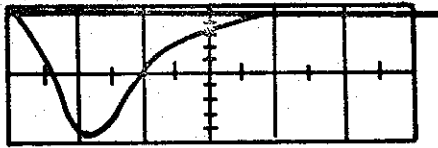
3000 gauss
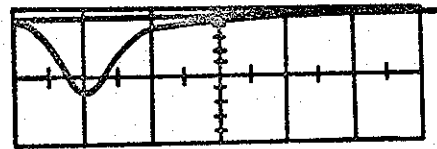
1800 gauss
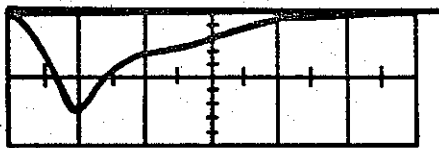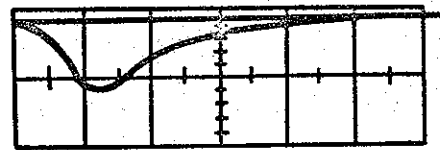
2400 gauss

3000 gauss
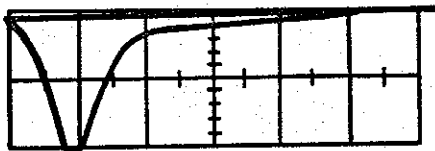
1800 gauss
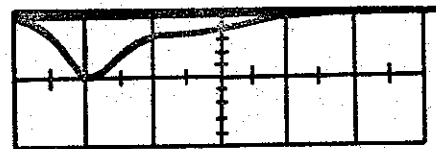
2400 gauss

Figure 3.3a. Sandia Model 705 Febetron current waveforms vs. focussing field for Type A tube No. 313 in air at the 1" position (1/32" aperture, 188 V/cm, 20 nsec/cm)

Figure 3.3b. Sandia Model 705 Febetron current waveforms vs. focussing field for Type A tube No. 313 in air at the 3.5" position (1/16" aperture, 470 V/cm, 20 nsec/cm)

B. Absorbed Dose

Spatial variations in the absorbed dose, as a function of distance from the tube surface, along the axial centerline of the electron tube were measured with 5 mil aluminum calorimeters and Cinemoid. These measurements were made in air and vacuum environments for both the Type A and D tubes.

In Figure 3.4 are presented the results for a "D" type tube obtained with a minimum absorption aluminum calorimeter and #25 Purple Cinemoid. The measurements depicted by the open circles and triangles (Figure 3.4) were made alternately with the calorimeter and Cinemoid. The pressure maintained in the drift tube during these measurements was approximately 50 μ. The data represented by the solid circles were the result of the minimum absorption aluminum calorimeter measurements at ambient pressure in the drift tube. As may be noted, the self-pinching of the electron beam at ambient conditions is quite evident.

Figure 3.5 depicts similar results obtained on several different "A" tubes. The upper curve (open circles) is the result of measurements obtained in a vacuum environment ($\approx 50 \mu$) with the minimum absorption aluminum calorimeters, and the lower most curve (triangles) is the result with #25 Cinemoid again at a pressure of approximately 50 μ. Intermediate to these two curves are minimum absorption calorimeter measurements (squares) obtained at ambient pressure. The data in this figure are not normalized and differences in magnitude of absorbed dose are the result of differences in output of the several tubes.

In addition to spatial variation measurements along the axial centerline, absorbed dose measurements normal to this coordinate were obtained by placing Cinemoid sheets normal to the electron beam at several distances from the tube surface. Additionally, arrays of silver phosphate and cobalt glass were arranged, again, normal to the electron tube axial centerline for additional beam profile data.

In Figures 3.6(a) and 3.6(b) are plotted the results, absorbed dose to Cinemoid, as a function of distance from the tube axial centerline.
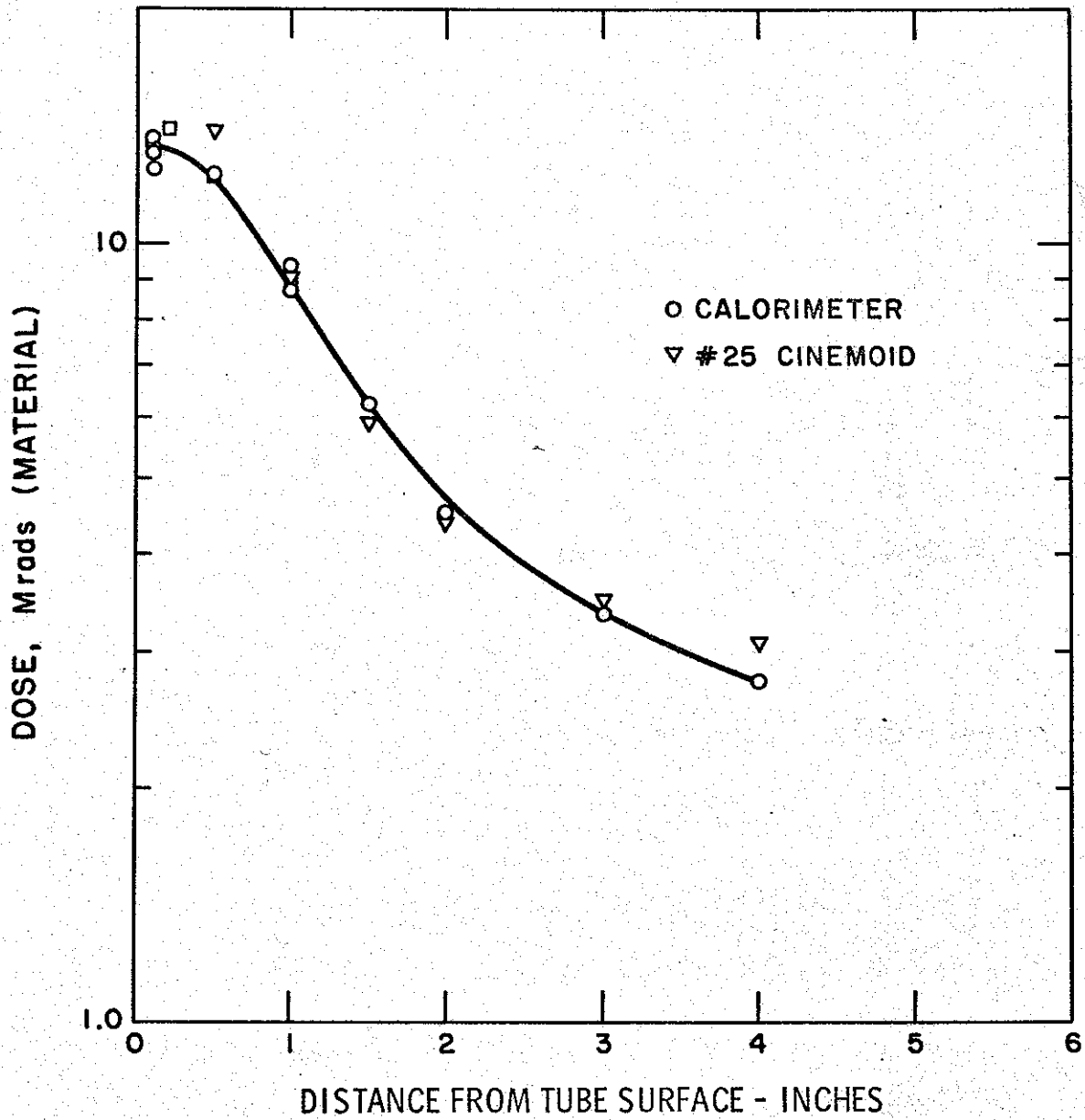
Figure 3.4a. Electron dose in aluminum and Cinemoid vs. distance for a D-type tube at partial vacuum
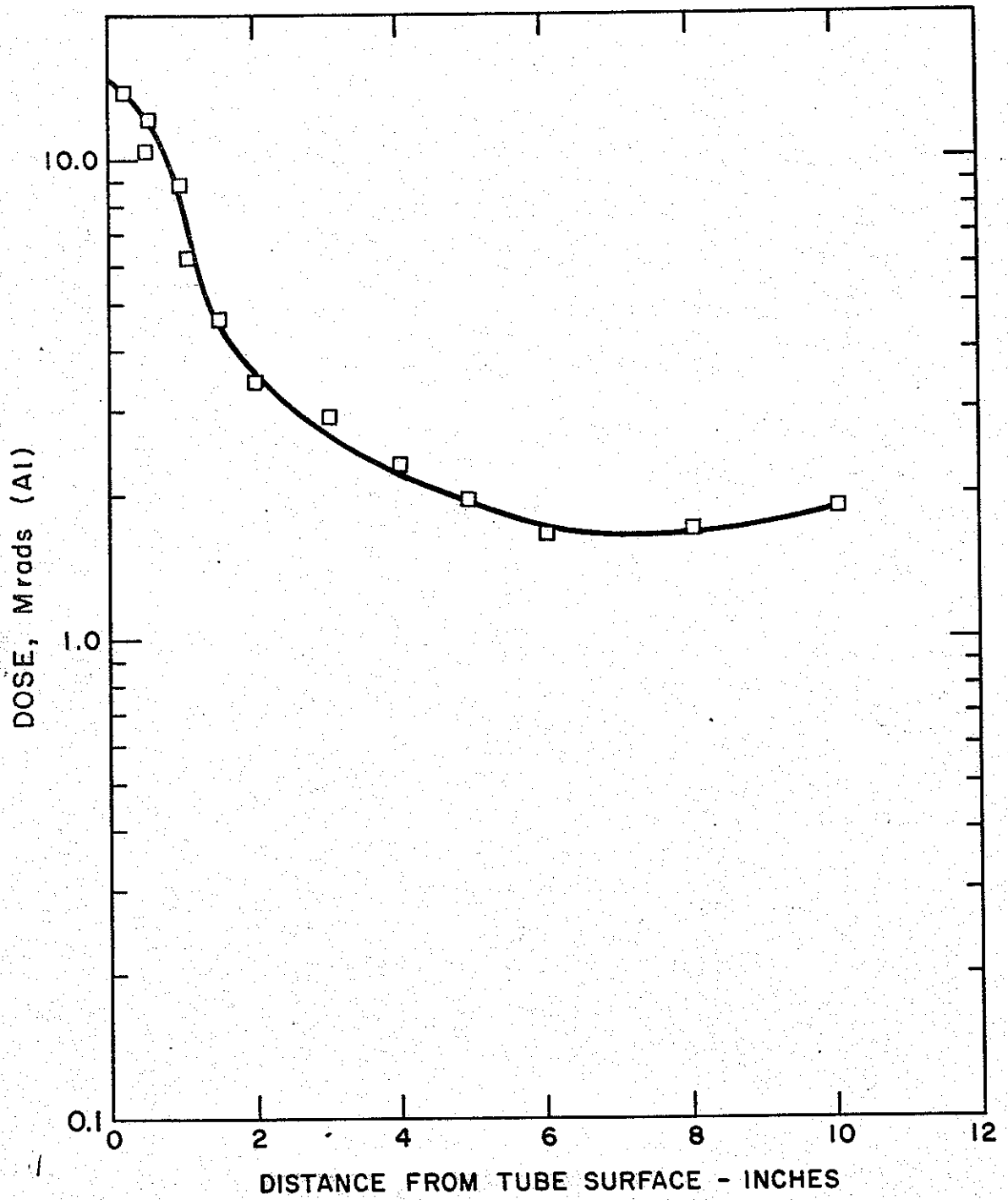
Figure 3.4b. Electron dose in aluminum vs. distance
for a D-type tube atmospheric pressure
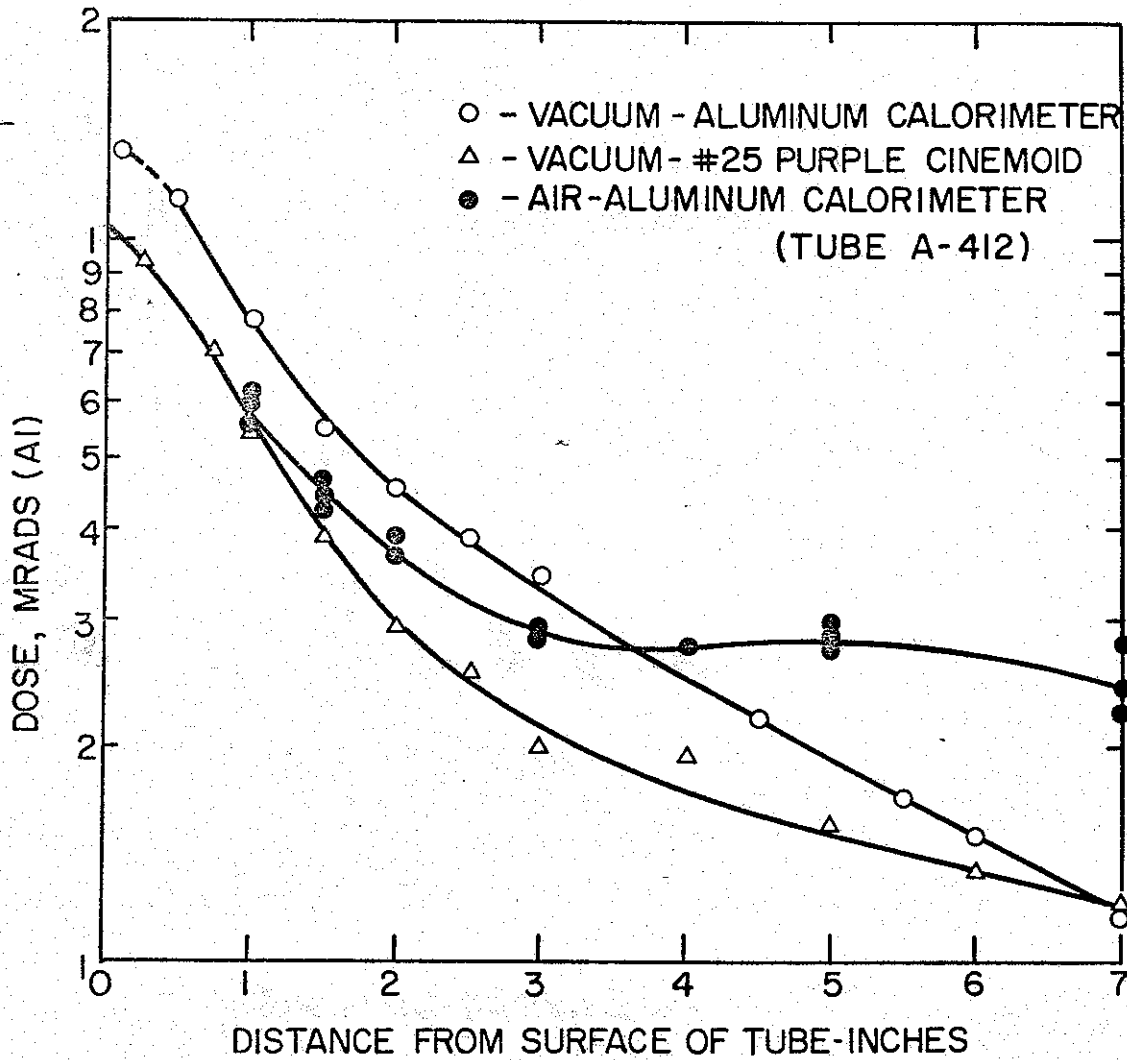
Figure 3.5. Electron dose in aluminum and Cinemoid vs distance for
an A-type tube at vacuum, and atmospheric pressure

Figure 3.6a.   Spatial variation of the electron dose to Cinemoid vs. distance from the axial centerline at various distances from the tube surface (Type A tube) at a pressure of 50 μ

Figure 3.6b. Spatial variation of the electron dose to Cinemoid
vs. distance from the axial centerline at various
distances from the tube surface (Type A tube) at
a pressure of 50 μ

These results are for an "A" tube firing into the drift tube maintained at 50 μ pressure and for distances spanning the interval from 8.5 inches to the tube surface. These data appear as continuous or smooth curves since the Cinemoid film was scanned, or analyzed, by means of a continuous recording microdensitometer.

Figures 3.7(a) and 3.7(b) present the information obtained with Cinemoid and ambient pressure conditions in the drift tube.

The beam profile information (condensed) obtained from the cobalt and silver phosphate glass measurements is presented in Figure 3.8. These measurements were made at 5 inches from the tube surface at ambient pressure. Since these glasses were analyzed on the Beckman DK-2 Spectrophotometer, the data appear in histogram form.

Note that, owing to the greater sensitivity of the glass, the resulting data extend to a much greater lateral range than the Cinemoid plastic data. Several interesting features of the beam are revealed by these data. First, the beam profile is symmetric about the tube axis and continues symmetric back at least 8.5 inches from the tube surface and very little relative beam spreading is evident from these measurements. The second observation, the marked decrease in total energy deposition by the beam, implies a low energy electron component with highly divergent trajectories.

C. Energy Deposition Profiles

Energy deposition profiles (dose-depth curve measurements) were obtained in the Febetron electron beam using aluminum calorimeters, glasses, and Cinemoid plastic. These measurements were made as a function of variation of several parameters, e.g., air and vacuum environments, variation of magnetic field, spatial variations, etc.

In Figure 3.9 is depicted dose versus depth measurements determined with a minimum absorption aluminum calorimeter on the axial centerline. The dashed curve in Figure 3.9 is the representative output of Tube A-297 at 5 inches distance from the tube surface and in an air environment. The solid curve in this figure is also representative of an "A" tube (number unknown); however, in this instance the measurements were in a vacuum
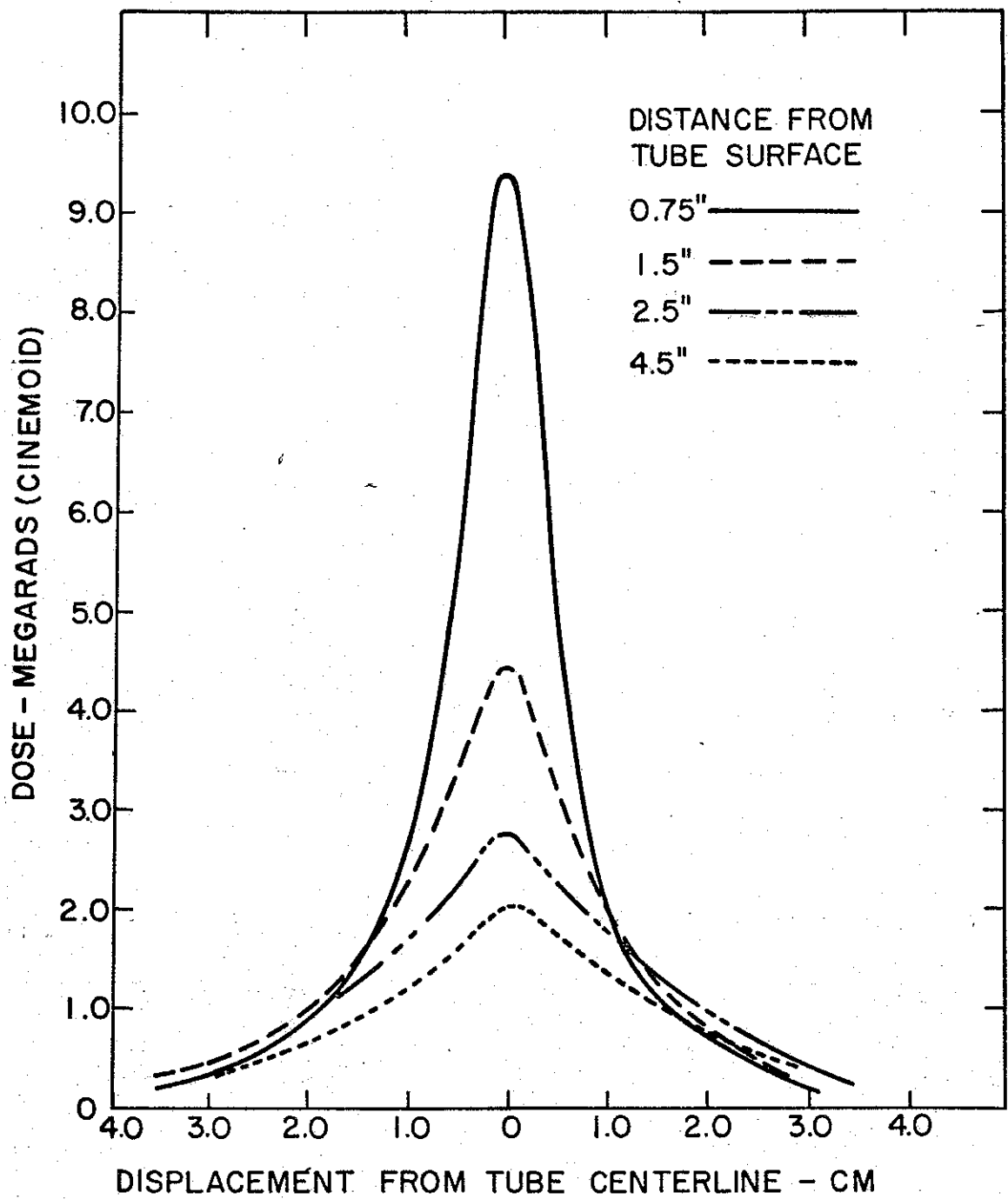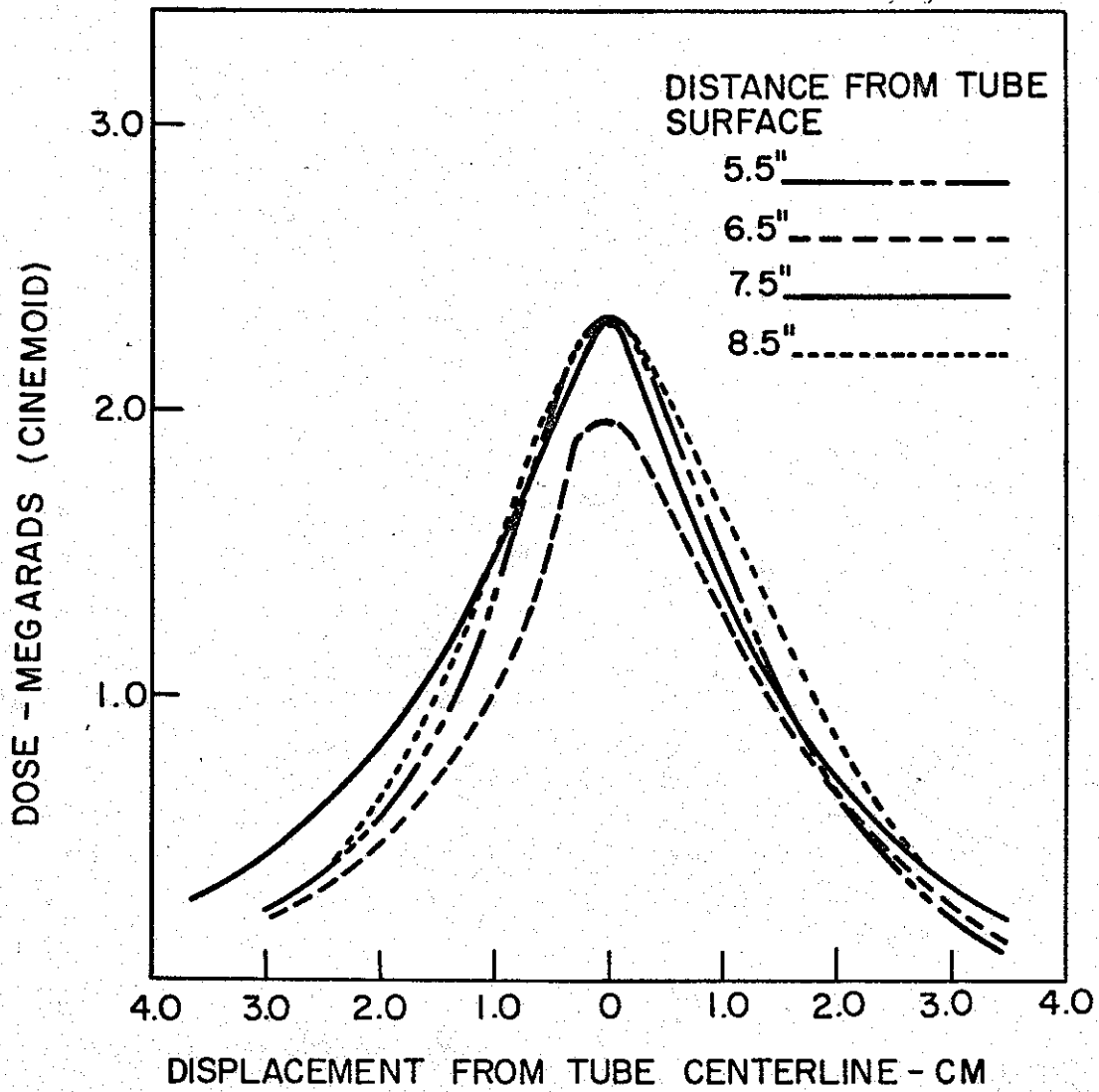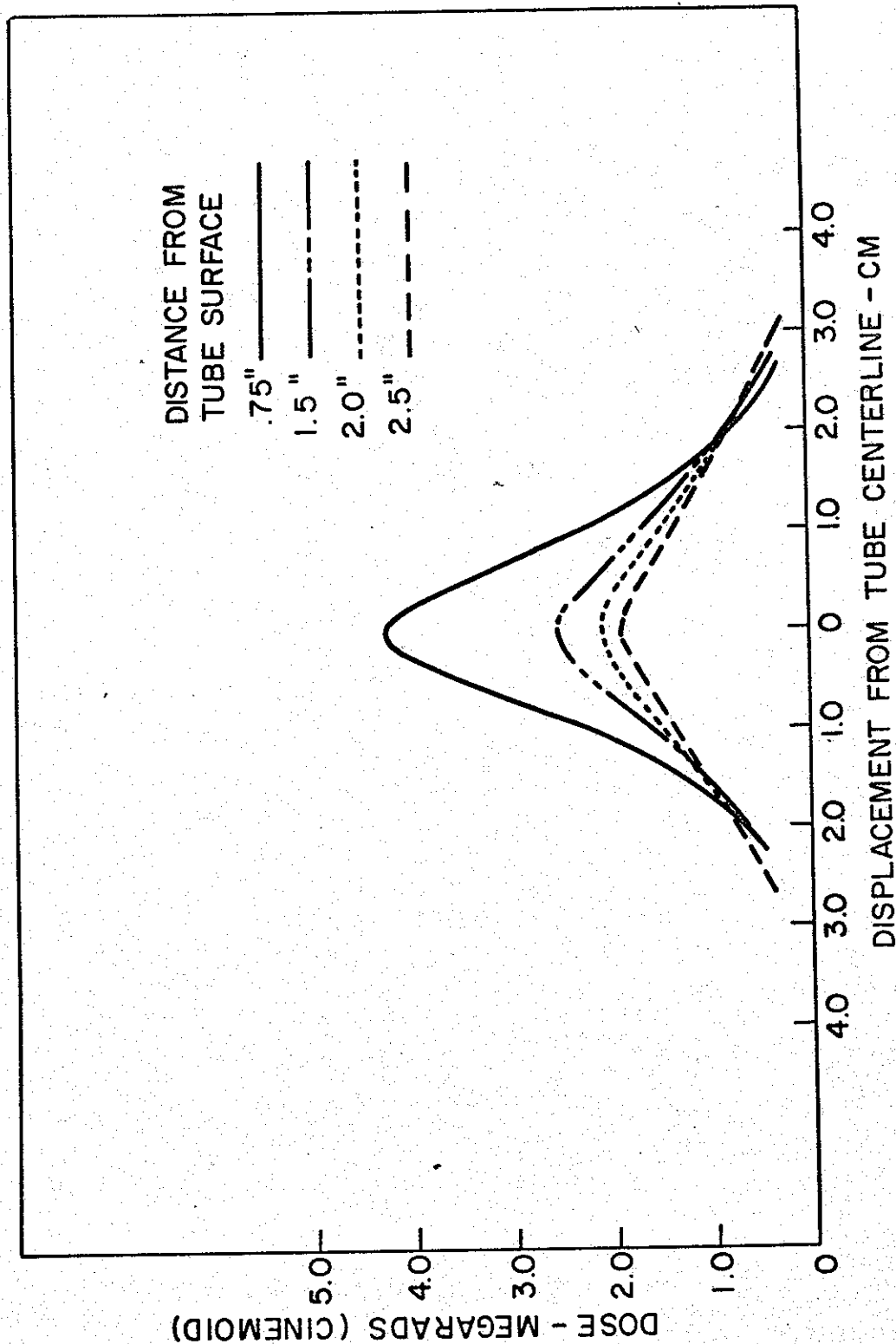
Figure 3.7a. Spatial variation of the electron dose to Cinemoid vs. distance from the axial center at various distances from the tube surface (Type A tube) at atmospheric pressure

Figure 3.7b. Spatial variation of the electron dose to Cinemoid vs. distance from the axial center at various distances from the tube surface (Type A tube) at atmospheric pressure

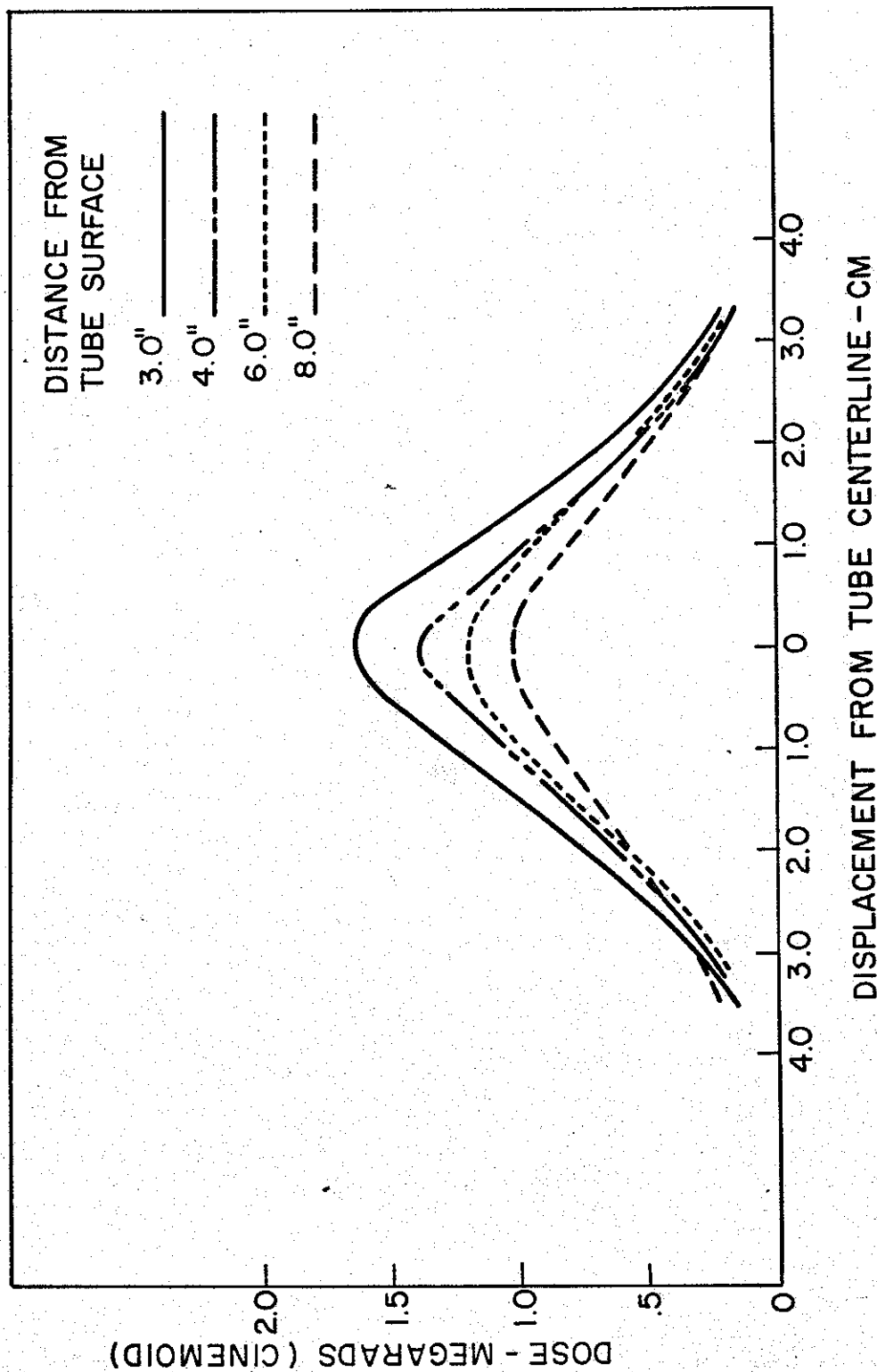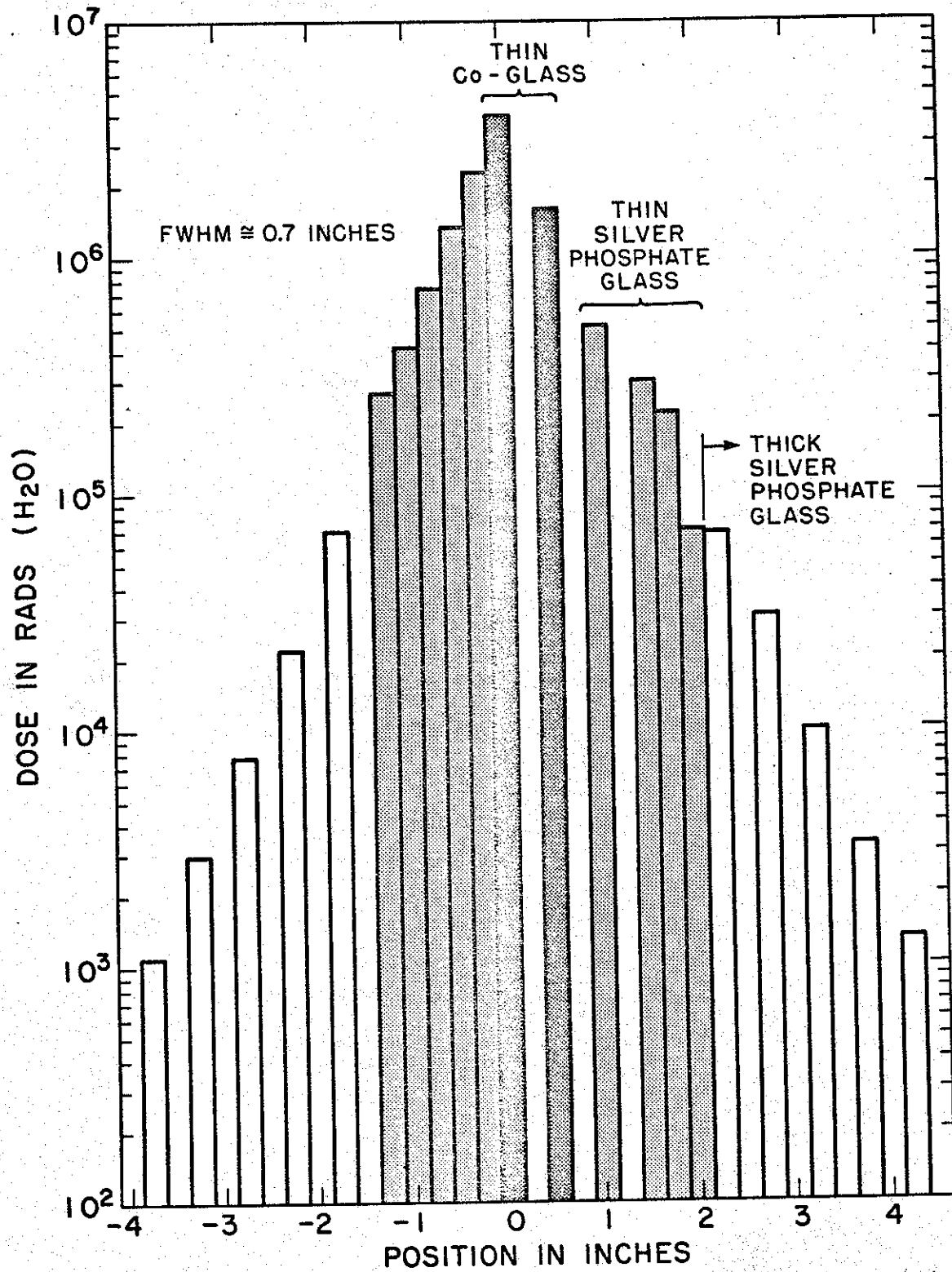Figure 3.8. Spatial variation of the electron dose to cobalt and silver phosphate glass vs. distance from the axial centerline for a Type A tube at atmospheric pressure
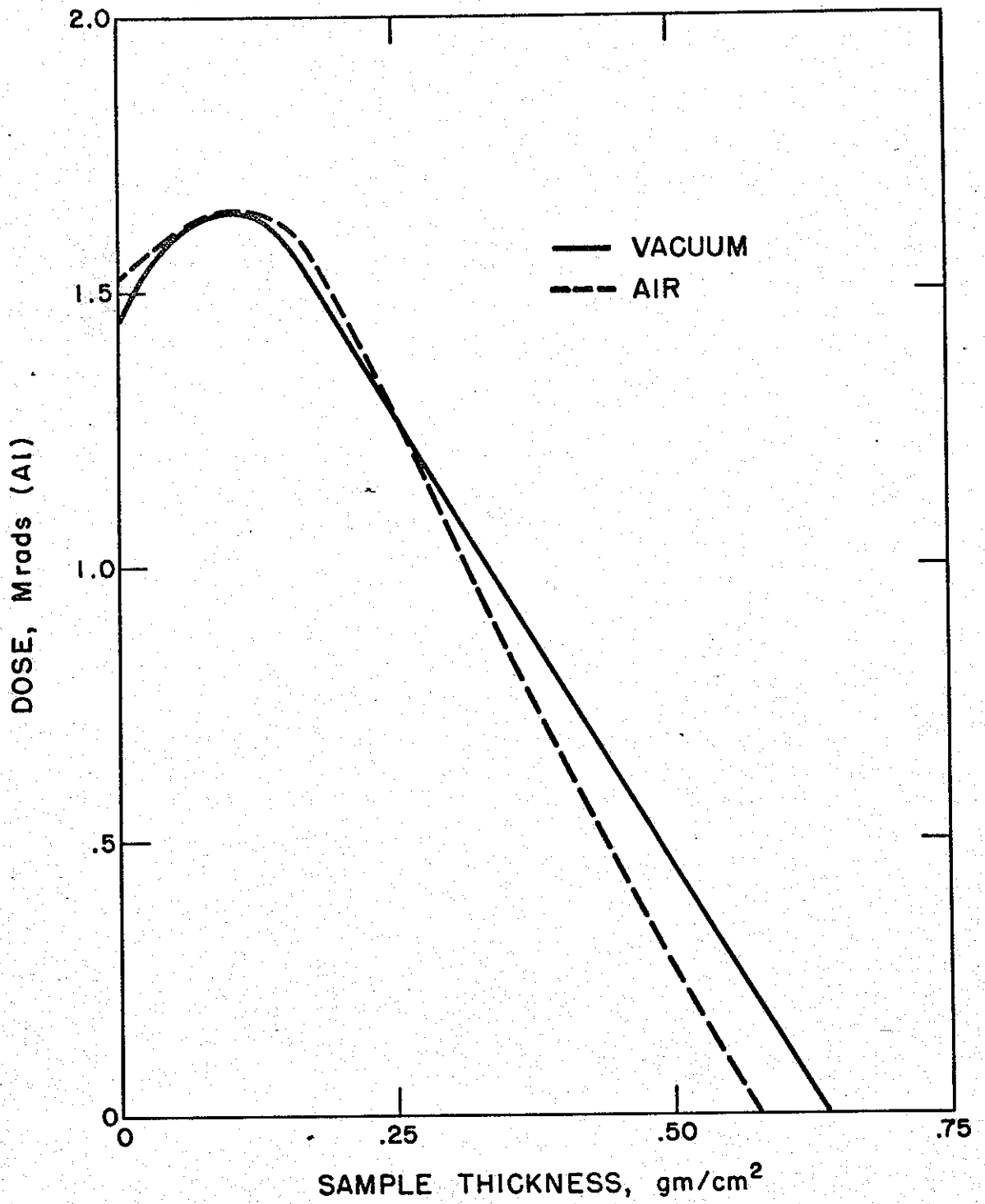
Figure 3.9. Electron energy deposition vs. penetration in aluminum calorimeters -- air and vacuum environments

environment (~ 200 μ). Absorbed dose in megarads is plotted as a function of penetration into the material in gm/cm^2 of material.

Both curves have been extrapolated to zero absorbed dose so that an extrapolated-range energy may be obtained. The extrapolated range of 0.58 gm/cm^2 for tube A-297 yields an extrapolated-range energy of 1.34 MeV, using the experimental range-energy relationship for aluminum (Figure 2.11); whereas, for the other tube, an extrapolated-range electron energy of 1.44 MeV is obtained. Integration of the two curves yields an incident beam energy density of 1.47 cal/cm^2 and 1.4 cal/cm^2 for the dashed curve and solid curve, respectively.

The experimental deposition curve for aluminum from Figure 2.8 is compared to the theoretical deposition curves calculated by Spencer[20] (see Figure 2.6). The deposition curves were calculated for normal incidence of the electrons onto an infinite half-space of aluminum. Presented in the figure are deposition curves, solid lines, for 1.0 and 1.5 MeV electrons. Plotted on the ordinate is the normalized energy deposition, $cal/gm/cal/cm^2$, while the abscissa represents penetration distance into the slab, gm/cm^2. The calculations were based on one electron/cm^2 incident; hence, the area under one of the predicted energy deposition profiles is then the total energy of the incident electron less any fraction of the energy that may have been lost via backscattering and bremsstrahlung.

In order to make a comparison between the measured and calculated deposition curves, some type of normalization of the data is needed; the normalization chosen was to divide the measured data by the incident beam energy density and the calculated results by the energy obtained from the integration mentioned above. As can be seen in Figure 2.6, the measured energy deposition profile is higher at the surface than the prediction for 1-MeV electrons. It peaks at a shallower depth of penetration than for either of the theoretical predictions, and the peak amplitude falls between the peaks for the 1- and 1.5-MeV electrons. The measured deposition profile falls off more rapidly than for the 1.5-MeV case. In this case the extrapolated-range maximum energy (1.35 MeV) appears to be a better choice for a single characteristic electron energy than the effective energy, 0.89 MeV. As stated in Appendix A, the average electron energy which is a better characterization of the beam is greater than the effective energy but less than the extrapolated-range electron energy.

The results from the aluminum calorimeter measurements, in air, on Tube A-297 are compared with some #25 Cinemoid measurements in Figure 2.8. The Cinemoid results are the average of three sets of measurements of the output of Tube A-297, in air, at 5 inches distance from the tube surface. A maximum electron energy, from the extrapolation to zero absorbed energy, is estimated from the results in Figure 2.8 to be 1.36 MeV, while the integrated incident beam energy density is calculated to be 1.40 cal/cm^2.

Although the output of Tube A-297 was found to be about 10 percent low, comparison of the aluminum calorimeter and Cinemoid data is useful. Considering an error of $\pm$ 10 percent for the #25 Cinemoid, the two curves in Figure 2.8 are, therefore, in agreement. This implies that, if space charge effects are present, they affect the energy deposition profile by no more than about 10 percent.

It is observable from the calculated deposition profiles for monoenergetic electrons traversing aluminum presented in Figure 2.6 and the experimentally determined deposition profiles for aluminum and Cinemoid given in Figures 2.8 and 3.9 that the Febetron electron beam is either not monoenergetic or quite disperse (i.e., the electrons possess a substantial range of angles of incidence). It may be seen that the (experimental) curves show an initial energy deposition characteristic of electrons with energies less than 1 MeV, whereas the deposition profile extends to penetrations characteristic of electrons with energies of the order of 1.5 MeV.

In Figure 3.10 are presented dose-depth measurements for #25 Cinemoid as a function of focussing field showing the decrease in dose and therefore beam energy density as well as an apparent lowering of the maximum energy characteristic of the extrapolated-range. The extrapolated-ranges in this figure correspond approximately to energies of 1.39, 1.43, and 1.45 MeV, but this may be primarily the result of spectral changes rather than a change in the end point energy of the electron beam energy spectrum.

Deposition measurements were also made on and off the beam axis at 3.5 inches and 9 inches from the tube window using 15° intervals up to a maximum of 60° with respect to the beam axis. Typical results are shown in Figure 3.11 where it can be seen that the dose-depth curves are characteristic of that expected for a large angular dispersion of the electrons penetrating the stacks of cobalt glass and silver phosphate glass employed.
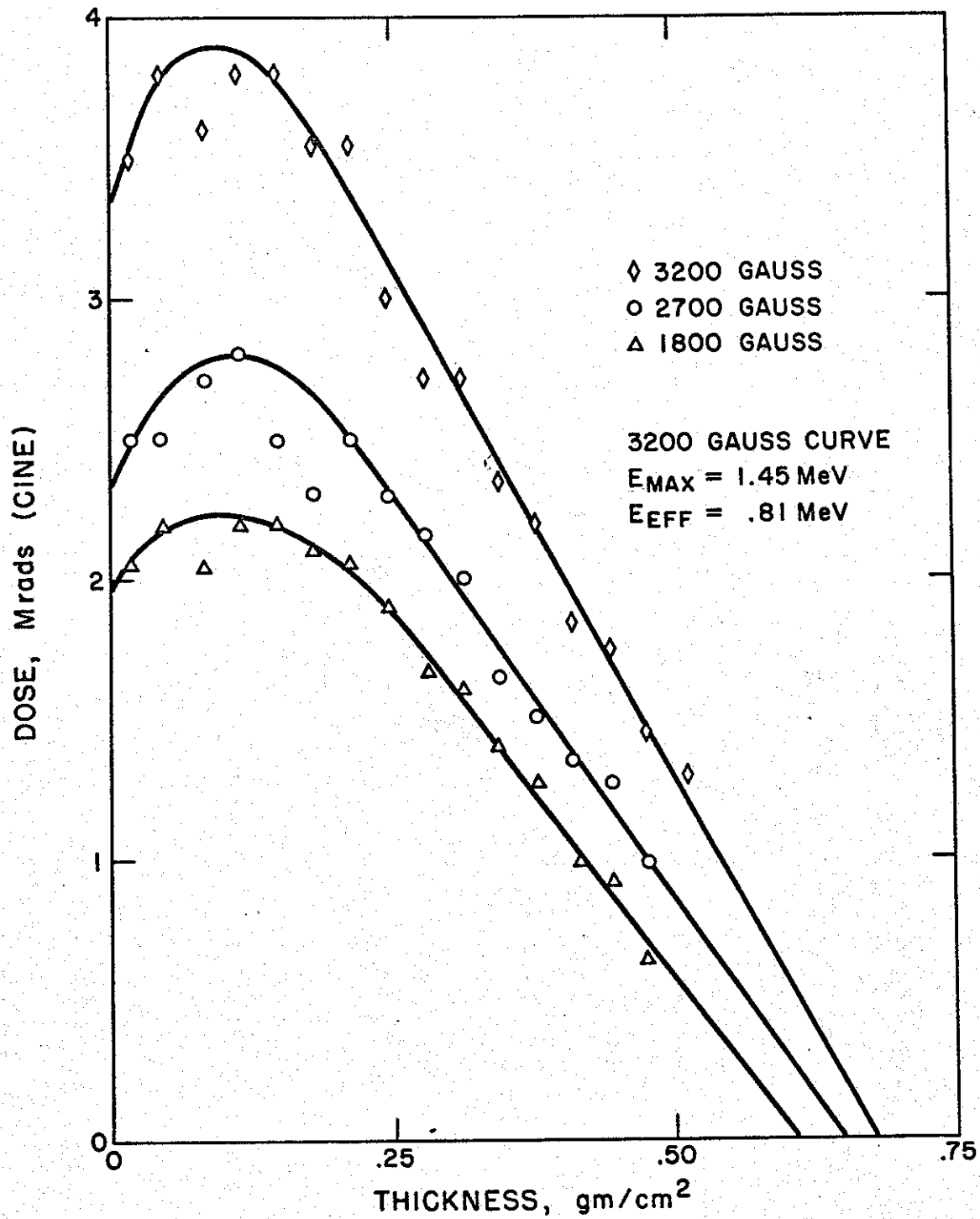
Figure 3.10. Electron energy deposition vs. penetration in
#25 Cinemoid at focussing fields of 3200,
2700, and 1800 gauss

Figure 3.11a. Electron energy deposition vs. penetration in silver phosphate or cobalt glass at the 9", 15° position

Figure 3.11b. Electron energy deposition vs. penetration in silver phosphate or cobalt glass at the 9", 30° position

I_B = 0.42 cal/cm^2

DOSE, Mrads (Co-GLASS)
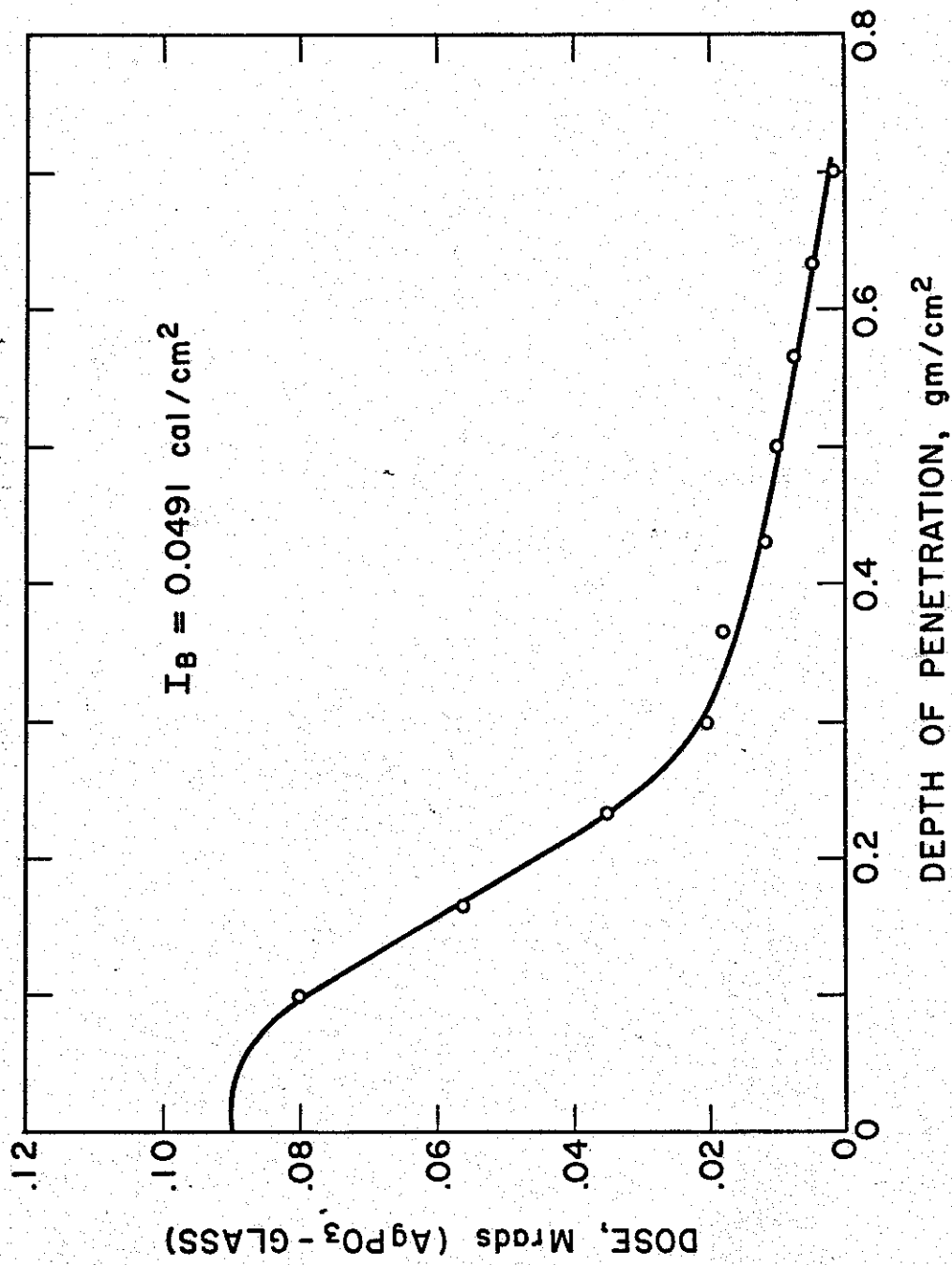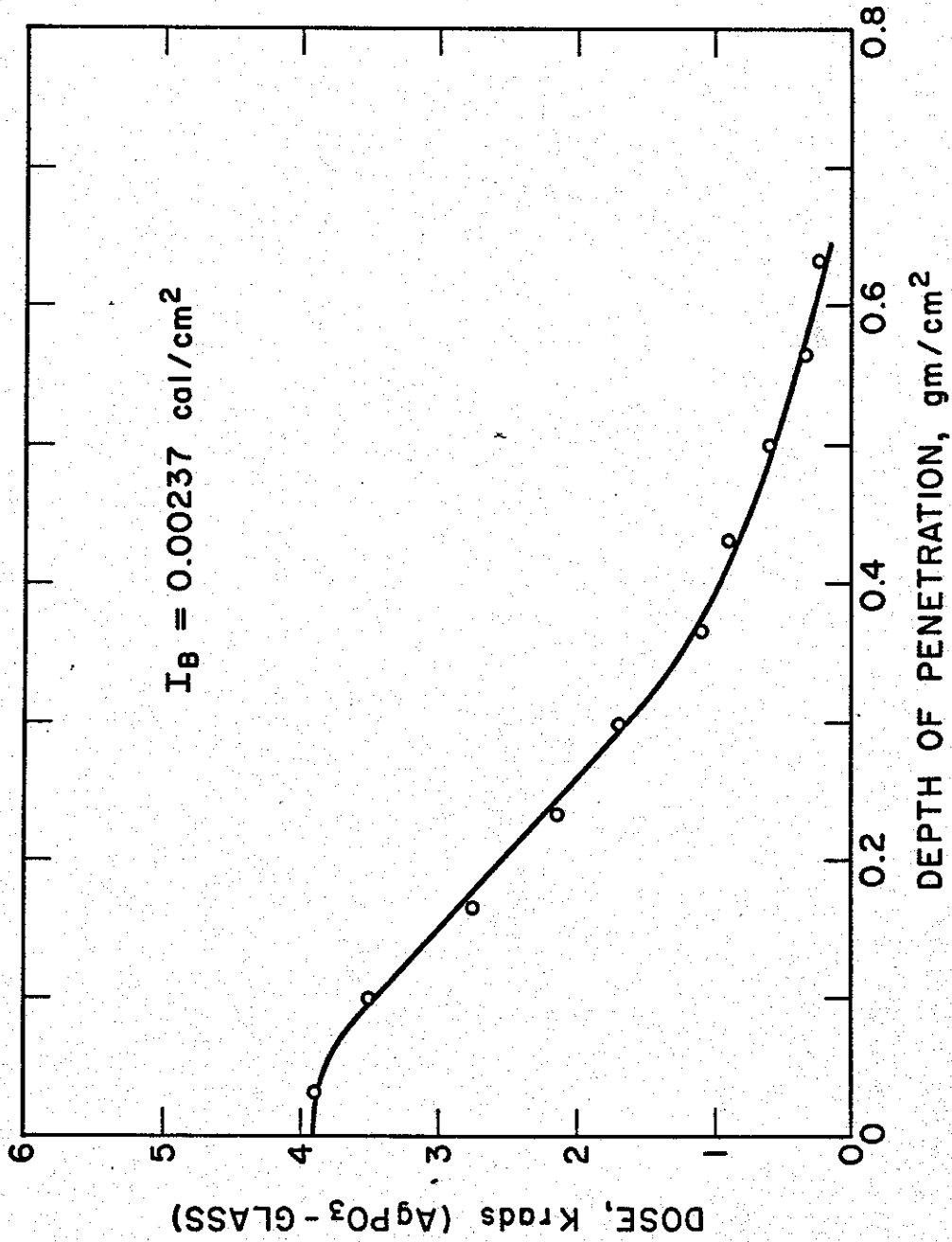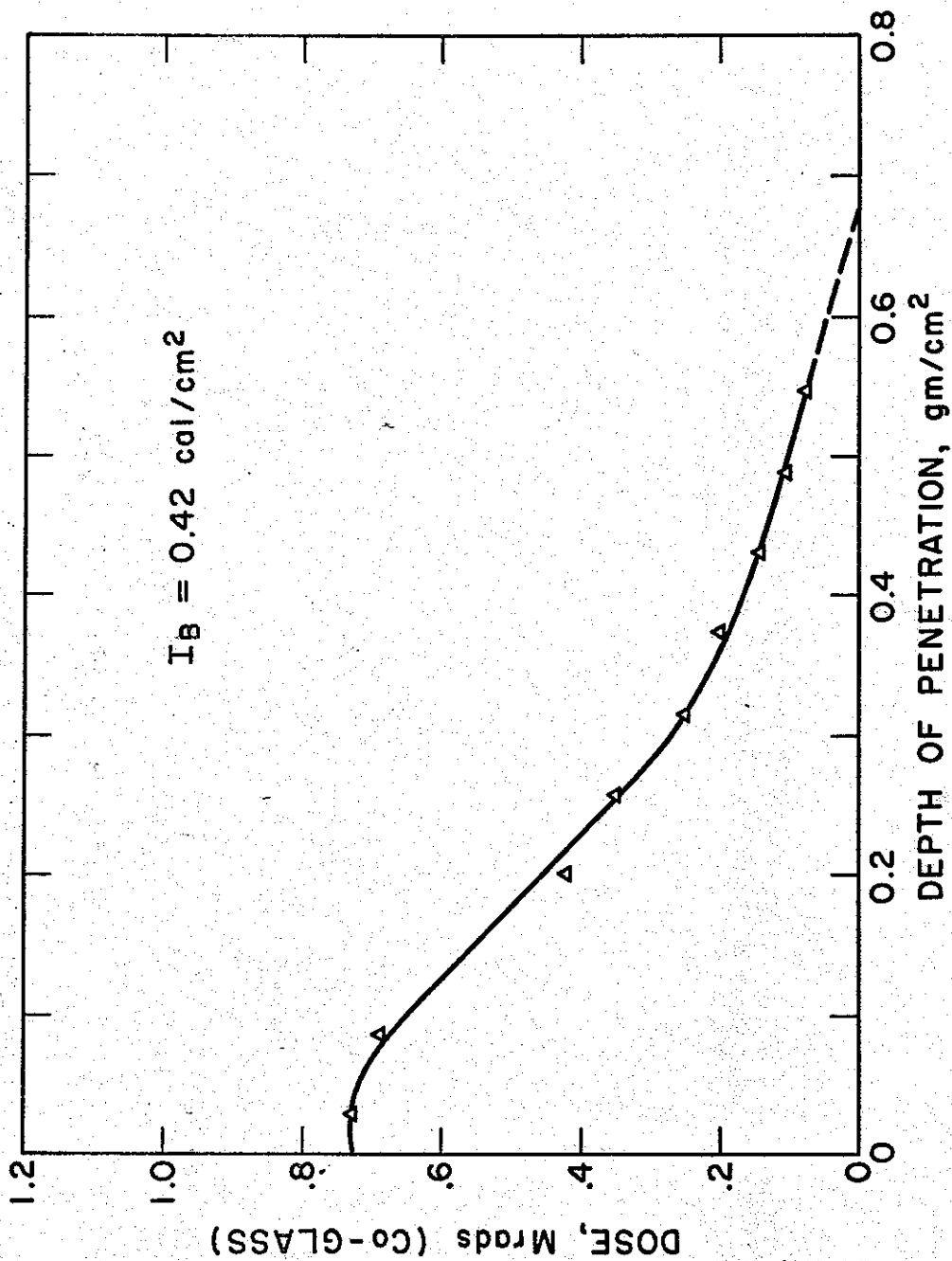
DEPTH OF PENETRATION, gm/cm^2

Figure 3.11c. Electron energy deposition vs. penetration in silver phosphate or cobalt glass at the 3.5", 15° position
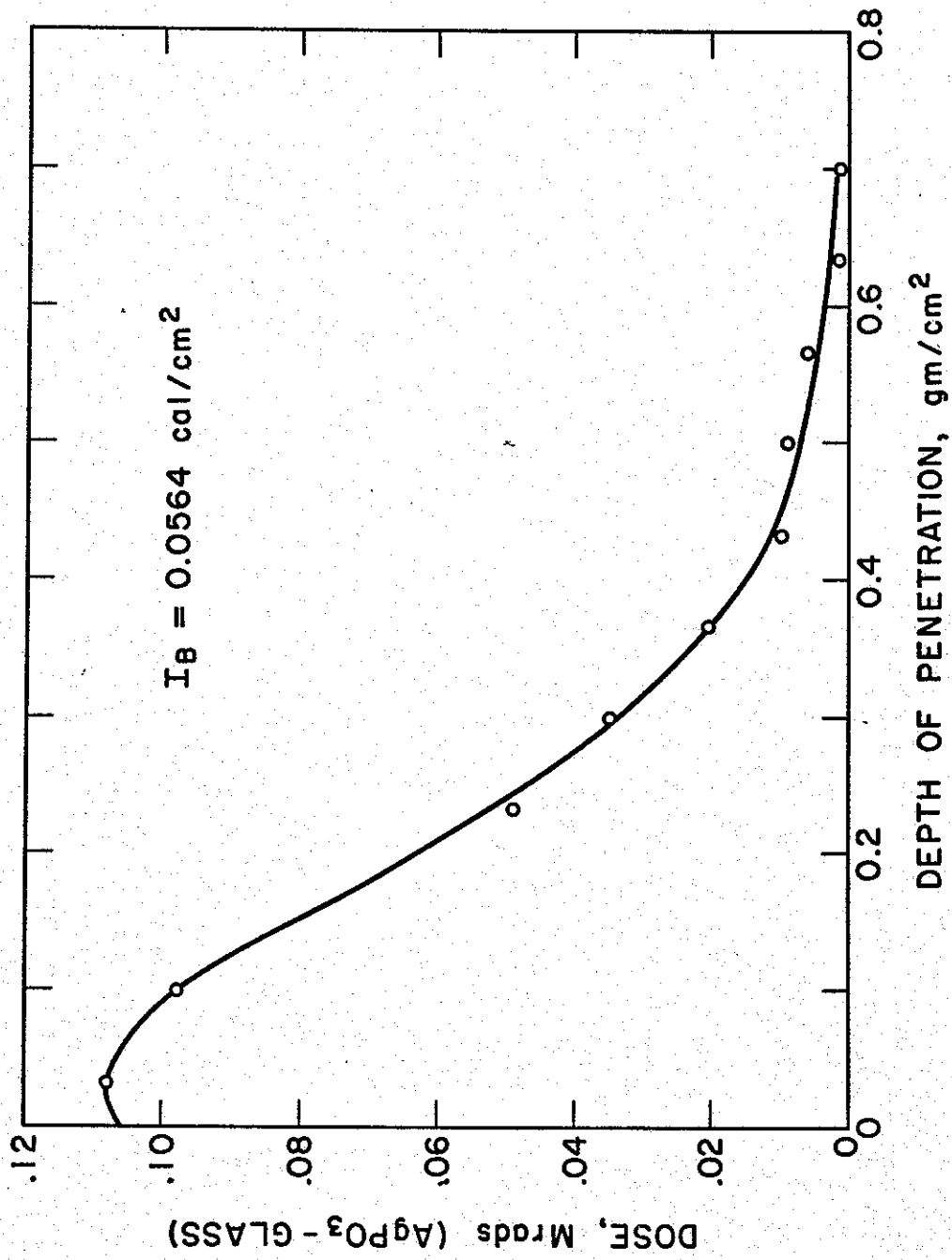
Figure 3.11d. Electron energy deposition vs. penetration in silver phosphate or cobalt glass at the 3.5", 30° position

As previously observed, the dose-depth curves, initially characteristic of low energy electrons, possess extrapolated ranges indicative of much higher energies.

In addition to the above deposition profiles, profiles were measured with #25 Cinemoid at various distances along the axial centerline of the machine. As stated in Section II, accurate energy information can only be obtained when the dose-depth curves are produced by a monoenergetic electron beam incident normally upon the stack of dosimetry material. The effective and maximum energies determined for Tube A-313 in air using #25 Cinemoid are presented in Figure 3.12 as a function of position on the beam axis. The solid curve for maximum energy was determined from available stopping power information for 1.5-MeV electrons in air.[21] The solid curve for effective energy is merely a best curve through the experimental points. As discussed in Appendix B, the effective energy is less than the average energy, which indicates that the average energy is expected to be greater than, but on the order of, 1 MeV. As stated earlier, the average energy has not yet been measured directly but this information will be obtained in the near future. These results for effective and maximum energies are compared with aluminum calorimeter results in Table III.1 and as can be seen the results for the two materials agree fairly well.

Table III.1

Effective and Maximum Energies
for #25 Cinemoid and Al

Position on Beam Axis	E_{eff}(MeV)		E_{max}(MeV)	
	#25 Cinemoid	Al	#25 Cinemoid	Al
5" (Unknown tube for Al, tube no. 313 for Cinemoid)	0.80 ± 0.11	0.91 ± 0.09	1.34 ± 0.13	1.47 ± 0.15
5" (tube no. 297)	0.89 ± 0.13	0.89 ± 0.09	1.48 ± 0.15	1.34 ± 0.13

D. Beam Energy Density

As mentioned in Section II.A, the beam energy density may be obtained by integrating the dose-depth curves. The results obtained in this way for three separate type A tubes are presented in Figures 3.13, 3.14, and 3.15 as a function of distance from the tube window on the beam axis. The
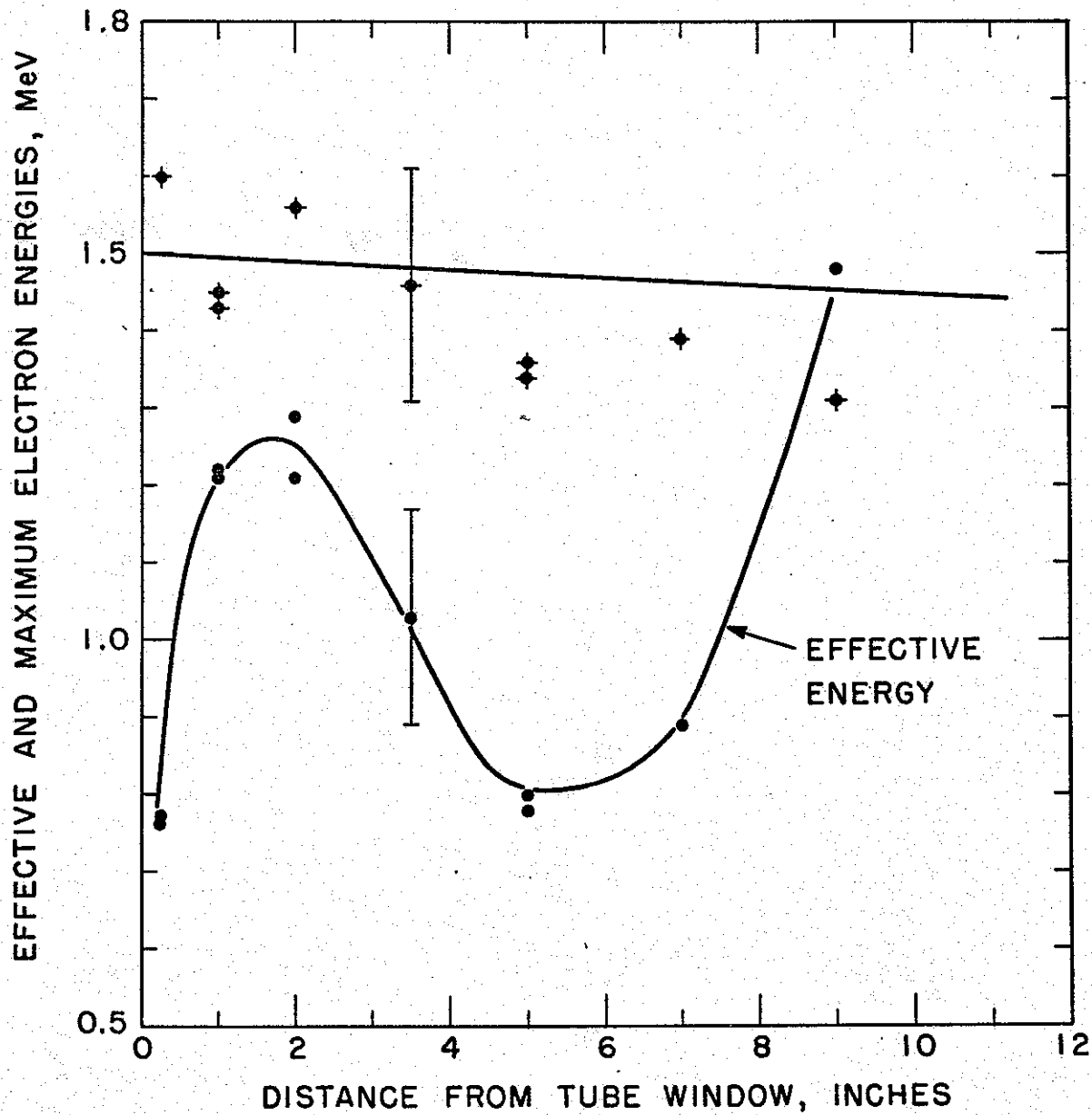
Figure 3.12. Effective and maximum electron energies vs. distance from the tube surface as measured with #25 Cinemoid
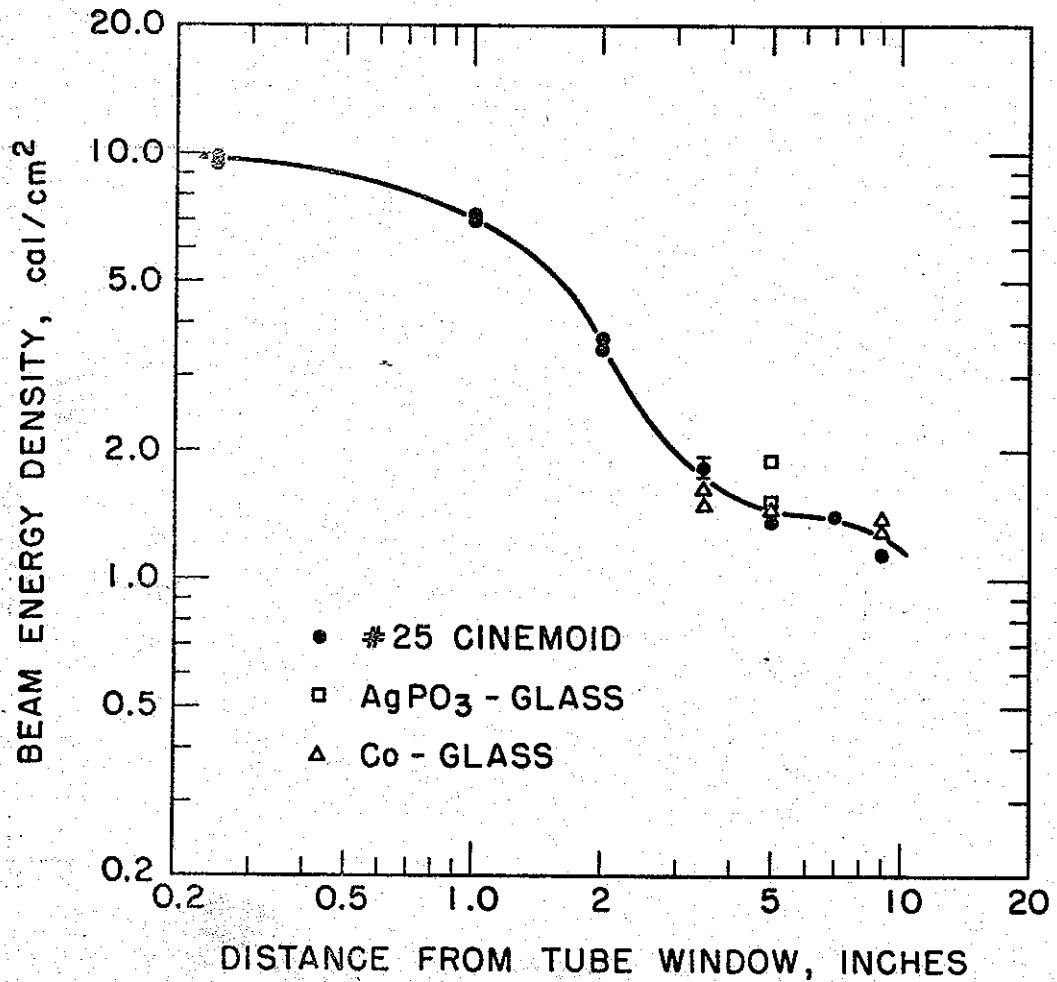
Figure 3.13. Electron beam energy density vs. distance from tube window as measured with Cinemoid, silver phosphate, and cobalt glass - Type A tube No. 313, and atmospheric pressure
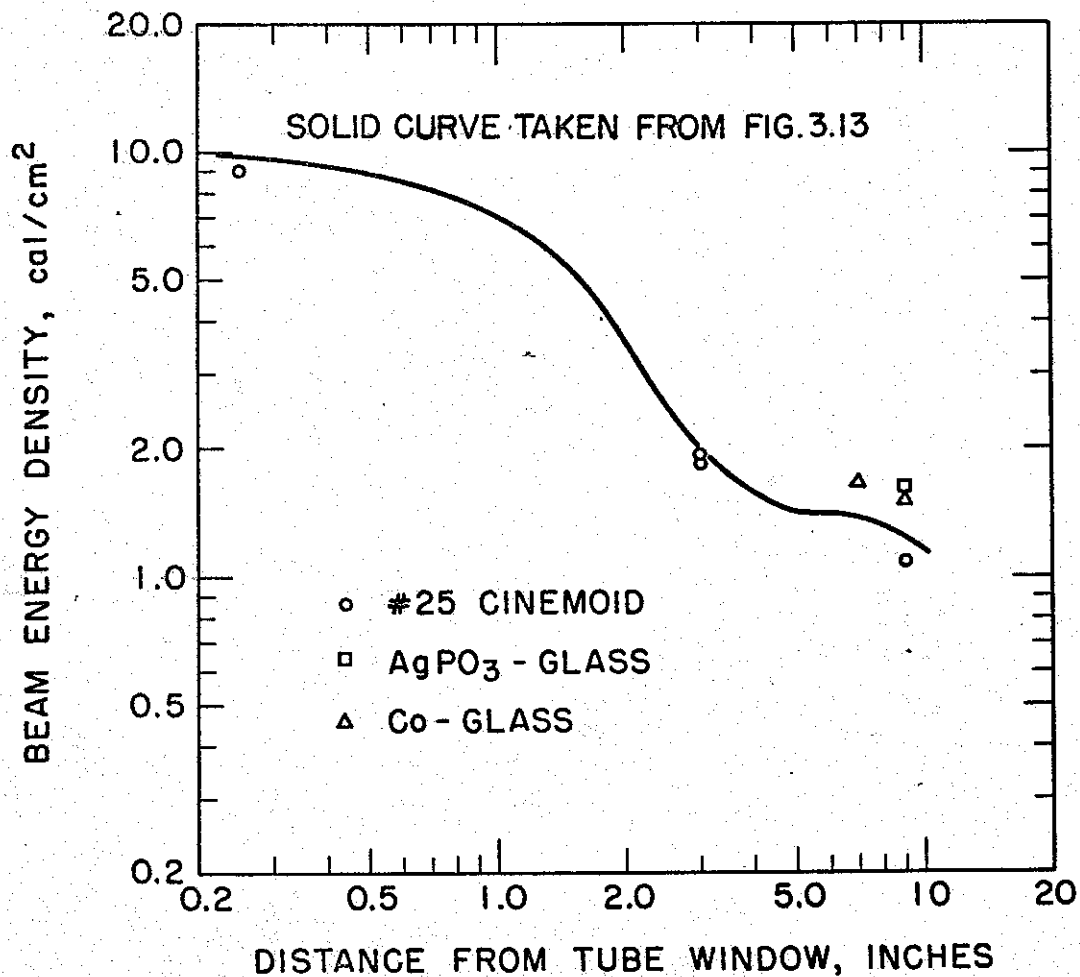
Figure 3.14. Electron beam energy density vs. distance from tube window as measured with Cinemoid, silver phosphate, and cobalt glass -- Type A tube No. 312, and atmospheric pressure
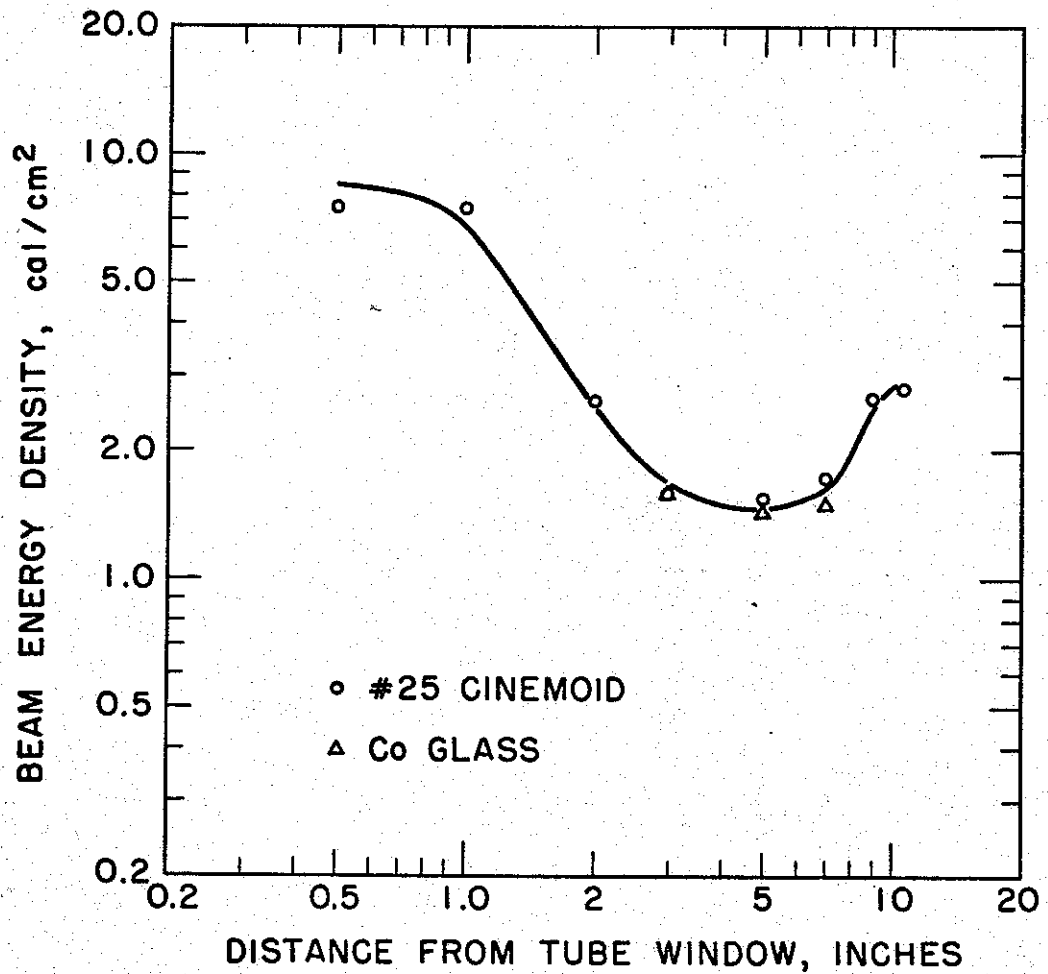
Figure 3.15. Electron beam energy density vs. distance from tube window as measured with Cinemoid and cobalt glass -- Type A tube, No. 297, 300 μ pressure

materials used to make these measurements were #25 Cinemoid, cobalt glass, and silver phosphate glass. The various materials are found to give results that are relatively consistent with one another. Initially the energy density falls off quite rapidly but then levels off or exhibits a maximum as a result of the "Bennett" pinch which is more pronounced for a pressure of approximately 300 μ than at atmospheric pressure, as can be seen from a comparison of Figures 3.13 and 3.15.

Measurements of the beam energy density, with cobalt glass and silver phosphate glass, at three focussing fields are shown in Figure 3.16. These results are consistent with those presented in the last section for the dose-depth curves in #25 Cinemoid, i.e., the energy density of the beam decreases with decreasing focussing field. This is probably the result of more disperse trajectories of the electrons at the lower focussing fields.

The dose-depth measurements on and off the axis mentioned in the last section were used to obtain the beam energy density as a function of angle from the beam axis at 3.5 inches and 9 inches from the tube window. The results are presented in Figure 3.17 where the focussing phenomenon at 9 inches is quite evident inasmuch as the energy density falls off more rapidly at 9 inches than 3.5 inches.

E. Energy Spectrum

As stated earlier, the energy spectrum measurements with the magnetic spectrometer were certainly not representative of the entire electron beam, due to the fact that the presence of the focussing field makes it very difficult to place the spectrometer close enough to the tube window to intercept a substantial portion of the electron beam while at the same time keeping the perturbation caused by the focussing field at an acceptable level. The results are, however, in relatively good agreement (in terms of shape and position of pronounced peaks) with other measurements on the Febetron 705 and other field emission devices. The film traces obtained in these measurements show that peaks exist at about 1.5, 1.0, and 0.6 MeV. The higher energy peak is much more pronounced than the lower two.

Typical results for a single pulse are presented in Figure 3.18 showing the medium and high energy peaks in the spectrum. Due to the fact that the absolute sensitivity of type AA and KK films has not as yet been determined,
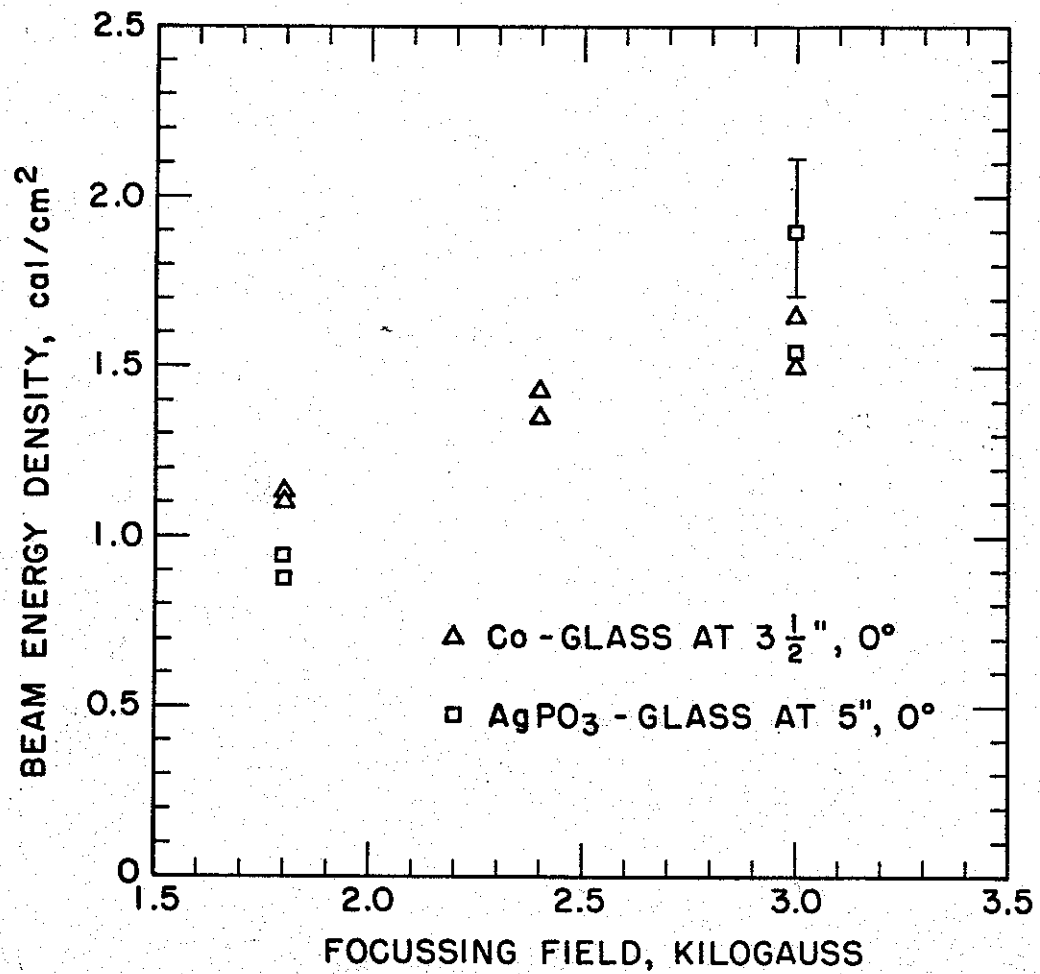
Figure 3.16.   Electron beam energy density vs. focussing field as measured with cobalt and silver phosphate glass
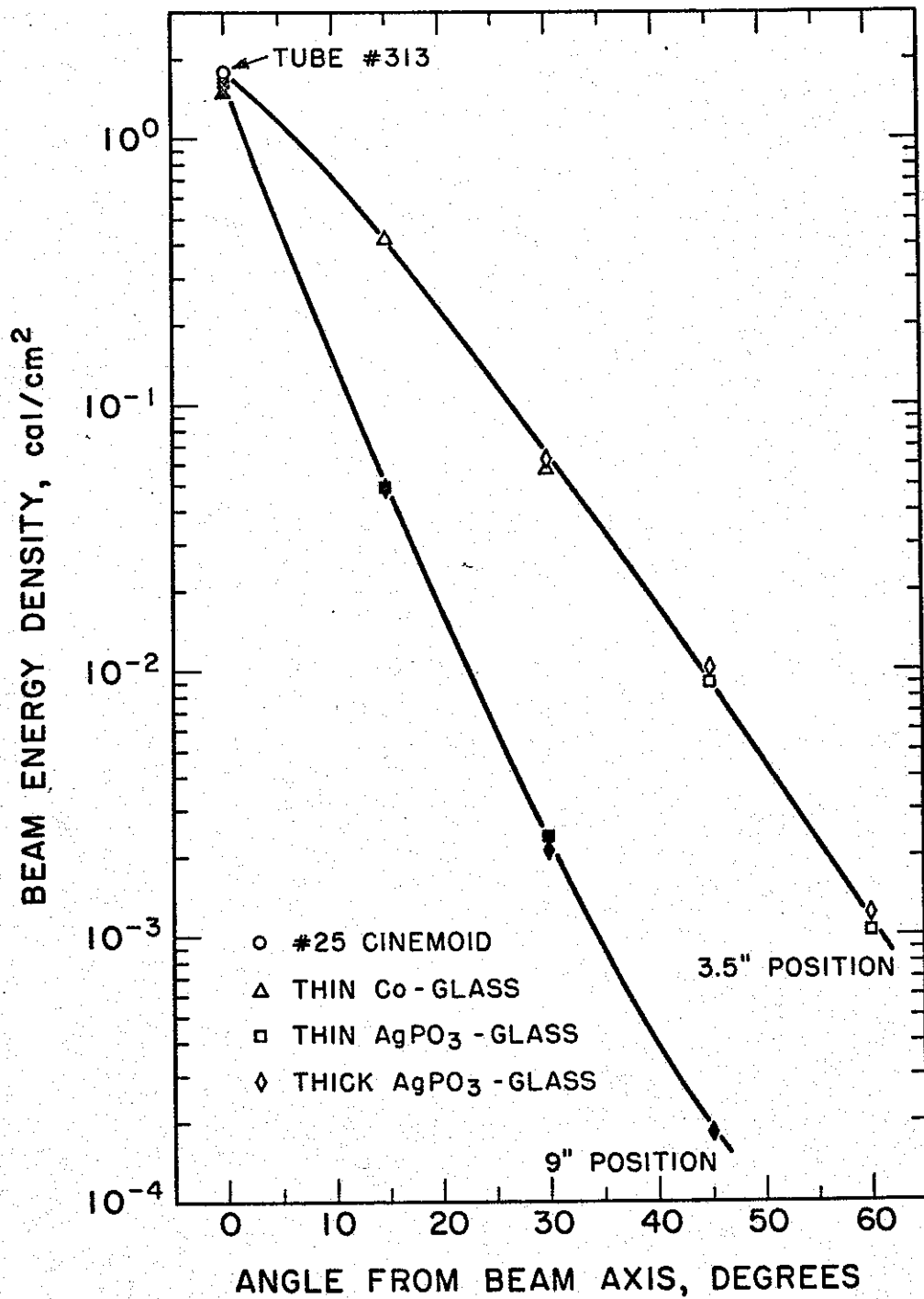
Figure 3.17. Electron beam energy density vs. angle from beam axis as measured with #25 Cinemoid, cobalt, and silver phosphate glass -- 3.5" and 9" from tube window
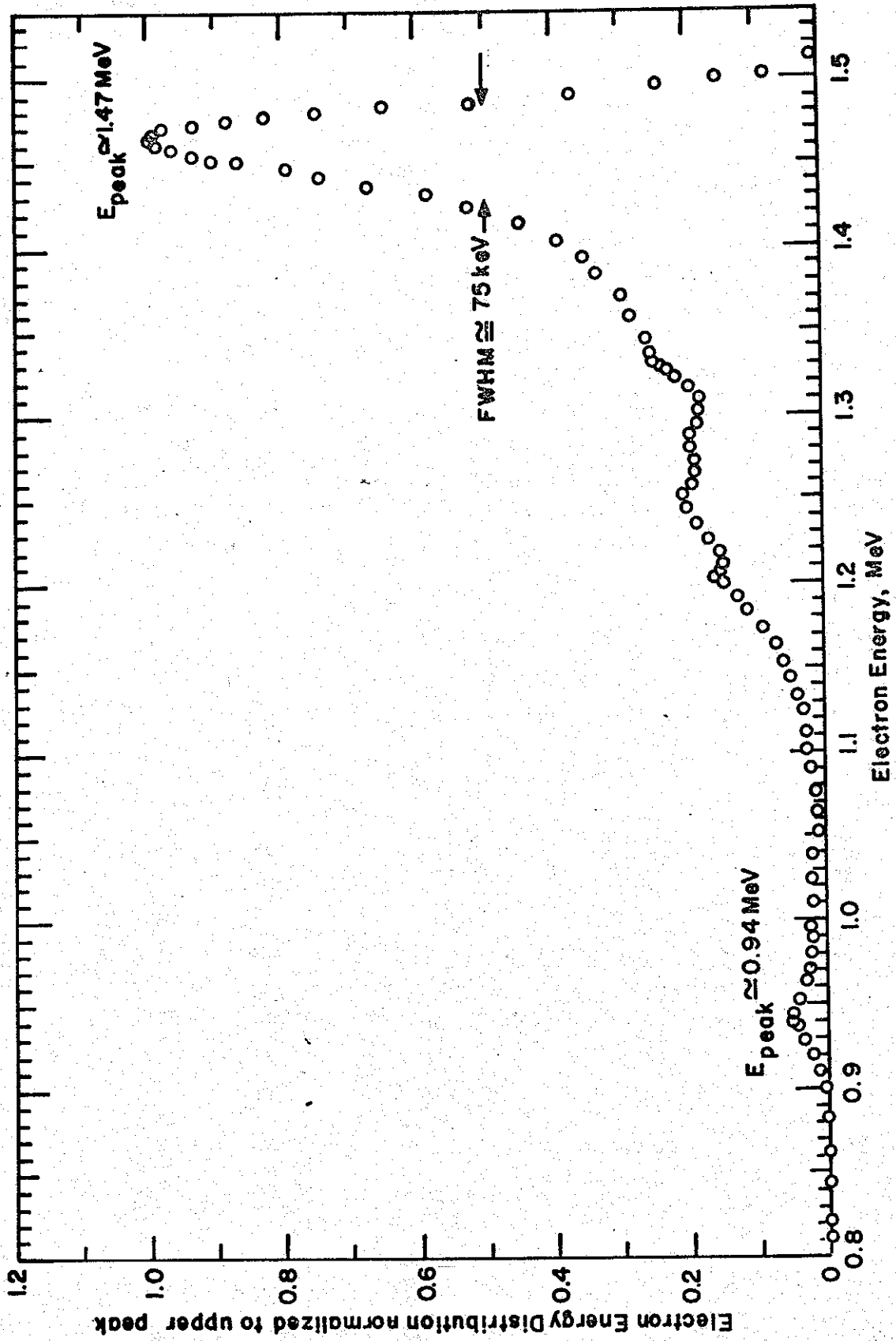
Figure 3.18. Electron differential energy spectrum as measured with the Sandia magnetic spectrometer

83

the relative electron energy distribution only is presented in this figure. It is seen that the high energy peak falls at 1.47 MeV, which is in good agreement with the results of the aluminum absorption measurements in light of the fact that in each case a different tube was used.

The energy and magnitude of the high energy peak were found to be much more reproducible from shot to shot than that of the lower energy peaks. This spectrum is much closer to being monoenergetic, possessing a full width at half maximum of only 75 keV, than was initially expected in light of the long tail existing on the voltage profile; this is probably due to the poor geometry (small intercepted solid angle) employed. An error of $\pm$ 10 to 15 percent is presently estimated for the relative electron energy distribution, and this represents uncertainties arising from the assumed energy dependence of the response of the type KK film (see Section II.C), the difficulty encountered in the transverse integration of the optical density at a point along the film, and the theoretical expression employed relating the electron energy and position on the focal plane. The energy resolution, arising from the finite size of the electron beam and its oblique angle of incidence upon the film as well as the fact that it is not a point source, is estimated to be approximately 8 keV and 4 keV for the 0.94 MeV and 1.47 MeV peaks, respectively. This degree of resolution may well be masked by non-uniformities in the film.

Various collimator arrangements were employed to look for space charge effects although such effects were never observed. In the course of this investigation it was found that decreasing the diameter of the precollimator drift section (see Figure 2.13b) resulted in a substantial decrease in the 1.0 MeV peak relative to the 1.5 MeV peak. This is but another indication of the complex trajectories of the electrons in the beam. These results can be compared with measurements made by the Field Emission Corp. on the same model Febetron at the same charging voltage, the results of which are shown in Figure 3.19 where EN(E) is plotted versus E. The higher energy end of the spectrum is similar in both cases, but the Field Emission results show a much more pronounced 1-MeV peak; this, in all likelihood, is a result of the fact that these measurements are reported to be representative of half the beam, whereas the results reported herein sampled only a small solid angle.

The technique employed in the Field Emission measurements is that of observing the time resolved electron beam current passing through various
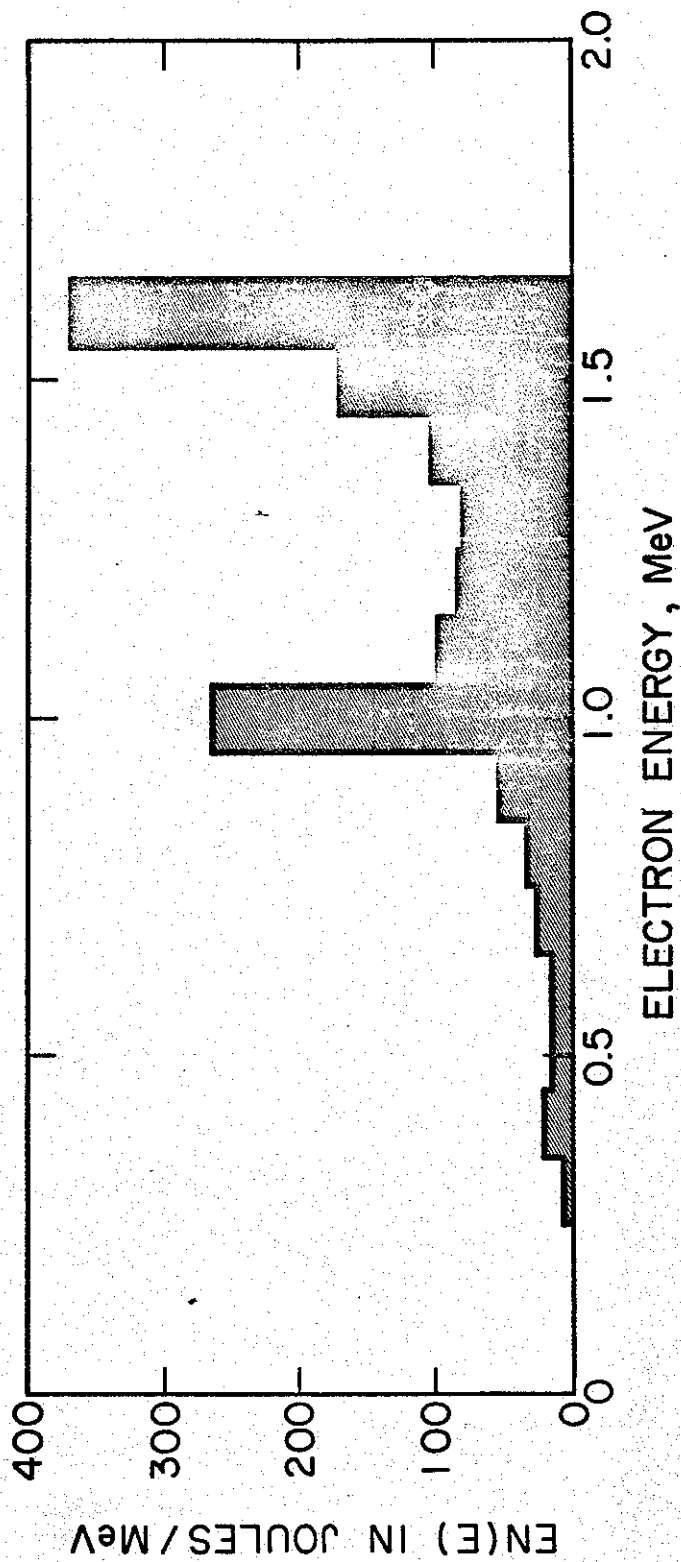
Figure 3.19.   Electron differential energy spectrum vs. electron energy as measured by the Field Emission Corporation using the aluminum differential absorption technique

thicknesses of Al absorber. In this way various portions of the current pro-
file can be characterized by average energies, for a normal-incident beam,
and in this way a histogram of the energy distribution is constructed. It
should be pointed out that the angular divergence of the electron beam intro-
duces uncertainties in the determination of the average energy associated
with each portion of the beam.

In Figure 3.20 measurements by Graybill and Nablo[10] on a field emission
device using a Van de Graaff accelerator to produce the charging potential
are also presented for comparison. These results correspond to a charging
potential of 2.6 megavolts and a 180° fixed-field magnetic spectrometer was
used to measure the spectrum. This spectrometer design employed a number of
Faraday cups on the focal plane for electron detection. As can be seen in
this figure, the shape is generally the same as in Figure 3.18 although the
lower energy peak is not distinctly separated from the shoulder of the high
energy peak. These results are also characteristic of only a small portion
of the beam, although for an IP x-ray machine this may not be as important
as for the Febetron 705 since the IP machine does not employ a focussing
field.

The previously mentioned effective energy measurements suggest that,
in the case of the Febetron 705, the 0.6 MeV peak may even be more pronounced
than indicated in Figure 3.18 for the electron differential energy spectrum
characteristic of the entire beam. As already mentioned, this is further
indicated in our measurements by the fact that varying the type of collimator
system employed resulted in a decrease in the magnitude of the lower energy
peaks when a collimator is employed which constricts the precollimator pas-
sage.

In Section II.C it was indicated that it is possible to obtain informa-
tion characteristic of the entire beam using the current and voltage wave-
forms, providing the tube shank inductance can be determined. This tech-
nique was employed on the Sandia Model 705 Febetron No. 2 where a timing
synchronization of the two waveforms of about 2 to 3 nsec was realized. At
this time only the results obtained assuming $L = 0$ can be presented since
accurate estimates of the tube shank inductance are not available. These
results are shown in Figure 3.21 for a charging potential of 30 kV and a
focussing field of 3200 gauss. Two distinct groups are evident but their
energies are somewhat high which is to be expected for the assumed zero shank
inductance. These results do, however, show a sizeable low energy group (at
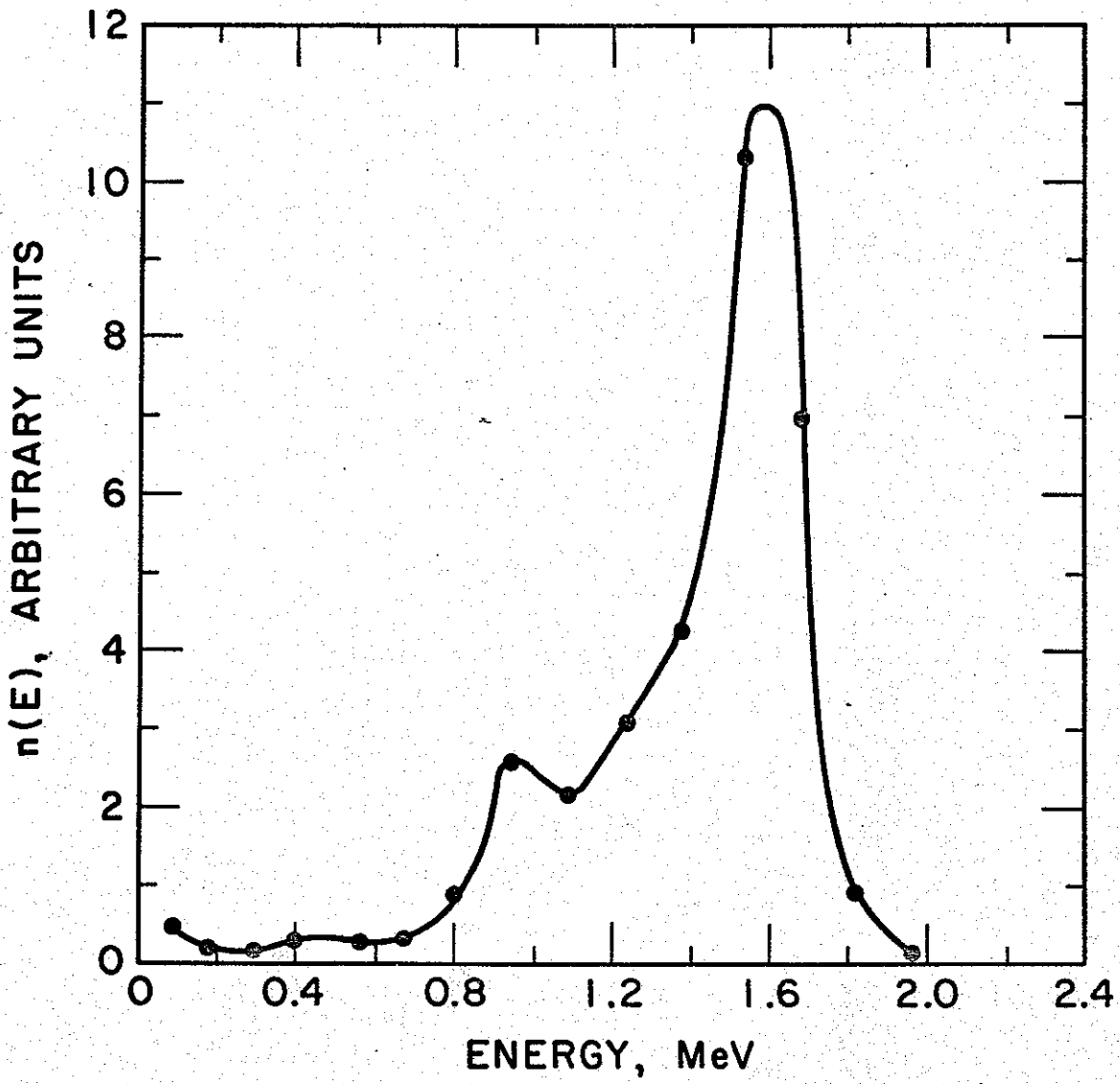
Figure 3.20.   Electron differential energy spectrum from a
               Van de Graaff field emission device as
               measured by Ion Physics
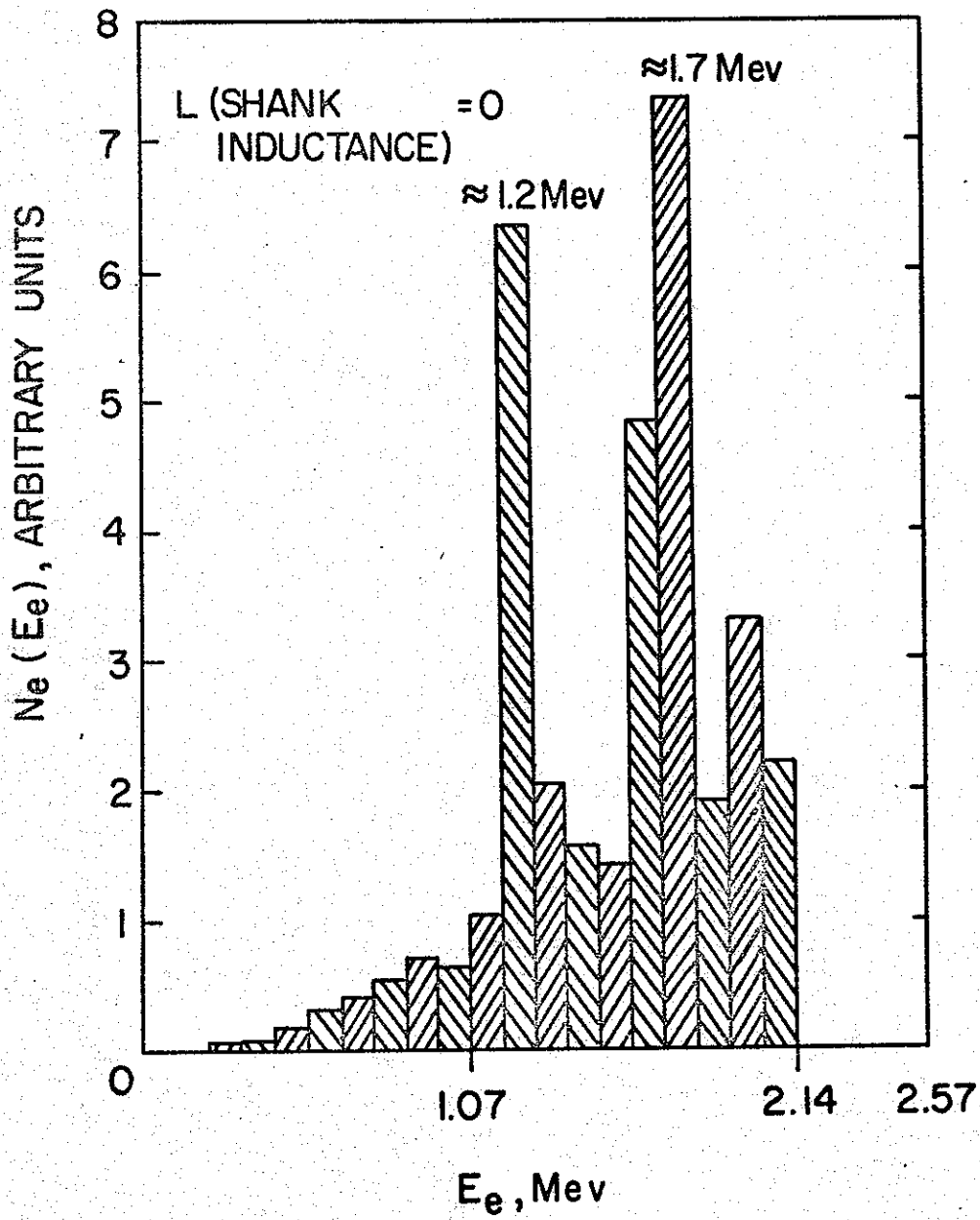
Figure 3.21. Differential energy spectrum obtained from the current and voltage waveforms for the Sandia Model 705 Febetron No. 2 operating at 30 kV charging potential and 3200 gauss focussing field

approximately 1 MeV). The inclusion of a finite shank inductance will lower the energy of these two groups, but the beam energy spectrum should still possess a sizeable low energy component.

IV. SUMMARY AND CONCLUSIONS

For pulsed electron beams of sufficient energy density, partial-absorbing and total-stopping calorimeters yield the most accurate energy deposition profile and beam energy density information, provided backscattering and bremsstrahlung corrections are not too large and that such corrective information is available. This corrective information is required if the total-stopping calorimeter is to ultimately yield the actual energy density incident on the front surface of the calorimeter. Use of bremsstrahlung and electron reflection data should be applied with discretion since these data are strongly dependent on electron energy. Additionally, care should be taken in the interpretation of results obtained on electron beams possessing sufficient energy density to produce calorimeter temperature rises for which radiation heat transfer becomes important. Calorimeters of a size comparable to the experimental samples should be used to determine I_B and dose to given samples in beams possessing a high degree of spatial nonuniformity.

The passive dosimetry materials (glasses and plastics), although useful at lower beam intensities and more easily employed in the determination of deposition profiles than calorimeters, possess a larger precision uncertainty and are in practice less accurate than the calorimeters. In addition, when dielectric passive dosimetry materials are employed, care should be taken to insure that space-charge effects, rate-saturation effects, and environmental effects can be eliminated or properly accounted for. In spite of the above mentioned deficiencies characteristic of the plastics used in electron beam diagnostics, these plastics possess a distinct advantage over the calorimetric method in electron beam spatial profile measurements. Since the plastics are analyzed optically, spatial profiles obtained with these materials result in a continuous scan of the beam profile whereas, necessarily, calorimetric determinations result in a stepwise representation of average values for the beam profile.

Charge release and/or current profiles can be determined using a Faraday cup providing that a high current carrying capacity conductor leads from the catcher plate in the cup directly to the current viewing resistor (e.g.,

of the type produced by the T & M Research Products) and of as short a
length as possible.

Spectral information with varying degrees of energy resolution can be
obtained in a variety of ways. The lowest resolution information (i.e.,
average energy and extrapolated end-point energy information) can be deter-
mined for approximately the entire beam and these measurements are the eas-
iest to make. The time-resolved differential-absorption technique employed
by Field Emission Corp. yields moderate resolution spectral information that
is typically representative of approximately half the beam. This technique
is sensitive to the angular dispersion of the electron beam as is the tech-
nique which employs the energy deposition profile to determine the extra-
polated end-point energy. High resolution spectral information can be
obtained using electron magnetic spectrometers. Results obtained using
instruments of this type are, however, representative of but a small portion
of the beam (the beam fraction sampled being dependent upon the sensitivity
of the detectors employed) and, therefore, cannot be used to predict infor-
mation representative of the entire beam for those beams possessing substan-
tial angular dispersion. In principle, it is possible to get high resolu-
tion spectral information that is representative of the entire beam from
synchronized tube voltage and beam current time histories. However, the
application of this technique requires an accurate knowledge of tube shank
inductance in order to obtain meaningful energy, as well as differential
number, spectra information.

As far as the Sandia Model 705 Febetrons are concerned, beam energy
density measurements can be made using totally stopping calorimeters such
as Al or Cu or stacks of various passive dosimetry materials (e.g., silver
metaphosphate glass, Cinemoid, etc.) while thin calorimeters can be used to
determine the dose to thin samples of various materials. Energy deposition
profiles in Al, which should be representative for low Z materials, can be
determined using a linear array of thin Al calorimeters. Linear array
calorimeters can also be used to find the energy deposition profile in a
variety of other materials.

Energy spectrum information suitable for general use is not so easily
obtained due to the spatial complexity of the electron trajectories in the
electron beam produced by these machines. Any one of the spectroscopy tech-
niques mentioned above which is compatible with the portion of the beam to
be intercepted by a test can be employed to obtain pertinent spectral infor-
mation.

In general, the angular dispersion of the electron beam from the Model 705 Febetron machines is such that any beam diagnostics performed should sample the same portion of the beam to be employed in the experiment.

Electron beam diagnostics on the higher energy machines, Hermes I, Reba, etc., are amenable to the same techniques as applied to the Febetron 705 machines provided the measurements are out of the region of intense electron pinch. Outside of the "pinch" region total stopping calorimeters of various Z materials have proved quite satisfactory. Partial absorbing calorimeters, particularly graphite and titanium, have been used with good results in these regions. Plastics may be used in regions of relatively low electron energy densities, i.e., 20 cal/cm^2 or less.

To date, the only diagnostic method used with any degree of confidence in regions of intense electron beam energy density has been the total stopping graphite calorimeter.

In regards to electron energy spectrum measurements, any of the techniques described above (as used with the Febetron 705's) should be applicable to the higher energy machines. Implicit with these techniques is, of course, good machine repeatability. The previously mentioned remarks concerning beam angular dispersion and sample dosimeter size are equally applicable to the higher energy machines.

References

1. Rauch, J. E., and Andrew, A., "Breakdown in Dielectrics Due to Pulsed Electrons," IEEE Trans. Nucl. Science, Vol. NS-13, No. 6, 109 (1966).

2. Gross, B., and Nablo, S. V., "High Potentials in Electron-Irradiated Dielectrics," J. Appl. Phys. 38, 2272 (1967).

3. Lackner, H., Kohlberg, I., and Nablo, S. V., "Production of Large Electric Fields in Dielectrics by Electron Injection," J. Appl. Phys. 36, 2064 (1965).

4. Dow, J., and Nablo, S.V., "Time Resolved Electron Deposition Studies at High Dose Rates in Dielectrics," IEEE Trans. on Nucl. Science, NS-14, No. 6, 231 (1967).

5. Goodman, A., "The Direct Measurement of the Gruneisen Parameter," SC-TM-67-13, April 1967 (unpublished).

6. Graham, R. A., and Hutchison, R. E., "Thermoelastic Stress Pulses Resulting from Pulsed Electron Beams," Appl Phys. Letters 11, 69 (1967).

7. Bennett, W. H., "Magnetically Self-Focussing Streams," Phys. Rev. 98, 1584 (1955); 45, 890 (1934).

8. Graybill, S. E., and Nablo, S. V., "Techniques for the Study of Self-Focussing Electron Streams," 8th Annual Symposium on Electron and Laser Beam Technology, April 1966.

9. Oswald, R. B., Eisen, H. A., and Conrad, E. E., "Pulsed Electron Beam Dosimetry," IEEE Trans. Nucl. Science NS-13, 229 (1966).

10. Graybill, S. E., and Nablo, S. V., "Electron Beam Diagnostics on FX1, the Ion Physics Corporation's Pulse Electron Facility," Ion Physics Corp. (unpublished).

11. Model 705 Febetron Technical Bulletin, Field Emission Corp., McMinnville, Oregon.

12. Miller, D., Schlosser, P., Burt, J., and Glower, D. D., "A Pulsed Radiation Energy Spectrometer Using Ferroelectrics," IEEE Trans. on Nucl. Science, NS-14, No. 6, 245 (1967).

13. Schulze, J. F., "Calorimeters for Measuring High-Energy, High-Intensity Pulsed Electron Beams," SC-TM-69-298, June 1969 (unpublished).

14. Koch, H. W., and Motz, J. W., "Bremsstrahlung Cross-Section Formulas and Related Data," Rev. Mod. Phys., Vol. 33, No. 2, Feb. 1962.

15. Berger, M. J., "Transmission and Reflection of Electrons by Aluminum Foils," NBS Technical Note 187, April 1963.

16. Wright, K. A., and Trump, J. F., "Back-Scattering of Megavolt Electrons from Thick Targets," J. App. Phys. Vol. 33, No. 2, Feb., 1962.

17. Menkes, C. K., and Goldstein, N., "Color Films for Megarad Dosimetry," USNRDL-TR-1097, Oct. 13, 1966.

18. McGuire, D., EG&G, private communication.

19. Buckalew, W. H., and Posey, L. D., "Rate Saturation Effects in Passive Dosimetry Materials," Sandia Corp. Research Report, to be published.

20. Spencer, L. V., "Energy Dissipation by Fast Electrons," NBS Monograph #1 (1959).

21. Berger, M. J., and Seltzer, S. M., "Tables of Energy Losses and Ranges of Electrons and Positrons," Studies in Penetration of Charged Particles in Matter, Publication #1133, Nat. Ac. Sci. - NRC, Washington, 1964.

22. Brown, K. L., and Tautfest, G. W., "Faraday-Cup Monitors for High-Energy Electron Beams," Rev. Sci. Instr. 27, 696 (1956).

23. Katz, L., and Penfold, A. S., "Range-Energy Relations for Electrons and the Determination of Beta-Ray End-Point Energies by Absorption," Rev. of Mod. Phys. 24, No. 1, Jan. 1952.

24. Browne, C. P., and Buechner, W. W., Rev. Sci. Instr. 27, 899 (1956).

25. Eastman Kodak Co., private communication.

26. Dudley, R. A., Nucleonics 12, No. 5, 24 (1954).

27. Touloukian, Y. S., "Thermo-Physical Properties of High Temperature Solid Materials, Elements," Vol. No. 1, MacMillan, New York (1967).

94

APPENDIX A

Technique for Determination of Effective Energy and/or Approximate Average Energy

Consider the situation in which an electron beam is incident upon a stack of dosimetry material. From the dose-depth curve obtained from the stack it is possible to determine the beam energy density and surface dose. The ratio of these two quantities for an electron beam that is <u>normally incident</u> upon the stack can be written as

$$\frac{I_B}{D(0)} = \frac{\int_0^\infty [E - \Delta E(E)] \phi(E) dE}{\int_0^\infty \frac{dE}{dx}\Big|_E J(0,E) \phi(E) dE} \qquad (A.1)$$

where I_B is the deposited energy density of the beam, $D(0)$ is the surface dose, $\phi(E)$ is the electron beam differential energy spectrum, $\Delta E(E)$ represents energy losses due to backscattering and bremsstrahlung production, $dE/dx|_E$ is the electron stopping power at energy E, and $J(0,E)$ is the surface energy dissipation function for <u>normally-incident</u> electrons defined by Spencer.[20] The function $J(0,E)$ may be either calculated or measured. Calculated values are available for Al and polystyrene[20] and in this report the polystyrene results have been used for Cinemoid.

At this point, let us limit our consideration to situations where $\Delta E(E)$ is but a few percent of E. This is a good approximation for either Al or Cinemoid in the energy range of 0.5 to 2 MeV. In this case Equation A.1 becomes

$$\frac{I_B}{D(0)} = \frac{\int_0^\infty E\phi(E) dE}{\int_0^\infty \frac{dE}{dx}\Big|_E J(0,E) \phi(E) dE} \qquad (A.2)$$

It should be pointed out that this ratio can be quite useful in determining the degree to which an electron beam is monoenergetic. Let us then further limit our consideration to a monoenergetic electron beam in which case Equation A.2 becomes

$$\frac{I_B}{D(0)}\bigg|_E = \frac{E}{\frac{dE}{dx}\big|_E J(0,E)} \equiv f(E) \tag{A.3}$$

where $f(E)$ is defined for convenience. The function $f(E)$ is plotted in Figure A.1 for Al and polystyrene where the $J(0,E)$ values of Spencer were used. Therefore, the ratio of the measured beam energy density to the measured surface dose uniquely determines the energy for a normal-incident electron beam. For a monoenergetic beam this value will be identical with the energy obtained from the extrapolated range. The range-energy relations for electron stopping in Al are known but are not available for Cinemoid.

In the event the beams were not monoenergetic, the electrons in the lower energy end of the spectrum would preferentially deposit their energy towards the front of the stack thus producing a larger increase in $D(0)$ than in I_B. The use of Equation A.3 on a spectrum, therefore, defines what is herein called the "effective energy;" i.e., the energy of a monoenergetic beam which would yield the same I_B and $D(0)$ as the spectrum in question although the "extrapolated range" must necessarily be different. The effective energy is then found from

$$\frac{I_B}{D(0)}\bigg|_{spectrum} = f(E_{eff}) \quad . \tag{A.4}$$

The above technique was tested by exposing a stack of #25 Cinemoid to the electron beam from a Van de Graaff accelerator operated at 1.8 MeV. In this case the electron beam is monoenergetic and normal incident. Results obtained from three exposures are presented in Figure A.2 where the dose has been normalized for comparison. As can be seen, the energy determined from the measured I_B and $D(0)$ using the polystyrene curve in Figure A.1 is in good agreement with the electron energy of 1.8 MeV (known to 80 keV). The solid curve is the deposition profile as predicted by Spencer for polystyrene. The shallower peaking in the experimental results are, in part at least, from the higher average atomic number of Cinemoid.
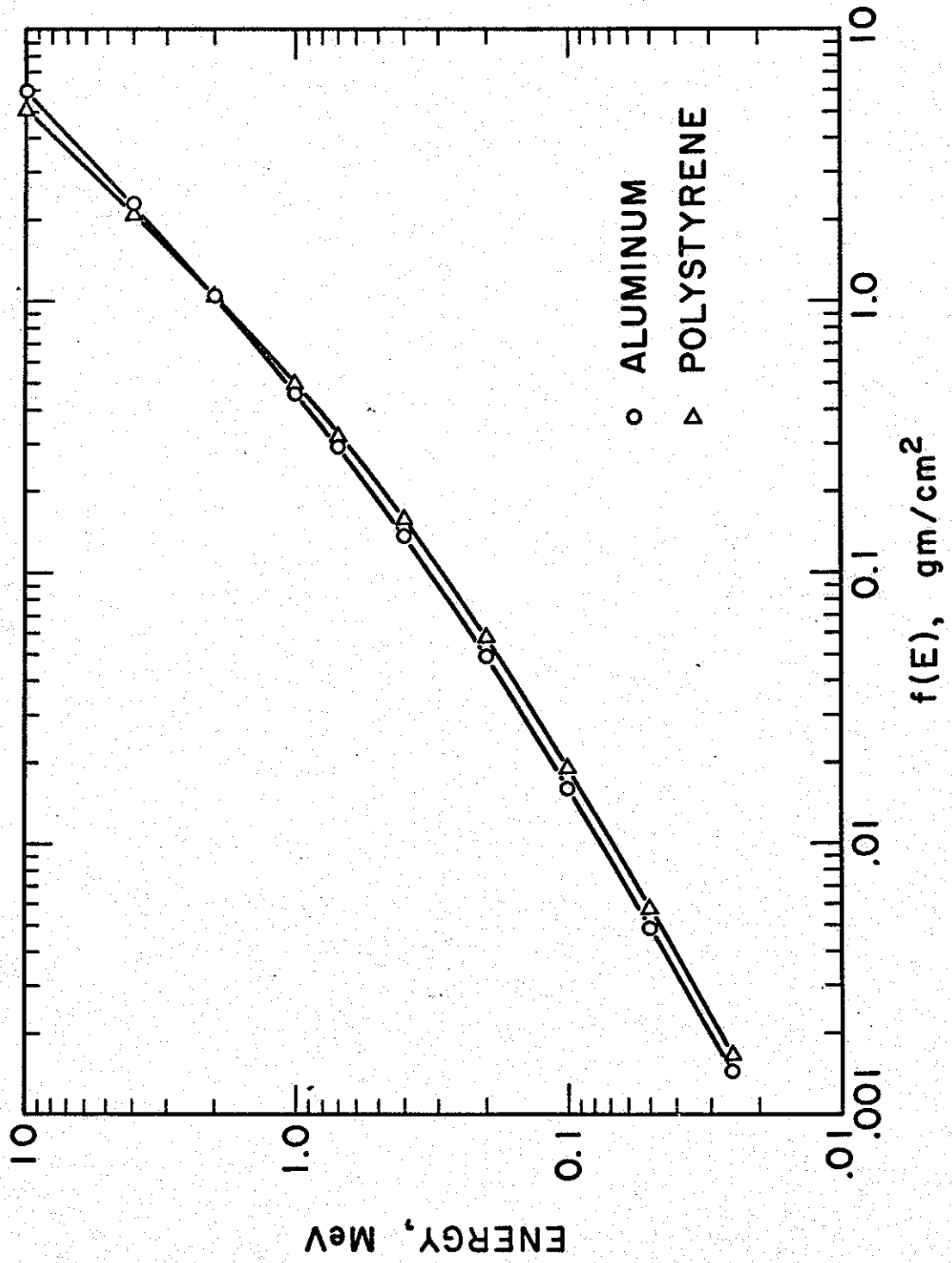
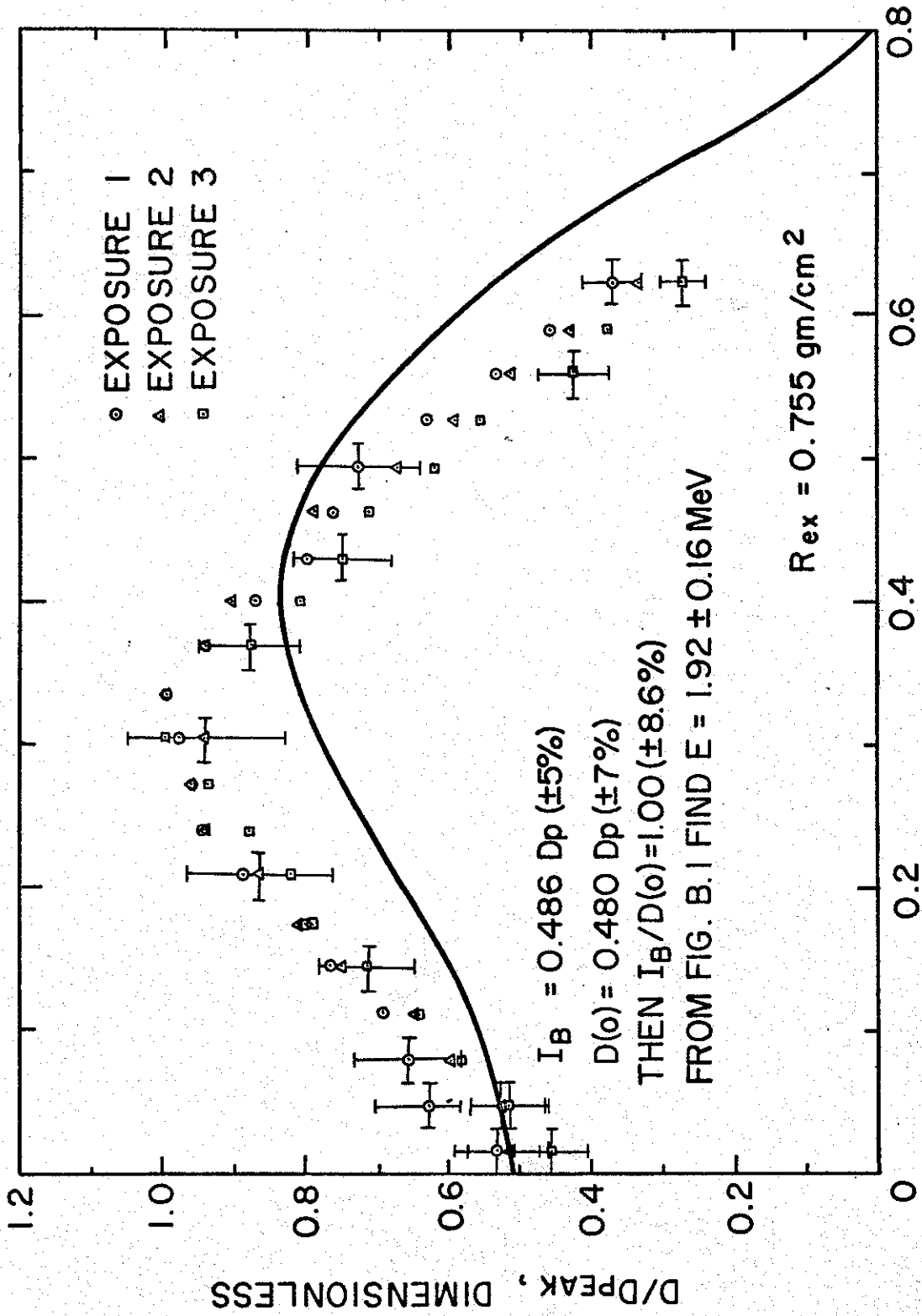Figure A.1. f(E) vs. E for aluminum and polystyrene

97

Figure A.2. Normalized energy deposition profile for
1.8 MeV electrons in #25 Cinemoid

Let us now return to the general case of a spectrum of electrons. Using the definition of $f(E)$ in Equation A.3, we can rewrite Equation A.2 in the form

$$\frac{I_B}{D(0)} \cong \frac{\int E\phi(E)dE}{\int \frac{E}{f(E)}\phi(E)dE} \quad . \tag{A.5}$$

It is possible to make a straight line fit to $f(E)$ in the energy interval from about 0.3 MeV to 2 MeV, as can be seen from Figure A.3. This is just the energy range of interest for the Febetron as was mentioned in Section III.E. Then, making use of the straight line approximation

$$f(E) = A + BE \tag{A.6}$$

in Equation A.5 yields

$$\frac{I_B}{D(0)} \cong \frac{\int E\phi(E)dE}{\int \frac{E}{A+BE}\phi(E)dE} = \frac{B\int E\phi(E)dE}{\int \frac{\phi(E)dE}{\left(1+\frac{A}{BE}\right)}} \quad . \tag{A.7}$$

It must be emphasized at this point that $(1 + A/BE)$ is close to unity only so long as $E > 0.3$ MeV, and therefore the steps which are to follow are only valid so long as $\phi(E)$ is effectively zero when $E < 0.3$ MeV (at an energy of 0.3 MeV, the factor $(A/BE) = -0.58$ for aluminum and this will decrease for higher energies). Expanding the quantity $1/(1 + A/BE)$ in Equation A.7 gives

$$\int \frac{\phi(E)dE}{\left(1+\frac{A}{BE}\right)} \doteq \phi(E)dE - \frac{A}{B}\int\frac{\phi(E)}{E}dE$$

$$+ \frac{A^2}{B^2}\int\frac{\phi(E)}{E^2}dE - \frac{A^3}{B^3}\int\frac{\phi(E)dE}{E^3} + \ldots \tag{A.8}$$

where the fourth term has been neglected since it will be 20 percent of the first term at 0.3 MeV and less at higher energies where the major contribution to the spectrum is expected. The information presented in Section III.E indicates that for the Febetron Model 705 most of the electrons are in the 1.0 to 1.5 MeV region, in which case
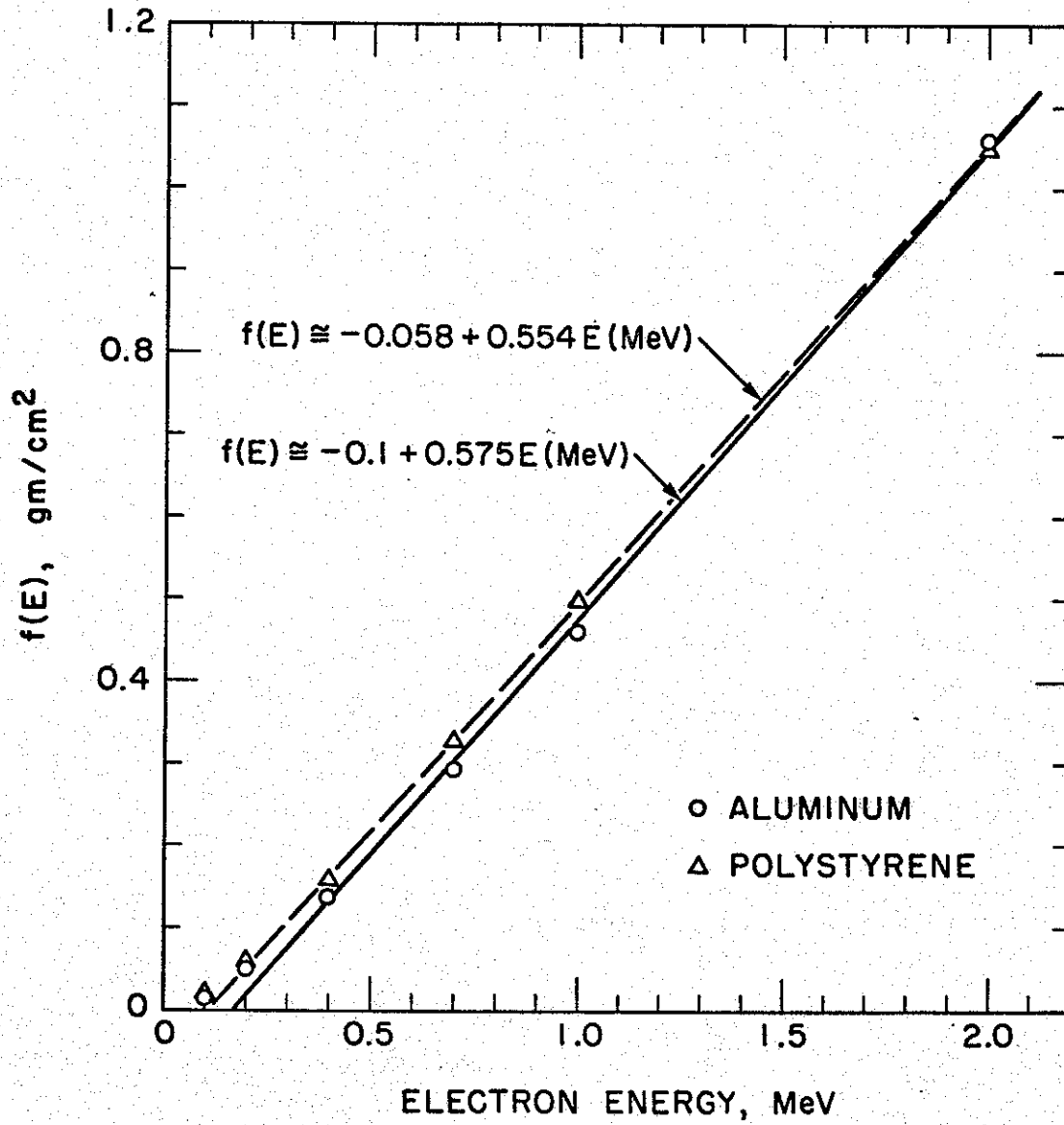
Figure A.3.   f(E) vs. E for aluminum and polystyrene, expanded scale

$$\frac{\int \phi(E)\frac{dE}{E}}{\int \phi(E)dE} = \overline{\left(\frac{1}{E}\right)} \lesssim 1$$

and

$$\frac{\int \phi(E)\frac{dE}{E^2}}{\int \phi(E)dE} = \overline{\left(\frac{1}{E^2}\right)} \lesssim 1 \quad .$$

Making use of these expressions in Equation A.8 yields

$$\frac{I_B}{D(0)} = B \frac{\int E\phi(E)dE}{\int \phi(E)dE} \frac{\int \phi(E)dE}{\int \frac{\phi(E)dE}{\left(1 + \frac{A}{BE}\right)}}$$

$$= \frac{B\overline{E}}{1 - \left(\frac{A}{B}\right)\overline{\left(\frac{1}{E}\right)} + \left(\frac{A}{B}\right)^2\overline{\left(\frac{1}{E^2}\right)}} = A + BE_{eff}$$

or

$$\overline{E} \cong \left(\frac{A}{B} + E_{eff}\right)\left[1 - \left(\frac{A}{B}\right)\overline{\left(\frac{1}{E}\right)} + \left(\frac{A}{B}\right)^2\overline{\left(\frac{1}{E^2}\right)}\right]$$

$$\approx \left(\frac{A}{B} + E_{eff}\right)\left[1 - \left(\frac{A}{B}\right) + \left(\frac{A}{B}\right)^2\right] \quad . \tag{A.9}$$

Since A/B is negative for both Al and Cinemoid, this last step will slightly overestimate the average energy. Using the values of A and B for Al this yields

$$\overline{E} \approx 1.21 \, E_{eff} - 0.21 \quad . \tag{A.10}$$

Expressions (A.9) and (A.10) can only be employed providing $\phi(E)$ is effectively zero below $E = 0.4$ MeV and the electron beam is incident normally upon the stack of dosimetry material.

An alternate, although somewhat rougher, approach would be to split the spectrum into a number of discrete groups with the lowest energy group falling at about 0.4 MeV and highest energy group at 1.5 MeV. Equation A.2 can be written

$$\frac{I_B}{D(0)} = \frac{\displaystyle\sum_{i=1}^{N} E_i \phi_i}{\displaystyle\sum_{i=1}^{N} J(E_i,0) \left.\frac{dE}{dx}\right|_{E_i} \phi_i} = \overline{E}\;\frac{\displaystyle\sum_{i=1}^{N} \phi_i}{\displaystyle\sum_{i=1}^{N} J(E_i,0) \left.\frac{dE}{dx}\right|_{E_i} \phi_i} \quad , \qquad (A.11)$$

where $i=1$ is the 0.4 MeV group and $i=N$ is the 1.5 MeV group. Factoring out ϕ_N and $J(E_N,0)\,dE/dx|_{E_N}\,\phi_N$ yields

$$\frac{I_B}{D(0)} = \left/\left(\frac{\overline{E}}{J(E_N,0)\left.\frac{dE}{dx}\right|_{E_N}}\right)\right. \frac{\left[1 + \displaystyle\sum_{i=1}^{N-1}\left(\frac{\phi_i}{\phi_N}\right)\right]}{\left[1 + \displaystyle\sum_{i=1}^{N-1}\left(\frac{J(E_i,0)\left.\frac{dE}{dx}\right|_{E_i}\phi_i}{J(E_N,0)\left.\frac{dE}{dx}\right|_{E_N}\phi_N}\right)\right]} \qquad (A.12)$$

Now,

$$\frac{\left[1 + \displaystyle\sum_{i=1}^{N-1}\left(\frac{J(E_i,0)\left.\frac{dE}{dx}\right|_{E_i}\phi_i}{J(E_N,0)\left.\frac{dE}{dx}\right|_{E_N}\phi_N}\right)\right]}{\left[1 + \displaystyle\sum_{i=1}^{N-1}\left(\frac{\phi_i}{\phi_N}\right)\right]} \geq 1 \qquad (A.13)$$

since $J(E_i,0)dE/dx|_{E_i}$ $(1 \leq i \leq N-1)$ $> J(E_N,0)dE/dx|_{E_N}$ in the energy interval 0.3 MeV to 1.5 MeV. A lower limit on the average energy is then found by assuming $\phi_N = 1$ and all other $\phi_i = 0$ while an upper limit is found by setting $\phi_1 = 1$ and all other $\phi_i = 0$, i.e.,

$$J(E_N,0)\frac{dE}{dx}\bigg|_{E_N} \left(\frac{I_B}{D(0)}\right) \leq \overline{E} \leq J(E_1,0)\frac{dE}{dx}\bigg|_{E_1} \left(\frac{I_B}{D(0)}\right) \quad . \tag{A.14}$$

For the case of Al this last expression would be

$$1.84\left(\frac{I_B}{D(0)}\right) \leq \overline{E} \leq 3.45\left(\frac{I_B}{D(0)}\right) \tag{A.15}$$

where the ratio $I_B/D(0)$ should be expressed in gm/cm^2. This last expression is so rough that normal incidence is not required, although if this condition is satisfied, the average energy would be closer to the lower limit while for a very disperse beam it would be closer to the upper limit.

APPENDIX B

Hermes I Electron Beam Diagnostics

In this appendix, typical beam diagnostics results obtained on Hermes I using the techniques described in the main body of the report are presented.

In light of the high energy density characteristic of the Hermes I electron beam, calorimeter material selection required careful consideration. In Figure B.1 the energy deposition required to produce a given temperature rise is presented for the materials which were selected to cover a broad Z range and to be capable of operation in high energy density beams. These curves are based, for the most part, upon the data from Touloukian[27] with additional data also considered. The points indicated for onset of radiation heat transfer correspond to the temperature at which 10 percent of the energy content of a sample would be radiated in one second. Total absorption calorimeters were fabricated using all these materials (all were single element calorimeters except for graphite where a planar array configuration was also employed), and linear array calorimeters were fabricated of all the materials but molybdenum. More information concerning the fabrication of these calorimeters can be found in the publication by J. F. Schulze.[13] In Figure B.2 one of the titanium linear array calorimeters is shown as well as the equilibrator in which the calorimeter array is placed in order to achieve electron equilibrium.

Results typical of the use of a graphite linear array calorimeter which, in general, samples but a small portion of the beam are shown in Figure B.3. In Figure B.3a results of three shots are shown at a position 0.5 inches from the tube anode on the axis of the drift chamber. The solid curve is the energy deposition profile predicted by Spencer[20] for 2.5 MeV (characteristic of the electron energy spectrum of Hermes I) electrons normally incident upon graphite. As can be seen from this figure, the measured deposition profiles peak at a shallower depth of penetration than the theoretical prediction. This is interpreted as resulting from the actual angular distribution of the electrons striking the graphite calorimeter array (i.e., the electron
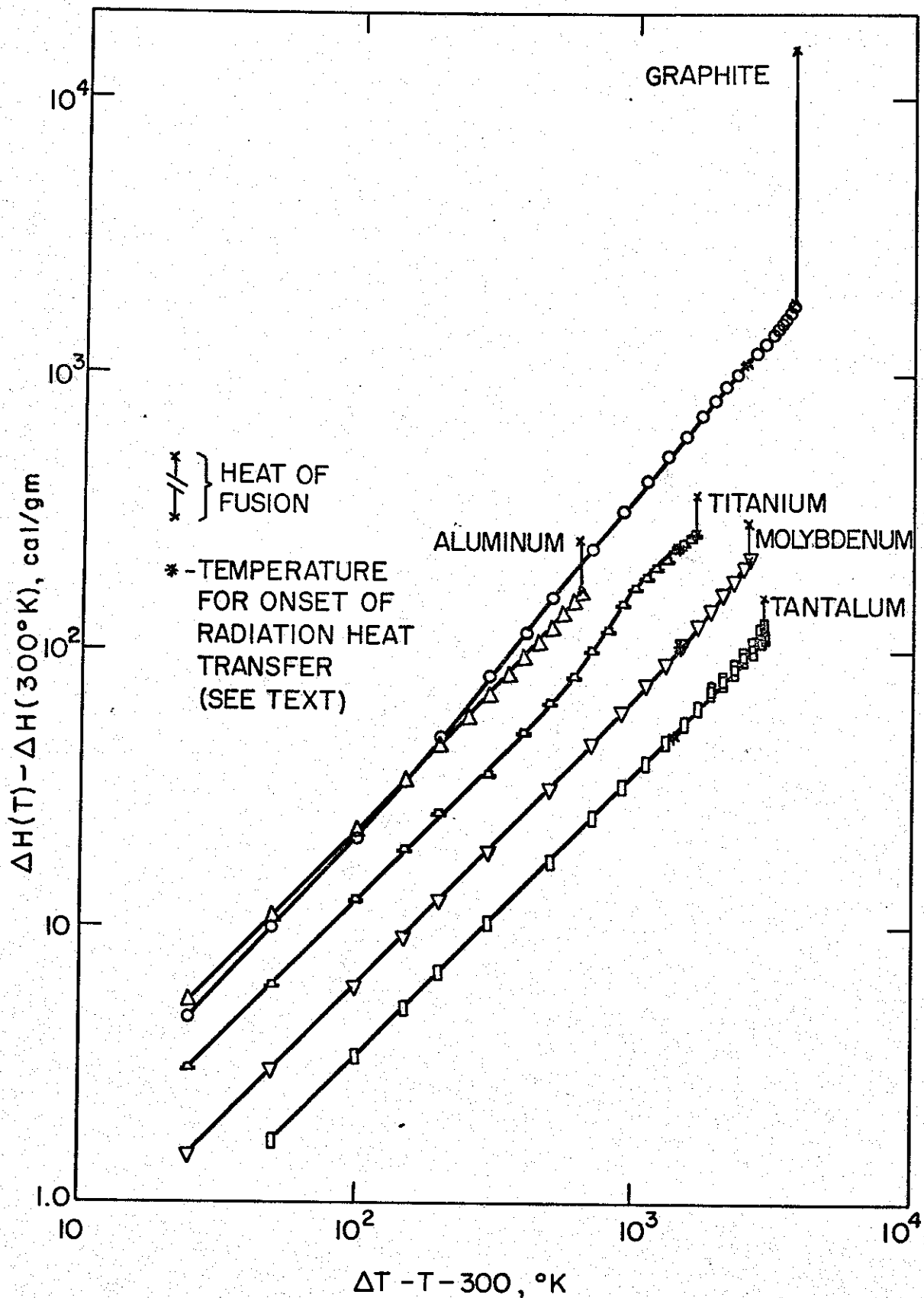
Figure B.1.   Enthalpy vs. temperature rise for various materials
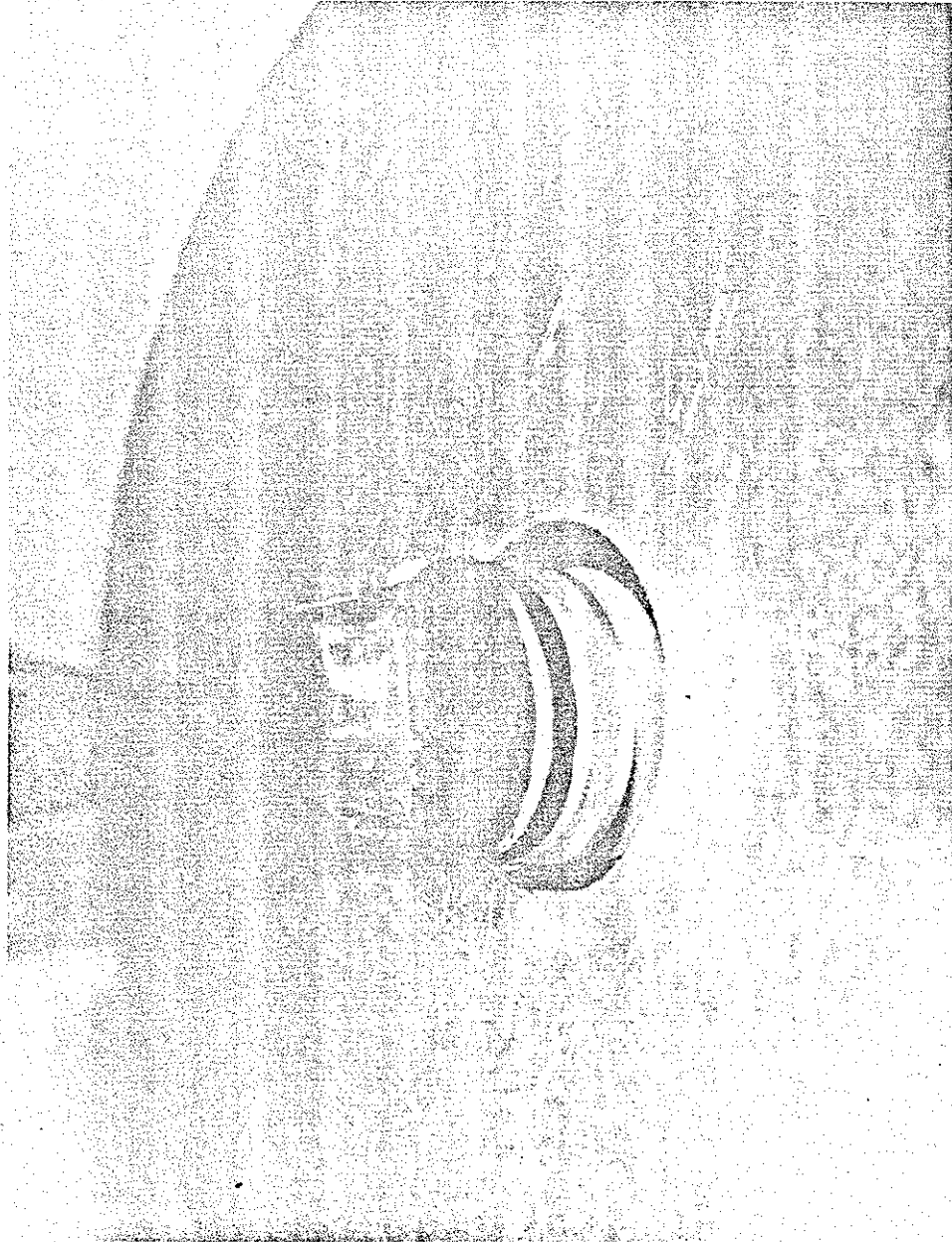employed in calorimeter fabrication

Figure B.2. Photograph of a titanium linear array
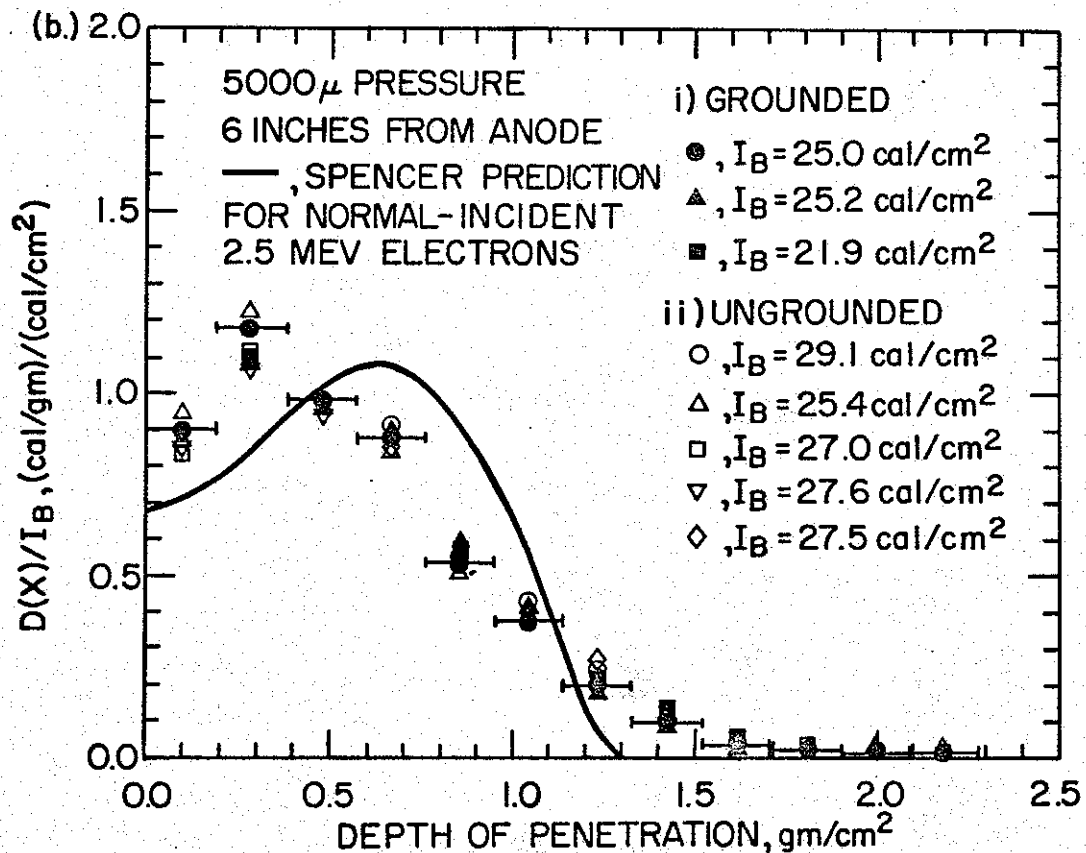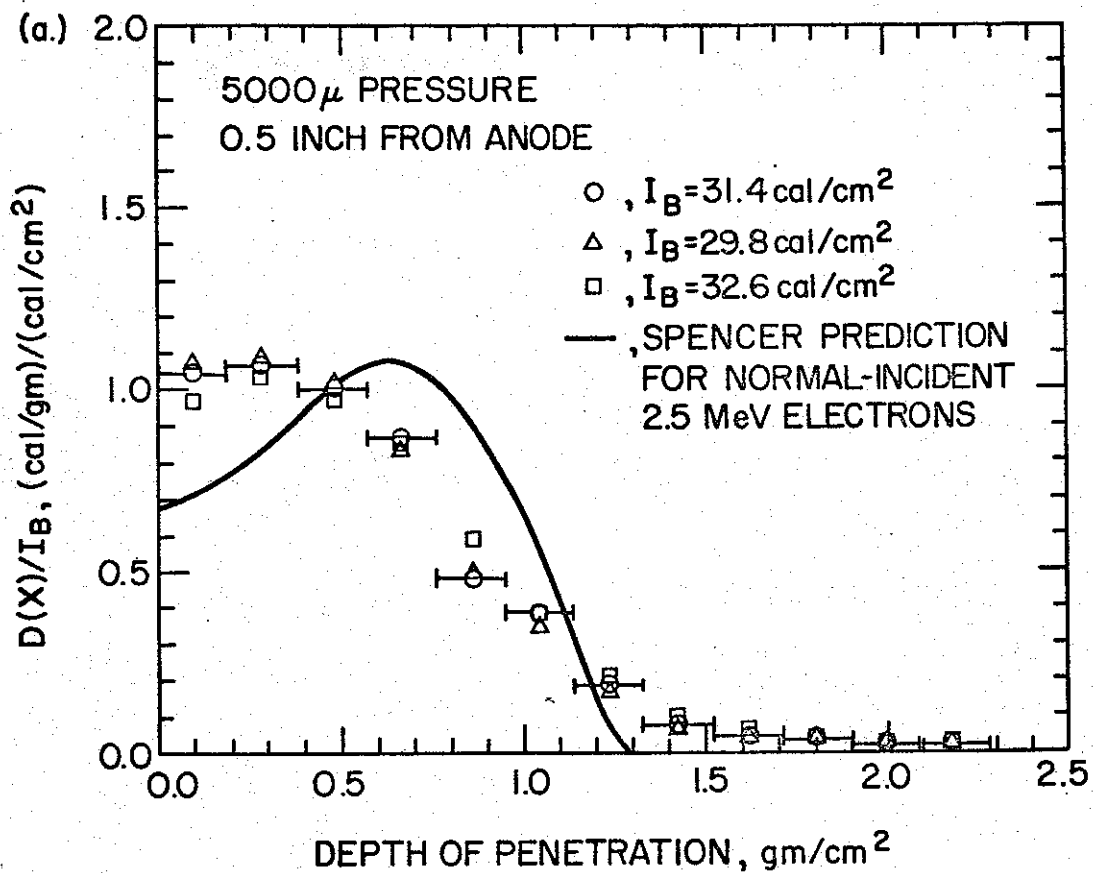calorimeter and equilibrator

Figure B.3. Energy deposition profiles in graphite on Hermes I at
(a) the 0.5 inch position, and (b) the 6 inch position

trajectories produce oblique angles of incidence) in light of the estimated energy spectrum of the electrons (see Figure B.9) where most of the electrons are found to have energies in excess of 2.5 MeV. In part (b) of this figure, results are presented for the situations in which (1) care was taken to make a good ground to the equilibrator, and (2) the equilibrator was left floating. The grounding condition of the equilibrator seems to have little effect on the energy deposition profile. The peak in the energy deposition profile is also shallower than the Spencer prediction at this 6 inch position but the peak is more pronounced, indicating an angular distribution closer to normal incidence and/or lower electron energies. The latter situation could only be realized if energy were given up to the gas in the drift chamber but the degree to which this phenomenon contributes cannot be estimated at the present time.

Results obtained using a titanium linear array calorimeter are presented in Figure B.4 where in part (a) measured energy deposition profiles are presented for various distances from the anode on the drift chamber axis (as for the graphite calorimeter array above, and for the tantalum array likewise, this calorimeter array samples only a small portion of the beam at all but those positions where the beam exhibits a pinch). These results indicate that there is not a strong dependence upon axial position, at least for that portion of the beam sampled by the calorimeter array. In part (b) of the figure, results are presented for the grounded and ungrounded conditions of the equilibrator and, as for the graphite, there appears to be no difference.

In Figure B.5 results obtained using a tantalum linear array calorimeter are presented at (a) 0.5 inch from the anode and (b) at the 6 inch position. It is felt that radiation heat transfer losses affected the measurements of the first two calorimeters of the linear array and as a result these energy deposition figures are low.

In Figure B.6 a typical spatial profile of the energy deposited in #25 Cinemoid by the electron-beam is presented. As can be seen from this figure, the beam possesses considerable spatial structure as it exits from the tube. This is not a spatial profile of the beam intensity or energy density but at the electron energies characteristic of Hermes I the electron stopping is nearly constant and therefore the results presented in this figure should give a reasonably good indication of the variation in beam intensity.
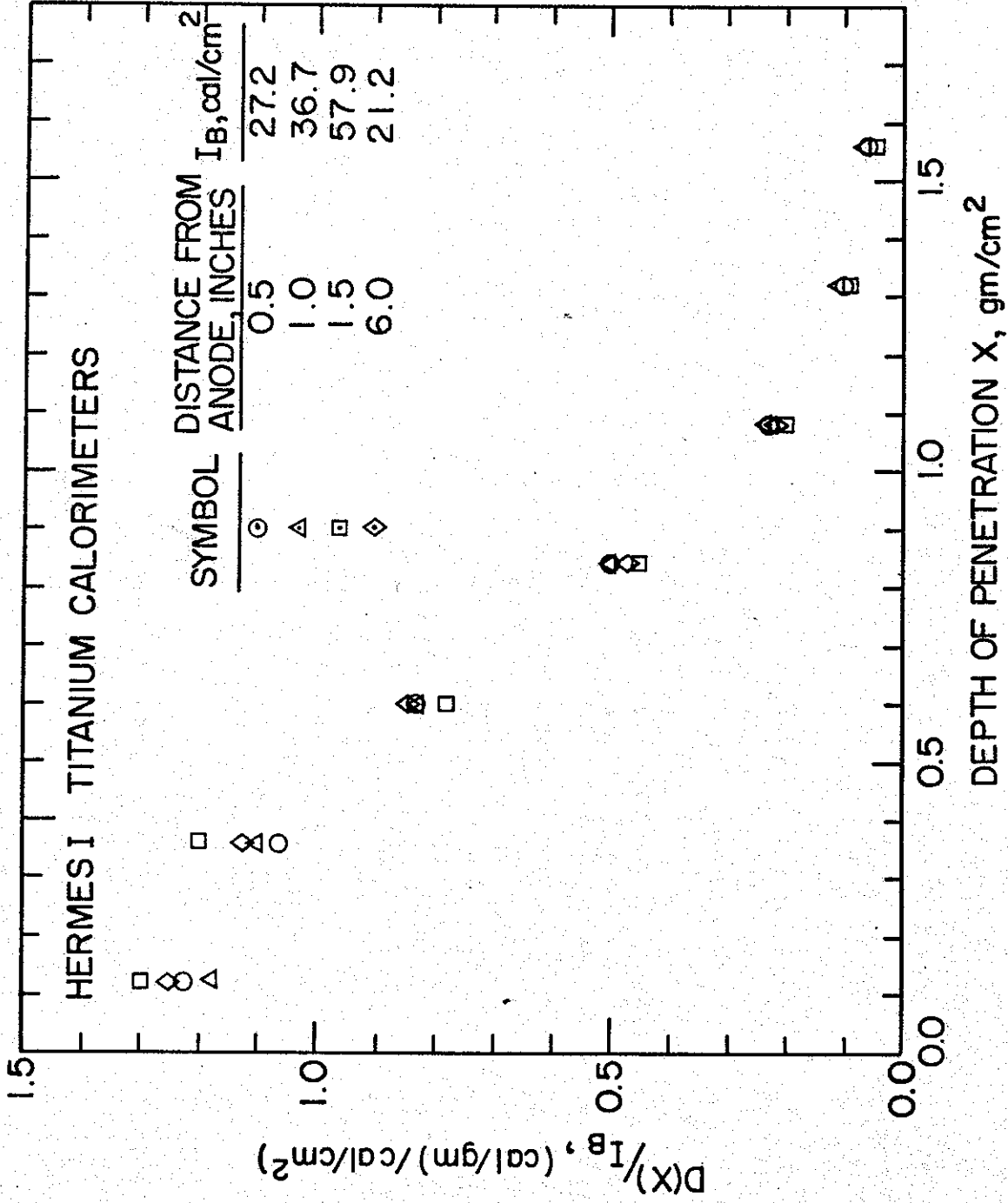
Figure B.4a. Energy deposition profiles in titanium on Hermes I at various positions on the drift chamber axis
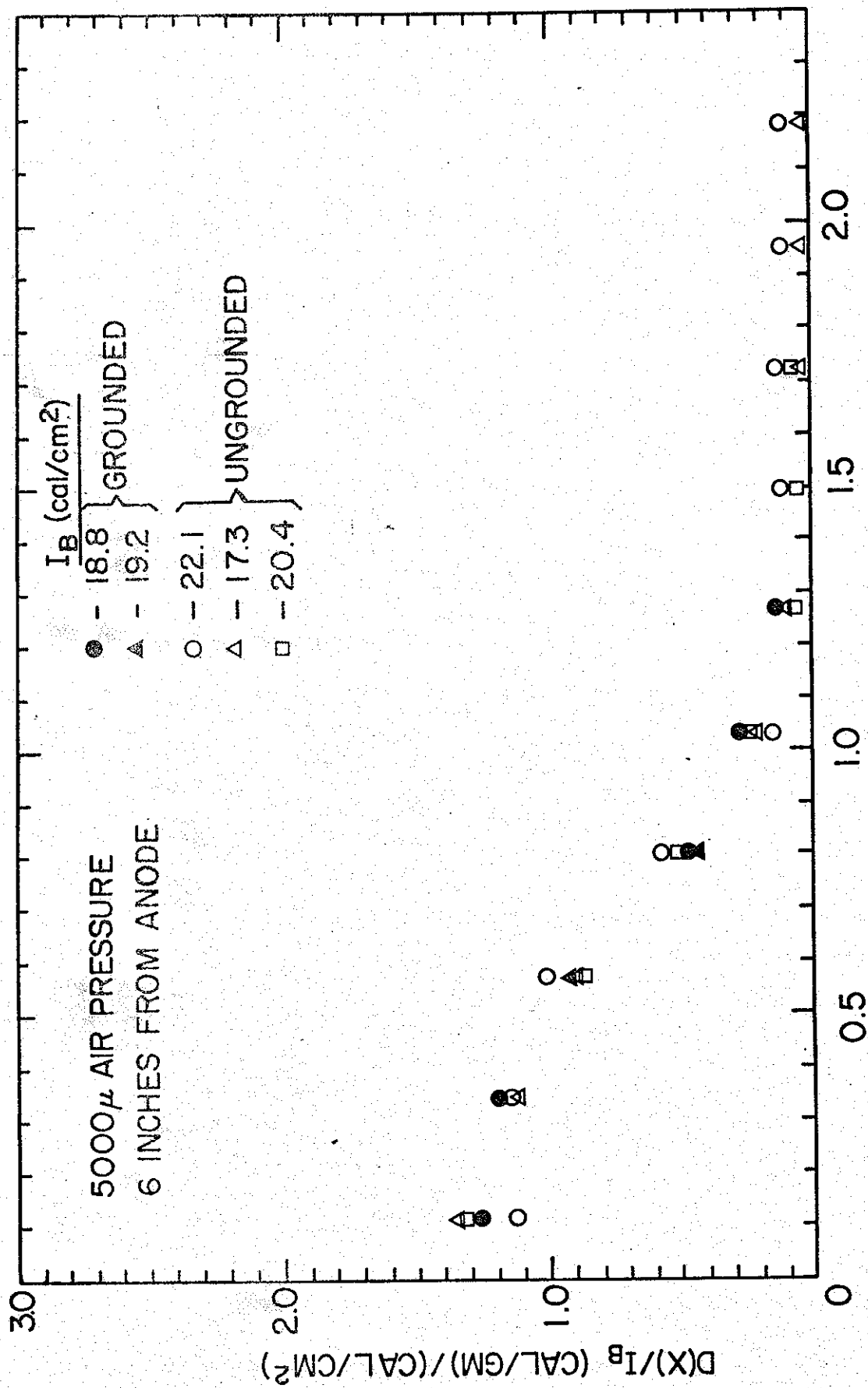
110

Figure B.4b. Energy deposition profiles in titanium on Hermes I at the 6 inch position in the grounded and ungrounded configurations
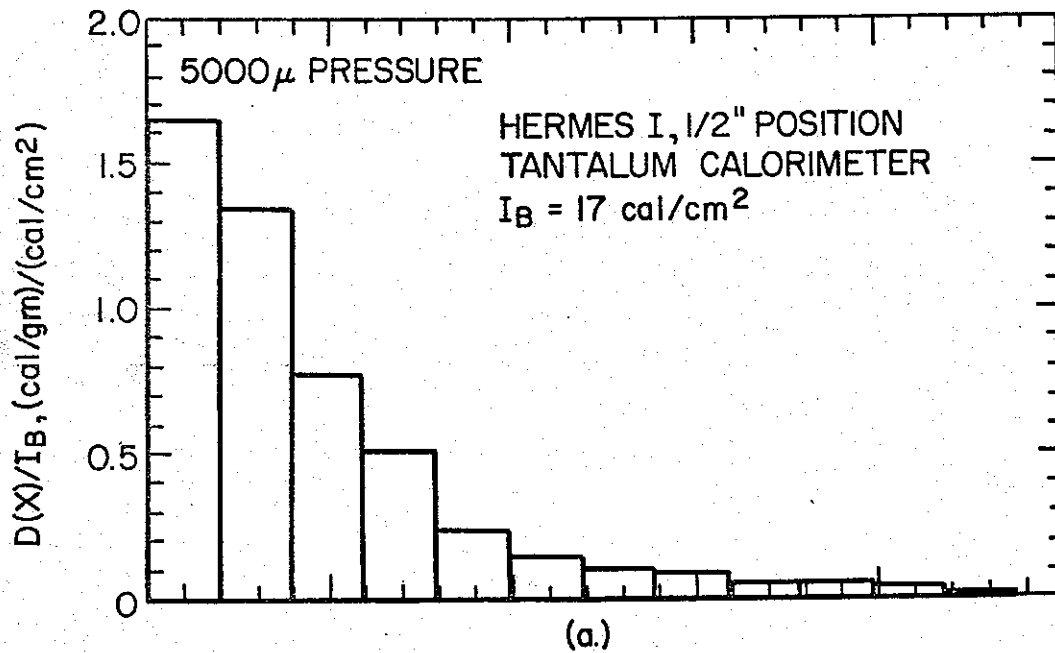
111

Figure B.5a.   Energy deposition profiles in tantalum on Hermes I
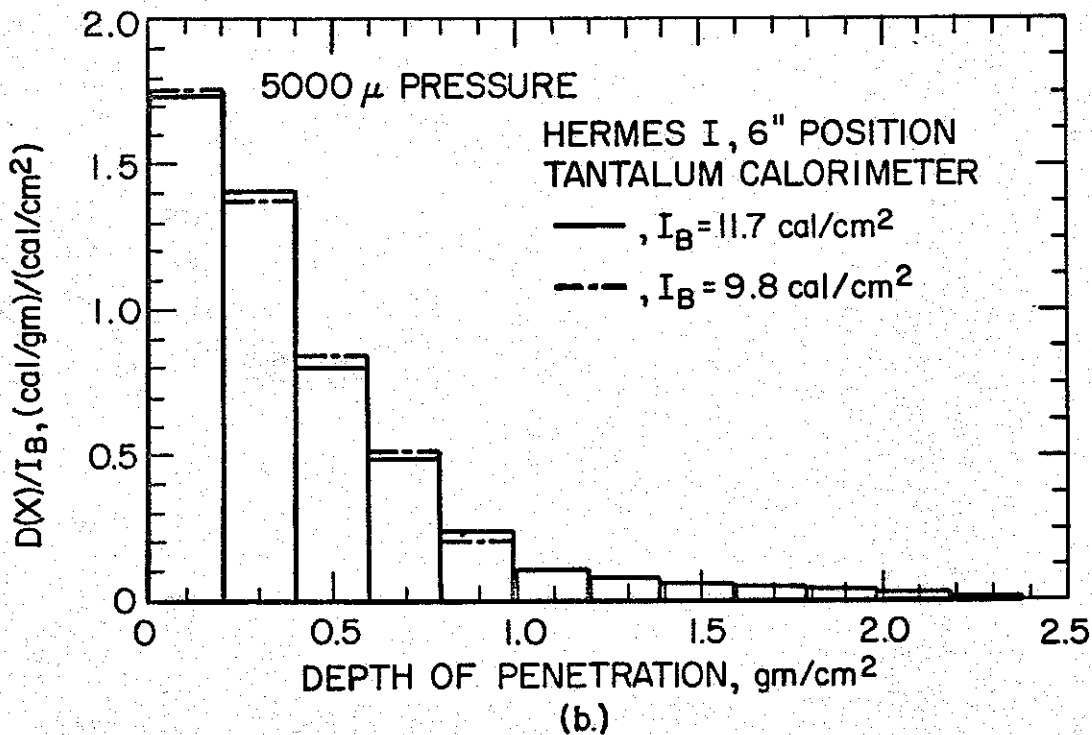at the 0.5 inch position

Figure B.5b.   Energy deposition profiles in tantalum on Hermes I
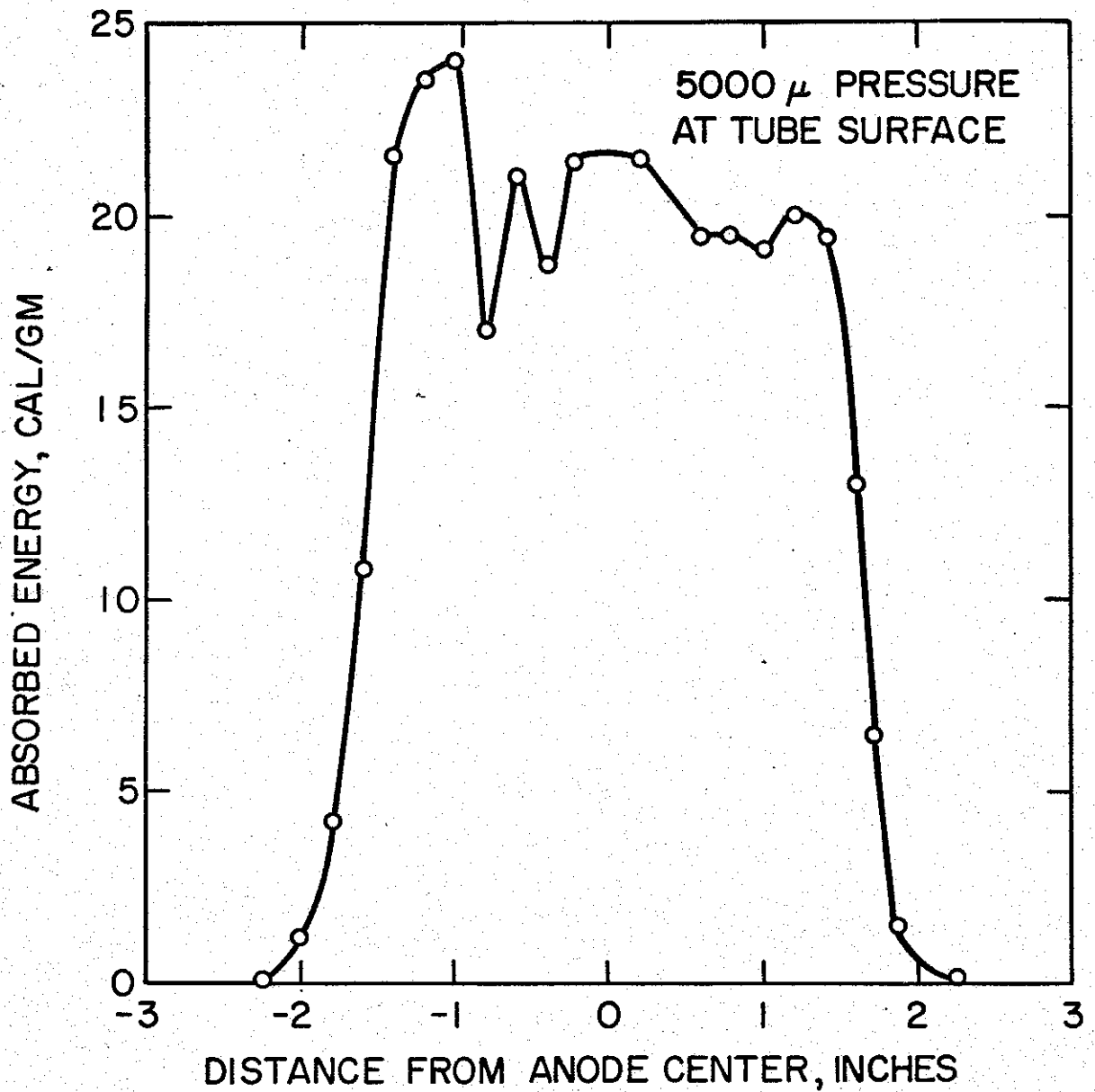at the 6 inch position

Figure B.6. Spatial profile of the dose to #25 Cinemoid perpendicular to the drift chamber axis at the tube surface on Hermes I

The beam energy density, on the drift chamber axis, is presented as a function of distance from the anode in Figure B.7. Inside the first pinch which occurs at about 3 inches from the anode, the reproducibility of the measurements is not as good as for the 5 and 6 inch positions, at least for that portion of the beam sampled by the calorimeters. The total beam energy output is expected to exhibit better reproducibility than the dose measurements based upon observed variations in the tube voltage and current time histories. This variation in measured beam intensity inside the first pinch is likely associated with variations in the beam-intensity spatial-profile from shot to shot. The peak in the beam intensity, commonly referred to as a pinch in the beam, corresponds to about 200 cal/cm^2.

The tube voltage and current time histories for Shot No. 823 on Hermes I are shown in Figure B.8 where the measurements were made using a resistive divider network and current viewing resistor ring for the voltage and current respectively. The current is known to 5 to 10 percent and voltage to 10 to 15 percent. Using these results and various values of tube shank inductance bracketing the estimated value of 0.67 μhenry, the electron number differential energy spectra presented in Figure B.9 were determined. For all values of the shank inductance employed the peak in the spectrum occurs at about 2.8 MeV. These spectra are characteristic of the entire electron beam (i.e., the total charge release per pulse) and would not necessarily be representative of only a small fraction of the beam which might be the situation of interest for an actual experiment.
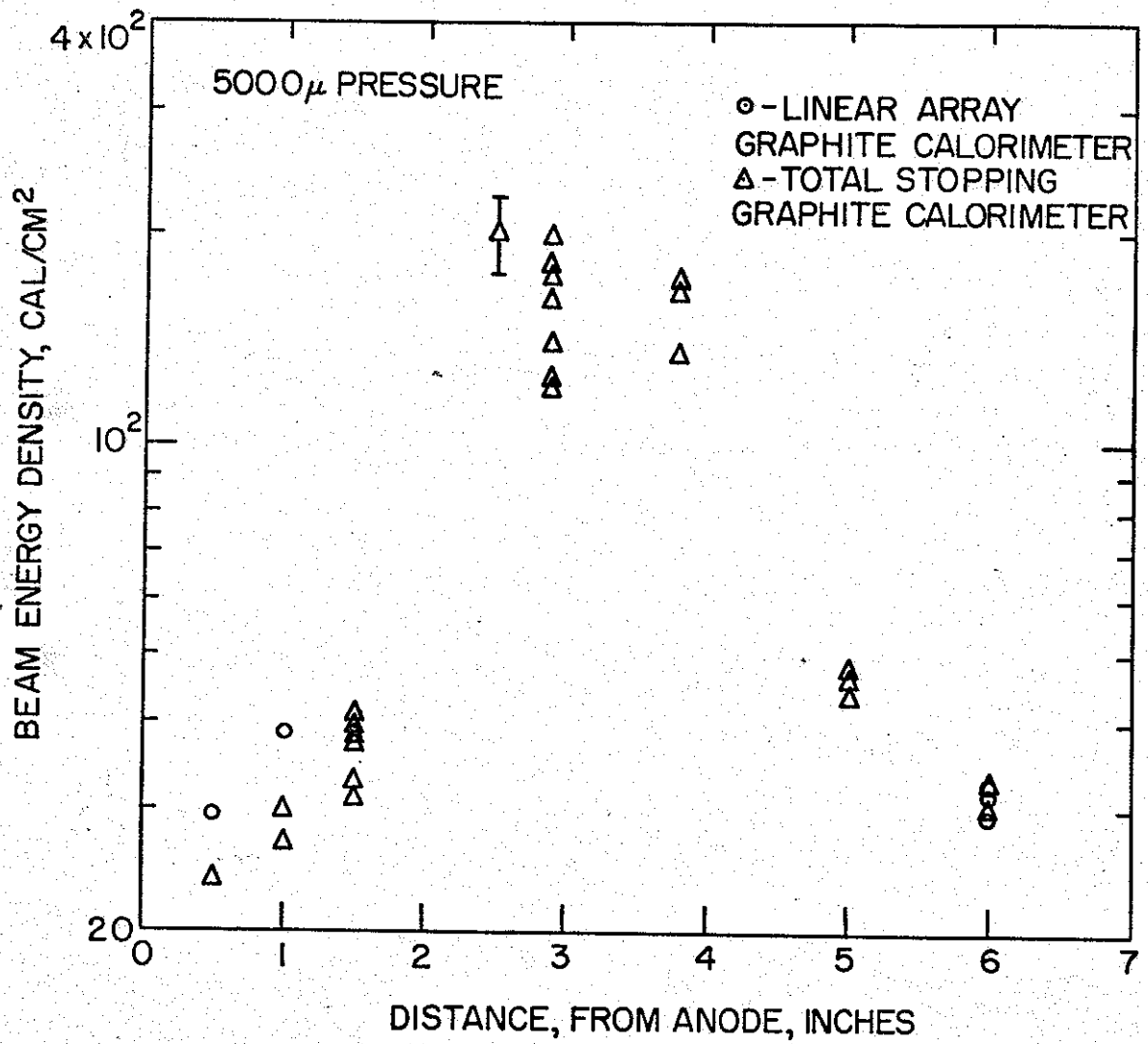
Figure B.7. Beam energy density on drift chamber axis vs. distance
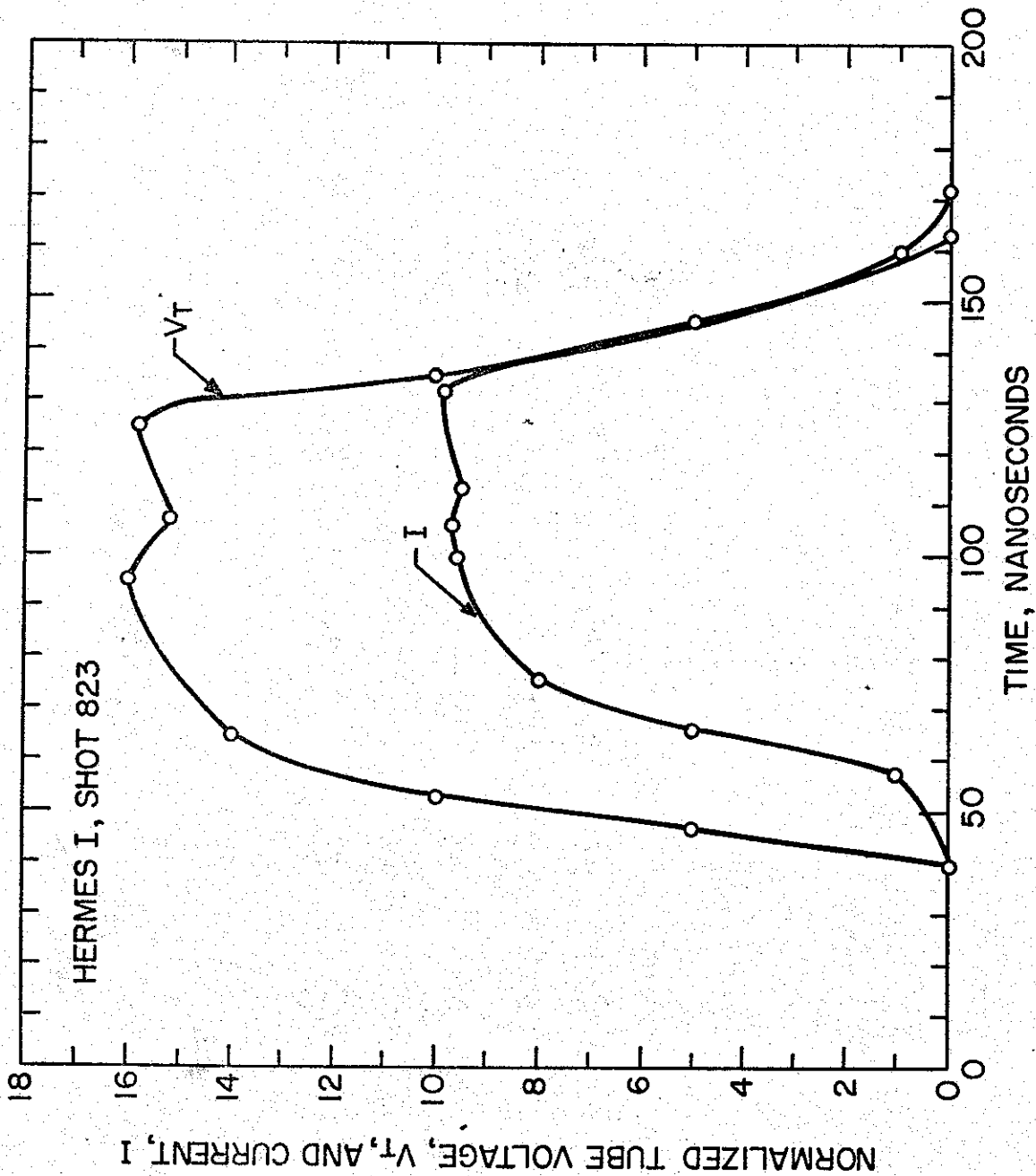from tube surface for Hermes I

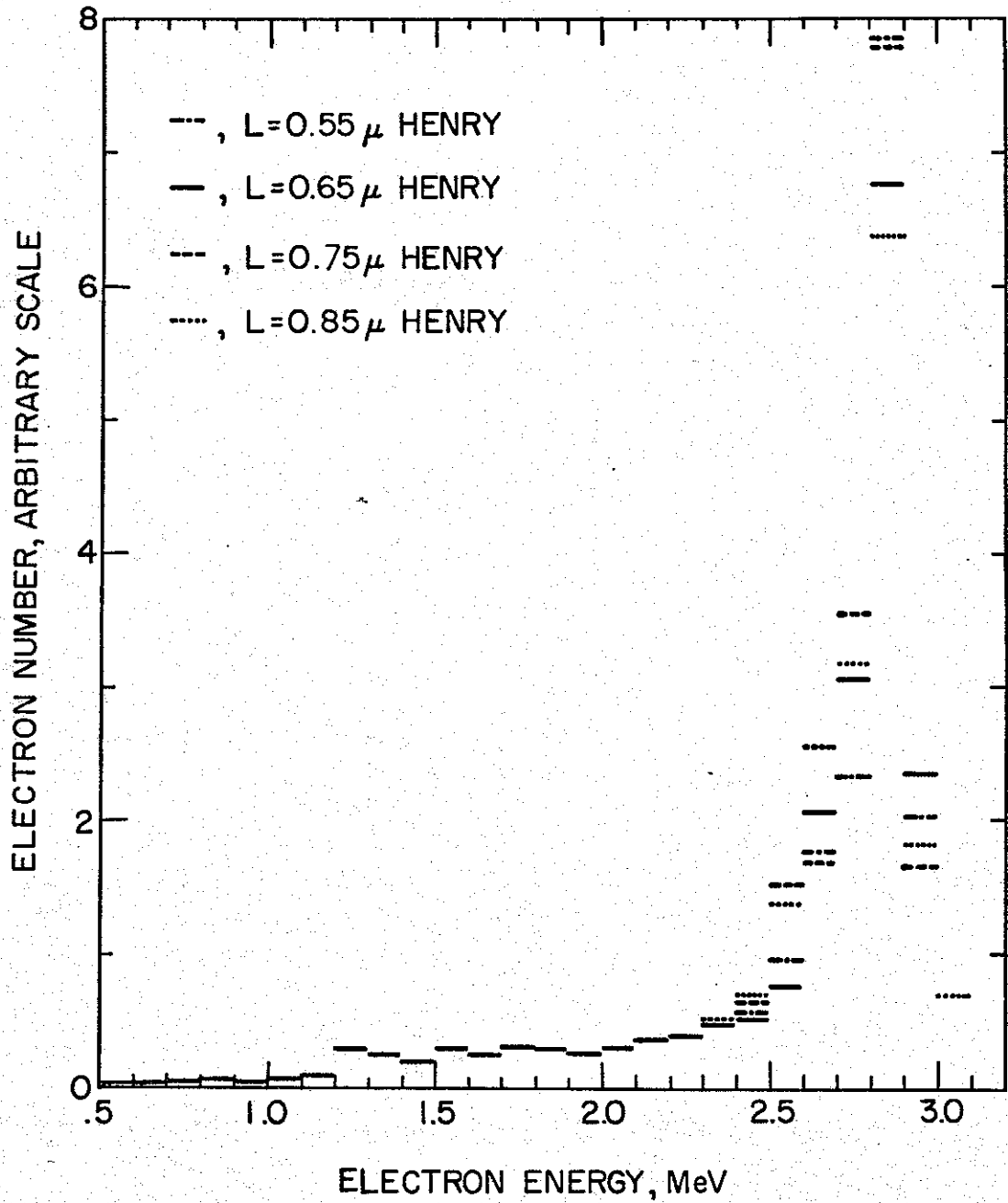Figure B.8. Typical voltage and current waveforms for Hermes I; Shot No. 823

Figure B.9. Electron differential energy spectra obtained from the voltage and current waveforms shown in Figure B.8 for various values of tube shank inductance

DISTRIBUTION:

Nuclear Engineering Department
University of New Mexico
Albuquerque, New Mexico 87106
   Attn: Prof. R. L. Long (1)
          Prof. G. A. Whan (1)

Electrical Engineering Department
University of New Mexico
Albuquerque, New Mexico 87106
   Attn: Prof. W. T. Grannemann (1)
          Prof. H. D. Southward (1)

EG&G, Inc.
P. O. Box 98
Goleta, California 93017
   Attn: Richard Mohr (1)
          Richard McGuire (1)

Lawrence Radiation Lab.
L-125
P. O. Box 808
Livermore, California 94550
   Attn: L. W. Woodruff
         J. L. Hesse
         J. L. Habberstad

A. J. Chabai, 1224
A. Goodman, 1224
J. T. Risse, 1548
W. H. Sullivan, 1548
R. G. Clem, 1730
C. G. Scott, 2316
K. L. Gillespie, 2320
E. G. Coffee, 2322
A. E. Giddings, 2322
J. P. Shoup, 2330
C. M. Tapp, 2610
G. W. Rodgers, 2620
J. A. Hood, 2650
W. T. Corbett, 2652
B. L. Gregory, 2653
F. N. Coppage, 2653
H. H. Sander, 2653
J. E. Schwiner, 2653
D. L. Weaver, 2653
D. H. Habing, 2654
B. D. Shafer, 2654
S. J. Buchsbaum, 5000
A. Narath, 5100
F. L. Vook, 5111
E. P. Eernisse, 5112
W. Herrmann, 5160
C. H. Karnes, 5165
L. C. Hebel, 5200
A. W. Snyder, 5220
R. M. Jefferson, 5221 (5)

F. A. Bailey, 5221
A. M. Chodorow, 5221
D. W. Dugan, 5221
J. E. Harness, 5221
R. L. Coats, 5222
J. V. Walker, 5223
P. E. Bolduc, 5223
W. H. Buckalew, 5223 (5)
J. A. Halbleib, 5223
J. G. Kelly, 5223
D. A. McArthur, 5223
L. D. Posey, 5223 (5)
J. E. Powell, 5223
R. L. Schuch, 5223
J. F. Schulze, 5223
G. C. Smith, 5224
G. A. Carlson, 5224
W. B. Gauster, 5225
F. C. Perry, 5225
C. R. Mehl, 5230
E. H. Beckner, 5240
T. H. Martin, 5245
J. E. Boers, 5245
D. L. Johnson, 5245
J. E. McDonald, 5300
L. M. Berry, 5500
R. G. Kepler, 5510
P. M. Beeson, 5514
L. A. Harrah, 5514
O. L. Burchett, 7362
G. E. Chaffee, 7531
E. L. Amador, 7532
D. E. Gregson, 8130
G. E. Brandvold, 8170
J. C. King, 8300
G. W. Anderson, 8330
J. L. Wirth, 8340
D. K. Dean, 8343
B. F. Murphey, 9100
C. D. Broyles, 9110
J. D. Plimpton, 9112
S. R. Dolce, 9112
H. N. Woodall, 9112
K. M. Glibert, 9112
J. G. Prather, 9112
J. L. Benson, 9115
M. M. Conrad, 9115
G. E. Hansche, 9120
R. S. Gillespie, 3411 (3)
G. C. McDonald, 3416
B. R. Allen, 3424
B. F. Hefley, 8232
C. H. Sproul, 3428-1 (15)

lw